



TECHNISCHE  
UNIVERSITÄT  
WIEN  
Vienna University of Technology

DISSERTATION

# **Effects of Fast Neutron Irradiation on Critical Currents and Intrinsic Properties of State-of-the-Art Nb<sub>3</sub>Sn Wires**

Ausgeführt zum Zwecke der Erlangung des akademischen Grades eines Doktors der  
technischen Wissenschaften unter der Leitung von

Univ.Prof. Dr.phil. Dr.h.c. Harald W. Weber  
E141  
Atominstitut

eingereicht an der Technischen Universität Wien  
Fakultät für Physik

von

Dipl.-Ing. Thomas Baumgartner  
Matrikelnummer: 0425162  
Düsseldorfsstraße 5–13/2/22  
1220 Wien, Österreich

Wien, am 27. Mai 2013



# Danksagung

Ich möchte mich an dieser Stelle herzlich bei Prof. Harald W. Weber für die Betreuungsarbeit im Rahmen meines Dissertationsprojekts sowie für seine besonnene Führung einer Arbeitsgruppe, die für mich zu einem wichtigen Teil meines Lebens geworden ist, bedanken. Im selben Atemzug sind meine Kollegen zu nennen, die für das gute Arbeitsklima verantwortlich zeichnen. Mein besonderer Dank gilt Michael Eisterer für unzählige interessante und hilfreiche Diskussionen, sowie für seine bewundernswerte Eigenschaft selbst in sehr schwierigen Situationen nicht seinen Humor zu verlieren.

Ohne unsere Partner am *CERN* wäre dieses Projekt nie zustande gekommen, weswegen ich ihnen – insbesondere Luca Bottura, René Flükiger und Christian Scheuerlein – zu Dank verpflichtet bin. Prof. Flükiger möchte ich außerdem dafür danken, dass er sich zur Teilnahme an meinem Rigorosum als Prüfer bereit erklärt hat.

Meinen Eltern, meinen Freunden und meiner Lebensgefährtin Doris habe ich mehr zu verdanken als ich an dieser Stelle aufzählen kann. Sie alle haben auf ihre eigene Weise zur Entstehung dieser Arbeit beigetragen.



# Kurzfassung

Die heutige Technologie supraleitender Magnete basiert hauptsächlich auf zwei Materialien: Nb-Ti und Nb<sub>3</sub>Sn. Während ersteres sich als wesentlich widerstandsfähiger in Bezug auf Strahlenschäden erweist, ist letzteres überlegen was seine supraleitenden Parameter betrifft. Der *Large Hadron Collider (LHC)* am *CERN* benutzt derzeit supraleitende Nb-Ti-Magnete für das Krümmen und Fokussieren der Teilchenstrahlen, welche in seinen ringförmigen Strahlrohren zirkulieren. Im Rahmen des *LHC Upgrade*-Projekts, welches auf eine Erhöhung der Luminosität des Colliders abzielt, wird die Möglichkeit untersucht, die so genannten inneren Triplets durch leistungsfähigere Nb<sub>3</sub>Sn-Magnete zu ersetzen. Die inneren Triplets sind Aufbauten aus Quadrupolmagneten, die zum Fokussieren der Strahlen in der Nähe der Wechselwirkungspunkte des *LHC* erforderlich sind, wo sie einem komplexen und intensiven Strahlungsfeld ausgesetzt sind. Aufgrund der Strahlenempfindlichkeit von Nb<sub>3</sub>Sn ist es essenziell zu untersuchen wie die supraleitenden Eigenschaften der in Frage kommenden Drähte von Strahlenschäden beeinflusst werden.

In der vorliegenden Arbeit werden die Effekte von schneller Neutronenstrahlung auf fünf moderne Nb<sub>3</sub>Sn-Drahttypen mit Hilfe von sequenzieller Bestrahlung von kurzen Drahtproben im *TRIGA Mark-II*-Reaktor am *Atominstitut* bis zu einer schnellen Neutronenfluenz von  $1.4 \cdot 10^{22} \text{ m}^{-2}$  untersucht. Zwei dieser Drähte wurden mit dem Restack-Rod-Prozess hergestellt und enthalten Tantal- bzw. Titan-Zusätze, zwei sind Powder-in-Tube-Drähte mit Tantal-Zusätzen, und einer ist ein unlegierter (binärer) Internal-Tin-Prototyp. SQUID-Magnetometrie wurde eingesetzt, um die kritische Stromdichte der Proben vor der Bestrahlung und nach jedem Bestrahlungsschritt im Temperaturbereich von 4.2 bis 15 K in angelegten Feldern von bis zu 7 T zu bestimmen. Um die Gültigkeit des Modells zu verifizieren, durch das sich die kritische Stromdichte aus Magnetometriedaten ermitteln lässt, wurden Transportstrommessungen an längeren Proben bei einer Temperatur von 4.2 K in angelegten Feldern von bis zu 15 T durchgeführt. Änderungen der kritischen Temperatur und des oberen kritischen Feldes wurden mit Hilfe von Wechselfeld-Suszeptibilitätsmessungen im

Nullfeld sowie Widerstandsmessungen in angelegten Feldern von bis zu 15 T ebenfalls untersucht.

Innerhalb des untersuchten Fluenzbereichs wurde eine geringe lineare Abnahme der kritischen Temperatur in allen Drahttypen gefunden, wie es angesichts des Einbringens von Unordnung zu erwarten war. Der gemessene Anstieg des oberen kritischen Feldes aufgrund der Abnahme der mittleren freien Weglänge der Elektronen durch strahleninduzierte Unordnung war unerwartet klein. Ein signifikanter Anstieg von ungefähr 50% wurde in der kritischen Stromdichte bei einer Temperatur von 4.2 K und einem Magnetfeld von 6 T in allen Drahttypen gefunden.

Das Pinning-Kraft-Skalierungsverhalten der Drahtproben wurde basierend auf den mittels SQUID-Magnetometrie erhaltenen Daten unter Verwendung einer zu diesem Zweck entwickelten Software analysiert. Es wurde festgestellt, dass im Fall der vier Drahttypen, die Zusätze enthalten, die Skalierbarkeit innerhalb des per Magnetometrie zugänglichen 7 T-Feldbereichs nur durch die Einführung einer physikalisch nicht sinnvollen Temperaturabhängigkeit des Skalierungsfeldes (es übersteigt das obere kritische Feld bei tiefen Temperaturen) erzwungen werden kann. Diese eingeschränkte Skalierbarkeit ist ein unerwartetes Ergebnis und verlangt nach weiterer Erforschung der Flussverankerung in solchen Drähten. Das wichtigste Resultat dieser Arbeit ist, dass die strahleninduzierten Änderungen des Pinning-Kraft-Skalierungsverhaltens mit einem Zwei-Komponenten-Modell beschrieben werden können, das einen Beitrag von einem zweiten Pinning-Mechanismus zu der Pinning-Funktion hinzufügt, die den unbestrahlten Zustand beschreibt. Dieser zweite Mechanismus wurde als Pinning durch Kernwechselwirkung zwischen den Flusslinien und normalleitenden punktartigen Strukturen identifiziert. Es wurde ermittelt, dass die Abhängigkeit des Punkt-Pinning-Beitrags von der schnellen Neutronenfluenz eine universelle Funktion für alle untersuchten Drahttypen ist.

# Abstract

The present day superconducting magnet technology is mostly based on two materials: Nb-Ti and Nb<sub>3</sub>Sn. While the former is by far more resilient when it comes to radiation damage, the latter is superior in terms of its superconducting parameters. The *Large Hadron Collider (LHC)* at *CERN* currently uses Nb-Ti superconducting magnets for bending and focusing the particle beams circulating in its ring-shaped beam pipes. In the course of the *LHC Upgrade* project, which aims at increasing the luminosity of the collider, the option of replacing the so-called inner triplets by more powerful Nb<sub>3</sub>Sn magnets is being investigated. The inner triplets are assemblies of quadrupole magnets required for focusing the beams near the interaction points of the *LHC*, where they are exposed to a complex and intense radiation field. Due to the radiation sensitivity of Nb<sub>3</sub>Sn it is essential to examine how the superconducting properties of the candidate wires are affected by radiation damage.

In the present work the effects of fast neutron irradiation on five state-of-the-art Nb<sub>3</sub>Sn wire types are examined by means of sequential irradiation of short wire samples in the *TRIGA Mark-II* reactor at the *Atominstut* up to a fast neutron fluence of  $1.4 \cdot 10^{22} \text{ m}^{-2}$ . Two of these wire types are restack rod processed strands containing tantalum and titanium additions, respectively, two are powder-in-tube wires with tantalum additions, and one is an unalloyed (binary) prototype internal tin strand. SQUID magnetometry was used to assess the critical current density of the samples before irradiation and after each irradiation step in the temperature range from 4.2 to 15 K in applied fields of up to 7 T. To verify the validity of the evaluation model used for obtaining the critical current density from magnetometry data, transport measurements were performed on longer samples at a temperature of 4.2 K in applied fields of up to 15 T. Changes in the critical temperature and in the upper critical field were also investigated by means of AC susceptibility measurements in zero applied field, and resistivity measurements in applied fields of up to 15 T, respectively.

Within the examined fluence range a small linear decrease of the critical temperature was

found in all wire types, as expected owing to the introduction of disorder. The increase in the upper critical field due to a decrease of the electronic mean free path caused by radiation induced disorder was found to be unexpectedly small. A significant increase of approximately 50% was found in the critical current density at a temperature of 4.2 K and a magnetic field of 6 T in all wire types.

The pinning force scaling behavior of the wire samples was analyzed based on the data obtained from SQUID magnetometry using a software code designed for that purpose. It was found that in the four wire types containing additives, a physically unsound temperature dependence of the scaling field (it exceeds the upper critical field at low temperatures) must be introduced to enforce scaling within the 7 T field range accessible by magnetometry. This limited scalability is an unexpected outcome, and calls for further research on flux pinning in such wires. The most important result of this work is that the irradiation induced changes in the pinning force scaling behavior can be described by a two-component model which adds a contribution of a second pinning mechanism to the pinning function describing the unirradiated state. This second mechanism was identified as pinning by core interaction between the vortices and normal conducting point-like structures. The dependence of the point-pinning contribution on fast neutron fluence was found to be a universal function for all examined wire types.



# Contents

<b>List of Symbols</b>	<b>11</b>
<b>1. Introduction</b>	<b>15</b>
1.1. The LHC Upgrade project . . . . .	15
1.2. Physical background . . . . .	17
1.2.1. Disordered A-15 compounds . . . . .	17
1.2.2. Flux pinning in polycrystalline Nb <sub>3</sub> Sn . . . . .	25
1.2.3. Irradiation effects . . . . .	28
<b>2. Sample Specifications and Preparation</b>	<b>41</b>
2.1. Specifications . . . . .	41
2.1.1. Wire types . . . . .	41
2.1.2. Heat treatments . . . . .	44
2.2. Preparation . . . . .	45
2.2.1. Samples for magnetization measurements . . . . .	45
2.2.2. Samples for transport measurements . . . . .	47
2.2.3. Samples for upper critical field measurements . . . . .	48
2.3. Irradiation procedure . . . . .	48
<b>3. Measurements</b>	<b>55</b>
3.1. SQUID magnetometry . . . . .	55
3.1.1. Standard sample transport . . . . .	57
3.1.2. Problems with the standard sample transport . . . . .	59
3.1.3. RSO . . . . .	68
3.1.4. AC susceptibility . . . . .	70
3.2. VSM measurements . . . . .	74
3.2.1. Comparison with SQUID magnetization data . . . . .	74
3.2.2. Angular dependence of the magnetic moment . . . . .	75
3.3. Measurements in the 17 T system . . . . .	77
3.3.1. Transport current measurements . . . . .	78
3.3.2. Upper critical field measurements . . . . .	85
3.4. Data evaluation . . . . .	87
3.4.1. Model for the evaluation of $J_c$ from magnetometry data . . . . .	87
3.4.2. Self-field correction . . . . .	90
3.4.3. Standard sample transport correction . . . . .	93
3.4.4. $I_c$ from transport measurements . . . . .	95

3.4.5.	$J_c$ from SQUID magnetometry . . . . .	96
3.4.6.	Comparison of magnetometry and transport results . . . . .	98
3.4.7.	$T_c$ from AC susceptibility . . . . .	102
3.4.8.	$B_{c2}(T)$ from resistivity measurements . . . . .	105
<b>4.</b>	<b>Results and Discussion</b>	<b>107</b>
4.1.	Properties in the unirradiated state . . . . .	107
4.1.1.	Critical current density . . . . .	107
4.1.2.	Critical temperature . . . . .	111
4.1.3.	Upper critical field . . . . .	113
4.1.4.	Scaling behavior . . . . .	117
4.2.	Radiation induced changes . . . . .	125
4.2.1.	Critical current density . . . . .	125
4.2.2.	Critical temperature . . . . .	129
4.2.3.	Upper critical field . . . . .	132
4.2.4.	Scaling behavior . . . . .	135
4.3.	Conclusions . . . . .	143
4.3.1.	Summary of the results . . . . .	143
4.3.2.	Outlook . . . . .	147
	<b>Bibliography</b>	<b>149</b>
	<b>Curriculum Vitae</b>	<b>161</b>

# List of Symbols

The symbols which are frequently used in this work are listed in the following. Unless stated otherwise, all quantities are measured in SI units.

## Constants:

$\hbar$	Reduced Planck constant.
$k_B$	Boltzmann constant.
$\mu_0$	Vacuum permeability.

## Variables:

$a$	Lattice parameter.
$A_{A-15}$	A-15 area of a sub-element.
$B$	Magnetic field inside a material (as opposed to the applied field).
$B_{AC}$	Amplitude of an alternating magnetic field.
$B_c$	Thermodynamic critical field.
$B_a$	Applied magnetic field.
$B_{c2}, B_{c2}^*$	Upper critical field, scaling field.
$B_p$	Pauli paramagnetic limiting field.
$B_{sf}$	Self-field caused by the current distribution inside a sample.
$b$	Reduced magnetic field relative to $B_{c2}$ or $B_{c2}^*$ .
$b_{max}$	Value of $b$ at which the volume pinning force exhibits its maximum.
$d$	Bean model penetration depth.
$E$	Electric field.
	Energy.
$f(b)$	Pinning force function.
$f_p, F_p$	Elementary pinning force per unit length, volume pinning force.
$h(t)$	Temperature scaling function.
$I, I_c$	Electric current, critical current.
$J, J_c$	Electric current density, critical current density.

$L$	Sample length.
$l$	Mean free path of electrons.
$m, m_{\text{irr}}$	Total magnetic moment, irreversible magnetic moment.
$m', m''$	In-phase and out-of-phase components of the magnetic moment in AC susceptibility measurements.
$M_a$	Atomic mass of a specific isotope.
$N$	Number of sub-elements in a sample. Number of particles. Density of states.
$n$	Power law exponent in transport critical current measurements. Fit parameter in the two-mechanism pinning model.
$p$	Low-field exponent in the pinning force function.
$q$	High-field exponent in the pinning force function.
$S$	Long range order (Bragg-Williams) parameter.
$T$	Temperature.
$T_c, T_c^*$	Critical temperature, effective critical temperature for scaling.
$t$	Reduced temperature relative to $T_c$ or $T_c^*$ . Time (in particular irradiation time).
$t_{1/2}$	Half life of a specific radioactive isotope.
$V$	Voltage.
$x$	Additive content in ternary A-15 compounds.
$\alpha$	Contribution of the original (unirradiated) pinning mechanism in the two-mechanism pinning model. Paramagnetic limitation (Maki) parameter.
$\beta$	Contribution of the radiation induced pinning mechanism in the two-mechanism pinning model. Misalignment angle in magnetization measurements.
$\gamma$	Electronic specific heat coefficient.
$\Delta T_c$	Transition width of the critical temperature.
$\kappa$	Ginzburg-Landau parameter.
$\lambda_{\text{ep}}$	Electron-phonon interaction parameter.
$\lambda_{\text{so}}$	Spin-orbit scattering parameter.
$\bar{\tau}$	Mean electron lifetime.
$\xi_0$	BCS coherence length.
$\rho_i, \rho_o$	Inner and outer sub-element radii.

$\rho_n$	Normal state resistivity slightly above $T_c$ .
$\sigma_{\text{eff}}$	Effective cross section of a nuclear reaction for a specific neutron spectrum.
$\sigma_{\text{trans}}$	Nuclear transmutation cross section.
$\Phi, \Phi_f$	Generic particle flux density or total neutron flux density, fast neutron flux density.
$\chi$	Magnetic AC susceptibility.



# 1. Introduction

The purpose of this chapter is to elucidate the inducements for the experimental undertakings and theoretical considerations presented in this work. The main goal was to investigate the effects of fast neutron irradiation on state-of-the-art multifilamentary Nb<sub>3</sub>Sn wires by means of magnetization and transport measurements, as specified in a collaboration agreement between *CERN* and the *Atominstitut*. These wires are potential candidates for an upgrade of the *Large Hadron Collider*, which is briefly outlined in Section 1.1. The underlying physics of disordered Nb<sub>3</sub>Sn and A-15 superconductors in general as well as the results of previous irradiation studies are discussed in Section 1.2.

## 1.1. The LHC Upgrade project

The *Large Hadron Collider (LHC)* is the most powerful instrument ever built for the purpose of exploring the realm of particle physics. Its well over a thousand superconducting Nb-Ti dipole magnets provide the means for keeping protons with energies of up to 7 TeV on a circular trajectory, following the beam pipes built into a ring-shaped tunnel with a circumference of roughly 27 km. Two such proton beams travel in opposite directions, thus providing center of mass energies of up to 14 TeV when they are brought to collision at the four interaction points where the major detectors *ATLAS*, *CMS*, *ALICE*, and *LHCb* are located. At these points the beams have to be focused very tightly (about 10  $\mu\text{m}$  beam diameter) in order to maximize the collision rate, which is accomplished by groups of quadrupole magnets, known as “inner triplets”.

Each inner triplet consists of four quadrupole magnets, the inner two of which are regarded as one unit (designated as “Q2”), which is why the structure is referred to as a triplet. The currently installed quadrupole magnets are based on Nb-Ti technology, and provide a field gradient of 205 T/m at an operating temperature of 1.9 K. The aperture of these

magnets is 70 mm, and they allow a  $\beta^*$  of 0.55 m, which corresponds to a luminosity of  $10^{38} \text{ m}^{-2} \text{ s}^{-1}$ .<sup>1</sup> It is the goal of the *LHC Upgrade* project to increase the luminosity of the collider by a factor of five, yielding  $5 \cdot 10^{38} \text{ m}^{-2} \text{ s}^{-1}$ . This project involves replacing the currently installed inner triplets by more powerful units, which can provide a comparable field gradient while having a considerably larger aperture, thus allowing a lower  $\beta^*$ . One way of realizing such upgraded inner triplets is to build magnets based on Nb<sub>3</sub>Sn instead of Nb-Ti [144].

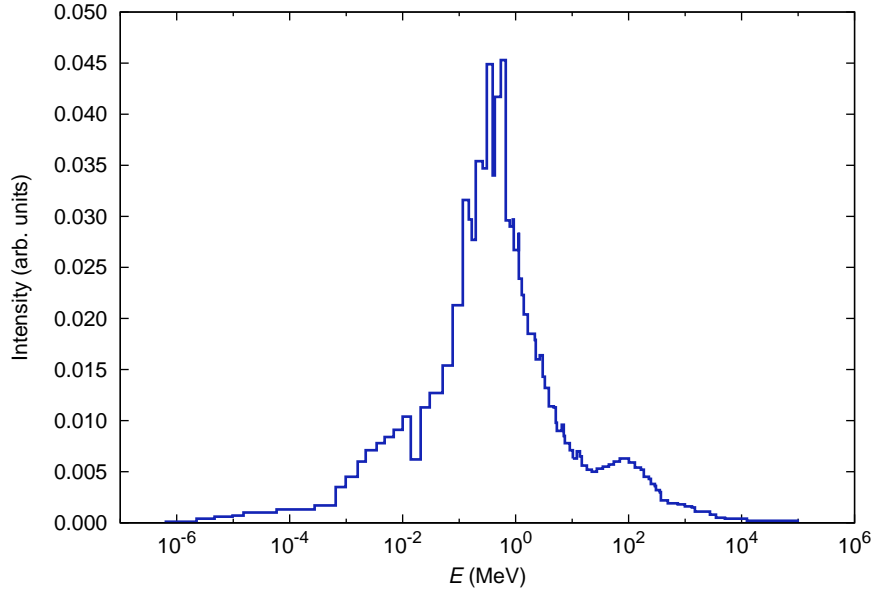
Due to their proximity to the interaction points of the *LHC* the inner triplets are exposed to a complex and intense radiation field. After interaction with the shielding material, the radiation reaching the superconductor is comprised mostly of photons, electrons, positrons, neutrons, protons, and pions, with particle energies extending well into the 100 GeV range. Aside from heating, the photons are expected to have no significant effect on the superconductors, whereas the other particles can transfer sufficient energy to the atoms in the magnet wires to create defects. The peak power density deposited in the magnets by the radiation will be of the order of  $10^7 \text{ W/m}^3$  after the luminosity upgrade [143]. It is a well known fact that Nb<sub>3</sub>Sn is a lot more sensitive to radiation damage than Nb-Ti [136], which raises the question whether this material is feasible for the construction of magnets capable of operating in such a radiation environment. It is the purpose of the present work to investigate the effects of neutron irradiation damage on several state-of-the-art Nb<sub>3</sub>Sn multifilamentary wires which are potential candidates for the production of upgraded inner triplet magnets.

Figure 1.1 shows the neutron spectrum the inner triplet magnets will be exposed to according to calculations by Cerutti [24]. As can be expected, this spectrum is very different from that of a fission reactor (cf. Section 2.3). However, its maximum is located at around 1 MeV, which is comparable to the peak energy of fast reactor neutrons. Therefore, it stands to reason that irradiation studies carried out using the *TRIGA Mark-II* reactor at the *Atominstitut* in Vienna will be representative for neutron damage occurring in the *LHC* radiation environment. To account for the contributions of neutrons with very high energies (notice the peak in the spectrum at around 100 MeV), damage energy scaling appears to be a promising option [136]. The effects of other types of radiation, especially those of proton radiation (from which data on pions may be inferred), are studied separately.

---

<sup>1</sup>The parameter  $\beta^*$  is a measure of the distance from the interaction point at which the beam is twice the size of that at the interaction point.





**Figure 1.1.:** Calculated neutron spectrum at the inner winding of quadrupole Q2 [24].

## 1.2. Physical background

When  $\text{Nb}_3\text{Sn}$  was discovered to be superconducting in 1954 by Matthias [81], its critical temperature of 18 K was the highest known at the time. Since then a vast amount of research has been dedicated to the production and improvement of wires made of this material, and today  $\text{Nb}_3\text{Sn}$  is the second most important commercial superconductor after Nb-Ti.  $\text{Nb}_3\text{Sn}$  crystallizes with the  $\beta$ -tungsten structure, forming a brittle intermetallic compound. It belongs to a class of materials known as A-15 compounds, which all have the composition  $A_3B$  in common. In order to investigate the effects of neutron irradiation on the samples examined in this work, knowledge of the physics describing disordered A-15 systems and radiation damage is essential. It is the purpose of the following subsections to review the physical principles most relevant to this field of knowledge.

### 1.2.1. Disordered A-15 compounds

The A-15 structure is depicted in Figure 1.2: The  $B$  type atoms form a body-centered cubic sublattice which is intersected by chains of  $A$  type atoms. Two such chains run parallel on opposite faces of the cube, and the three pairs of chains are orthogonal to each other. Out of the many possible  $A_3B$  compounds 60 exhibit superconductivity, and some undergo a

martensitic transformation to a tetragonal phase at a temperature  $T_M > T_c$ . For pure  $\text{Nb}_3\text{Sn}$  the transformation temperature is 43 K. [99]

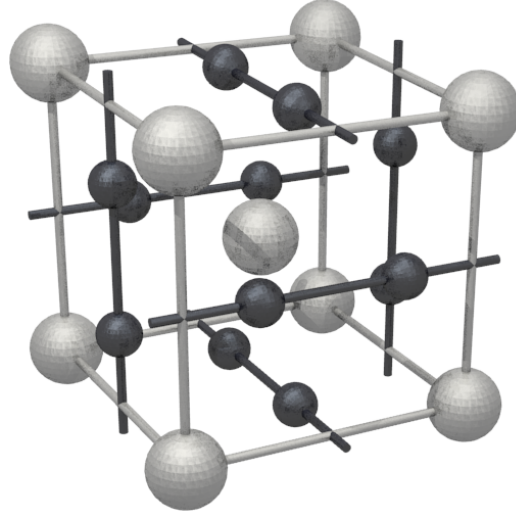


**Figure 1.2.:** Crystal structure of A-15 compounds. In  $\text{Nb}_3\text{Sn}$  the large bright balls are Sn atoms, and the small dark ones are Nb atoms.

Research on the superconducting A-15 compounds revealed that the critical temperature  $T_c$ , the normal state resistivity  $\rho_n$  (measured at a temperature slightly above  $T_c$ ), and the upper critical field  $B_{c2}$  of these materials strongly depend on the degree of disorder in their atomic structure. In [48] and [46] the effects of introducing disorder in the A-15 superconductors  $\text{Nb}_3\text{Sn}$ ,  $\text{Nb}_3\text{Al}$ ,  $\text{Nb}_3\text{Ge}$ ,  $\text{Nb}_3\text{Ir}$ ,  $\text{Nb}_3\text{Pt}$ ,  $\text{Nb}_3\text{Au}_{0.7}\text{Pt}_{0.3}$ ,  $\text{V}_3\text{Si}$ ,  $\text{V}_3\text{Ga}$ , and  $\text{Mo}_3\text{Os}$  are discussed. In these studies the atomic order was affected by changing the chemical composition, as well as by thermal quenching and annealing. A general trend observed in a multitude of materials is that  $\rho_n$  takes on its minimum value in the case of perfect ordering, and rises with increasing disorder. In A-15 systems  $T_c$  usually decreases with increasing disorder ( $\text{Nb}_3\text{Ir}$  is an exception), while  $B_{c2}$  usually increases ( $\text{Mo}_3\text{Os}$  is an exception).

A convenient quantity for describing the disorder in a crystallographic system is the long range order parameter  $S$ , also known as Bragg-Williams parameter. For a binary compound it is defined by

$$S = \frac{|f_A^A - c_A|}{1 - c_A}, \quad (1.1)$$

where  $f_A^A$  is the fraction of  $A$  type atoms occupying  $A$  sites, calculated with respect to the number of  $A$  type atoms in the crystal, and  $c_A$  is the fraction of  $A$  type atoms relative to the total number of atoms in the crystal [93]. In A-15 compounds  $c_A$  takes on the value  $3/4$ , and (1.1) can thus be simplified to

$$S = 4f_A^A - 3. \quad (1.2)$$

Since  $S$  does not depend on how the disorder was introduced, it defines a common scale for comparing systems disordered by chemical processes, thermal treatments, and radiation damage. Therefore, the above-mentioned findings are also relevant to the radiation sensitivity of A-15 materials, which is discussed in Subsection 1.2.3.

### Effects of disorder on $B_{c2}$

The dependence of  $\rho_n$  on atomic order can be explained by the fact that an increase in disorder results in a reduction of the mean free path  $l$  of the conduction electrons. Consequently, due to stronger scattering the average electron drift velocity in a given electric field decreases, which macroscopically manifests itself in a resistivity increase. The observed increase of  $B_{c2}$  can also be explained by the decrease of  $l$ , as shown by Gor'kov [55] and discussed within the framework of the GLAG theory in standard literature such as [138] and [11]. In the dirty limit, which is characterized by an electronic mean free path much smaller than the BCS coherence length  $\xi_0$ , the Ginzburg-Landau parameter  $\kappa$  can be expressed as a function of  $\rho_n$ :

$$\kappa = \kappa_0 + C\sqrt{\gamma}\rho_n \quad \text{for } l \ll \xi_0 \quad \text{with } C = 2.37 \cdot 10^6 \frac{\text{kg}^{3/2} \cdot \text{m}^{5/2}}{\text{K} \cdot \text{A}^2 \cdot \text{s}^4} \quad (1.3)$$

In (1.3), which is known as the Gor'kov-Goodman relation,  $\kappa_0$  is the Ginzburg-Landau parameter of the pure material, and  $\gamma$  is the electronic specific heat coefficient. Due to the relationship

$$B_{c2} = \kappa \sqrt{2} B_c \quad (1.4)$$

the upper critical field exhibits an increase which primarily reflects the change in  $\kappa$  given by (1.3), since the thermodynamic critical field  $B_c$  can be expected to change only slightly owing to the small reduction in  $T_c$  observed at not too high degrees of disorder, which is discussed below.

The temperature dependence of  $B_{c2}$  in the dirty limit was derived by Maki [79, 80], and is also discussed in [138] and [11]. An analytical expression for  $B_{c2}(T)$  for arbitrary degrees of impurity was found by Helfand and Werthamer [61, 62], and was extended by them and Hohenberg to include the effects of Pauli spin paramagnetism and spin-orbit impurity scattering [140]. They were able to compute a function  $h^*(t)$  which relates the upper critical field at the reduced temperature  $t = T/T_c$  to the slope of  $B_{c2}(T)$  at  $T = T_c$ :

$$h^*(t) = \frac{B_{c2}(t)}{\left(-\frac{dB_{c2}}{dT}\right)_{t=1}} \quad (1.5)$$

Using the (numerically computed) value of this function at  $t = 0$  to extrapolate  $B_{c2}(T)$  data to the zero-field value of the upper critical field is commonly referred to as the WHH method after the names of the authors. The function  $h^*(t)$  depends on the paramagnetic limitation parameter  $\alpha$ , also known as Maki parameter, as well as the spin-orbit scattering parameter  $\lambda_{so}$ . The Maki parameter indicates how strongly the upper critical field is depressed by the difference in spin susceptibility between superconducting and normal state, which is referred to either as Pauli paramagnetic limiting or Clogston-Chandrasekhar limiting [25, 27]. As shown by Maki [80], the upper critical field in the presence of Pauli limiting is given by

$$B_{c2} = \frac{B_{c2}(\alpha = 0) B_p}{\sqrt{2B_{c2}^2(\alpha = 0) + B_p^2}}, \quad (1.6)$$

where  $B_p$  is the Pauli limiting field, which according to Clogston can be estimated using  $B_p = T_c \cdot 1.84 \text{ T/K}$  [27]. The connection between  $B_p$  and  $\alpha$  is given by

$$\alpha = \frac{\sqrt{2}B_{c2}(T = 0, \alpha = 0)}{B_p(T = 0)}. \quad (1.7)$$

According to Werthamer, Helfand, and Hohenberg the value of the Maki parameter takes the form

$$\alpha = \frac{3e^2\hbar\gamma\rho_n}{2m_e\pi^2k_B^2} \quad (1.8)$$

in the dirty limit [140]. The only material specific quantities in (1.8) are the resistivity  $\rho_n$ , and the specific heat coefficient  $\gamma$ . The elementary charge  $e$ , the reduced Planck constant

$\hbar$ , the electron mass  $m_e$ , and the Boltzmann constant  $k_B$  can be combined, yielding

$$\alpha = C \gamma \rho_n \quad \text{with} \quad C = 2.369 \cdot 10^3 \frac{\text{A}^2 \cdot \text{s}^5 \cdot \text{K}^2}{\text{kg}^2 \cdot \text{m}^2}. \quad (1.9)$$

They rearranged (1.7) into the form

$$\alpha = C \left( -\frac{dB_{c2}}{dT} \right)_{T=T_c} \quad \text{with} \quad C = 0.528 \text{ K/T}, \quad (1.10)$$

which is convenient for determining  $\alpha$  from  $B_{c2}(T)$  measurements. Without Pauli paramagnetic limiting ( $\alpha = 0$ ) the dirty limit value of  $h^*(0)$  is 0.693, leading to the expression

$$B_{c2}(0) = 0.693 T_c \left( -\frac{dB_{c2}}{dT} \right)_{T=T_c}, \quad (1.11)$$

which is frequently used to estimate the zero temperature upper critical field of dirty superconductors.

The influence of spin-orbit scattering was investigated by Hake, who computed  $h^*(0)$  as a function of  $\alpha$  for different values of the spin-orbit scattering parameter  $\lambda_{so}$  [60]. At high  $\lambda_{so}$  values the dependence of  $h^*(0)$  on  $\alpha$  becomes increasingly less pronounced owing to the fact that spin-orbit scattering increases the Pauli spin susceptibility in the superconducting state. In [92] Orlando et al. examined the purity dependence of  $B_{c2}$  in  $\text{Nb}_3\text{Sn}$  and  $\text{V}_3\text{Si}$ , and reported that neither clean (low resistivity) nor dirty (high resistivity)  $\text{Nb}_3\text{Sn}$  exhibited noticeable Pauli paramagnetic limiting, whereas  $\text{V}_3\text{Si}$  is strongly limited. They concluded that the value of  $\lambda_{so}$  necessary to explain this behavior is unreasonably high, and proposed a modification of the Pauli paramagnetic limiting field  $B_p$  based on the inclusion of the electron-phonon interaction in the following form:

$$B_p = C (1 + \lambda_{ep}) T_c \quad \text{with} \quad C = 1.86 \text{ T/K} \quad (1.12)$$

The large electron-phonon interaction parameter  $\lambda_{ep} \approx 1.8$  of  $\text{Nb}_3\text{Sn}$  [92] yields  $B_p \approx 94 \text{ T}$ . From (1.6) it is obvious that such a high limiting field has little influence on an upper critical field of roughly 25 T, which explains the apparent absence of Pauli paramagnetic limiting in this material.

In [103] Schachinger and Prohammer presented a full strong coupling analysis of the same data, taking into account the anisotropy of the electron-phonon interaction and of the Fermi

velocity. They concluded that in this case the Pauli paramagnetic limiting must be included to achieve good agreement between theory and experimental results. A small anisotropy of the upper critical field of Nb<sub>3</sub>Sn was reported by Foner and McNiff in [51]. They found an anisotropy  $\delta \approx 0.05$ , where  $\delta$  is defined as

$$\delta = \frac{B_{c2}[100] - B_{c2}[110]}{\langle B_{c2} \rangle} \quad \text{with} \quad \langle B_{c2} \rangle = \frac{B_{c2}[100] + B_{c2}[110]}{2}, \quad (1.13)$$

where the index tuple  $[hkl]$  denotes the crystallographic direction. The reported value of  $\delta$  was independent of whether or not the crystal undergoes a martensitic transformation. According to Foner and McNiff there is excellent agreement between experimental data and theory, assuming a dirty superconductor without Pauli paramagnetic limiting. Another result presented in [51] is that in the cubic phase of Nb<sub>3</sub>Sn  $B_{c2}$  is significantly higher at all temperatures (by approximately 4 T at  $T = 0$ ) than in the tetragonal phase. A detailed analysis of anisotropy effects, which takes into account the band structure of Nb<sub>3</sub>Sn, can be found in [14].

Multifilamentary Nb<sub>3</sub>Sn wires always exhibit a certain Sn concentration gradient within their filaments or sub-elements, leading to an off-stoichiometric A-15 phase [50, 132]. Hence, they can always be regarded as dirty superconductors, as opposed to single crystals where the dirty limit condition  $l \ll \xi_0$  may not apply. Another consequence of the Sn gradient is that the individual grains in multifilamentary wires differ from each other in composition, which results in a broadening of the transition when measuring  $T_c$  or  $B_{c2}(T)$  due to the strong dependence of these parameters on the Sn content [50].

For high-field magnet applications it is clearly beneficial to have superconducting wires with high upper critical field values. Due to the above described dependence of  $B_{c2}$  on atomic ordering, the upper critical field can be optimized by artificially increasing the normal state resistivity, as already suggested almost five decades ago by Hake [60]. This increase of  $\rho_n$  can be achieved relatively easily by adding certain elements to the precursors of Nb<sub>3</sub>Sn wires, thus producing ternary (for low additive concentrations sometimes referred to as pseudo-binary) A-15 phases. The effects of additives are described in many publications such as [32, 50, 52, 107, 123] (Ta additions), and [5, 32, 50, 52, 65, 110, 123] (Ti additions). Using Al as an additive was investigated in [91], adding Ni and Zn was examined in [32], and in [123] the results of works on the effects of adding V, Zr, Mo, Hf, and Ga are reviewed. In modern Nb<sub>3</sub>Sn wires the most common additives are Ta and Ti. As pointed out in [50], Ta substitutes Nb, thus forming  $(\text{Nb}_{1-x}\text{Ta}_x)_3\text{Sn}$ , whereas Ti sub-

stitutes Sn, yielding  $\text{Nb}_3(\text{Sn}_{1-x}\text{Ti}_x)$ . As a side effect of the addition of foreign elements to  $\text{Nb}_3\text{Sn}$ , the martensitic transformation to the tetragonal phase is suppressed [50, 100], which allows taking advantage of the higher critical field values of the cubic phase.

### Effects of disorder on $T_c$

Aside from increasing the upper critical field, additives in  $\text{Nb}_3\text{Sn}$  also have an effect on the critical temperature, as evidenced by the results presented in [123], [5], and [110]. Orlando et al. found that  $T_c$  appears to be a universal function of resistivity, which means that it does not matter which mechanism is responsible for the change in resistivity relative to clean, stoichiometric  $\text{Nb}_3\text{Sn}$  [91]. The critical temperature remains relatively unchanged up to  $\rho_n \approx 30 \mu\Omega \cdot \text{cm}$ , whereas it exhibits a significant decrease at higher resistivities.<sup>2</sup> As pointed out in a review article by Flükiger [50], the opposite variation of  $T_c$  and  $\rho_n$  in alloyed  $\text{Nb}_3\text{Sn}$  leads to the existence of an optimum value for the additive content  $x$ . For Ta additions this value is between 3 and 4 at.%, for Ti between 1 and 2 at.%.

Testardi and Mattheiss found an explanation for the universal dependence of the critical temperature on resistivity [128]. They introduced a broadening function to investigate how the properties of A-15 materials are affected by electron lifetime effects:<sup>3</sup>

$$X(E, \Gamma) = \int S(E, E', \Gamma) X(E', \Gamma = 0) dE' \quad (1.14)$$

In (1.14)  $X(E, \Gamma = 0)$  is a quantity corresponding to a perfectly ordered material, whose energy dependence near the Fermi surface is known, and  $\Gamma = \hbar/\bar{\tau}$  is the electron damping. Since the broadening function  $S(E, E', \Gamma)$  depends on  $\Gamma$ , the quantity  $X$  depends on the mean electron lifetime  $\bar{\tau}$ . The latter can be estimated from the Drude plasma frequency  $\Omega_p$  using

$$\rho_n^{-1} = \frac{\langle \Omega_p^2 \rangle \bar{\tau}}{4\pi}, \quad (1.15)$$

which establishes a relation with the normal state resistivity  $\rho_n$ . The BCS expression for the dependence of  $T_c$  on the density of states at the Fermi level  $N(0)$  is

$$k_B T_c = 1.13 \hbar \omega_D e^{-1/VN(0)}, \quad (1.16)$$

---

<sup>2</sup>The non-SI unit  $\mu\Omega \cdot \text{cm}$  is commonly used in literature due to its convenience, which is why it appears in this work as well.

<sup>3</sup>In the paper by Testardi and Mattheiss the expression is cast in a different form. Here the form found in [122] was used.

where  $k_B$  is the Boltzmann constant,  $\omega_D$  is the Debye frequency, and  $V$  is the BCS potential. From (1.16) it is obvious that a broadening in the density of states according to (1.14), which leads to a decrease in  $N(0)$ , causes a reduction of  $T_c$ . Wiesmann et al. estimated the electronic specific heat coefficient  $\gamma$  of irradiated  $Nb_3Sn$  and  $Nb_3Ge$  samples based on measurements of  $B_{c2}(T)$  and  $\rho_n$  using the expression

$$\gamma = C \frac{1}{\eta \rho_n} \left( \frac{dB_{c2}}{dT} \right)_{T=T_c}, \quad (1.17)$$

where  $C$  is a constant, and  $\eta$  is a strong coupling correction factor [142]. They found a significant decrease in the thus obtained  $\gamma$  values with increasing fluence, i.e. increasing disorder. Due to the relationship [82]

$$\gamma = \frac{2}{3} \pi^2 k_B^2 N(0) (1 + \lambda_{ep}), \quad (1.18)$$

in which the factor  $(1 + \lambda_{ep})$  accounts for the strong coupling correction, this decrease in  $\gamma$  is correlated with a decrease in  $N(0)$ . Wiesmann et al. reported that  $\gamma$  is roughly proportional to  $1/\rho_n$ , which supports the concept introduced by Testardi and Mattheiss. Tsuei re-examined these data taking into account changes in the electron-phonon interaction due to increasing disorder [131]. The result of this study was that in  $Nb_3Sn$   $N(0)$  decreases by a factor of approximately 4 as  $T_c$  decreases from 18 K to 3 K due to the introduction of disorder, accompanied by a decrease of the the electron-phonon interaction  $\langle I^2 \rangle$  by a factor of 1.6. In [122] Soukoulis and Papaconstantopoulos calculated  $N(0)$  and other properties of various A-15 compounds based on the Testardi-Mattheiss model and band structure computations. Their calculations predict a decrease of  $N(0)$  and  $T_c$  in  $Nb_3Sn$  and in most of the other examined materials ( $Nb_3Si$  and  $Nb_3Sb$  were the exceptions) with increasing disorder.

Appel derived an expression for the electron-phonon interaction parameter  $\lambda_{ep}$  based on the linear-chain model, and calculated the dependence of the critical temperature of various A-15 compounds on the long range order parameter  $S$  using the McMillan formula [3]. In this work the calculation of  $\lambda_{ep}(S)$  is based on the experimentally determined dependence of the density of states  $N(0)$  on  $S$ , obtained from specific heat measurements. A connection between the disorder induced reduction of  $T_c$  and the electron-phonon interaction was also investigated by Meisel and Cote [85], who treated the problem within the framework of the Eliashberg theory using the Pippard-Ziman condition. The latter states that phonons with wavelengths exceeding the mean free path of electrons are ineffective electron scatterers.



In [86] Mukherjee and Baixeras investigated how changes in the lattice parameter  $a$  affect the electron-phonon interaction parameter  $\lambda_{\text{ep}}$ . They concluded that variations of  $T_c$  with  $a$  can almost completely be accounted for by changes of  $N(0)$  with  $a$ .

In [44] Farrell and Chandrasekhar attributed the changes in  $T_c$  to a damage induced smoothing of the anisotropy of the energy gap. They admitted, however, that this effect can only be a significant mechanism if  $l > \xi_0$ , which does not apply in the dirty limit. Schachinger and Prohammer concluded in their work that anisotropy smoothing may be relevant at small defect concentrations, whereas changes in  $N(0)$  seem to be responsible for the  $T_c$  degradation at higher concentrations [103].

### 1.2.2. Flux pinning in polycrystalline $\text{Nb}_3\text{Sn}$

From an application-oriented point of view the critical current density  $J_c$  at certain values of temperature and magnetic field is usually the most important characteristic of a superconducting wire. It is determined by the pinning of flux vortices in the superconductor, which depends on the microstructure of the material (grain boundaries, precipitates, voids, etc.). The volume pinning force  $F_p$  is the force per unit volume necessary to depin the vortices. Since the resulting vortex motion causes the generation of an electric field and hence a voltage drop along the superconductor, this depinning marks the end of lossless current transport and thus defines the critical current density. The absolute value of  $F_p$  is therefore equal to the Lorentz force per volume  $\vec{J} \times \vec{B}$  at  $|\vec{J}| = J_c$ , and can be expressed as

$$F_p = J_c B \tag{1.19}$$

if  $\vec{J}$  and  $\vec{B}$  are perpendicular, as it is usually the case during transport measurements on superconducting wires. Fietz and Webb found that the pinning force in niobium alloys obeys a scaling law, i.e. the  $F_p(B)$  curves measured at different temperatures exhibit the same functional dependence when plotted as a function of the reduced field  $b = B/B_{c2}$  [45]. Scaling behavior was subsequently identified in many other superconductors including  $\text{Nb}_3\text{Sn}$ . In the present work scaling is treated within the framework of the unified scaling law (USL), which is described in detail in a review article by Ekin [36].

The USL parameterization of the volume pinning force is

$$F_p = K(t, \varepsilon) f(b), \quad (1.20)$$

in which the function  $K(t, \varepsilon)$  describes the pinning force dependence on reduced temperature  $t$  and strain  $\varepsilon$ , whereas the field dependence is given by the pinning force function  $f(b)$ . The reduced field  $b$  used in the USL is given by

$$b = \frac{B}{B_{c2}^*(t, \varepsilon)}, \quad (1.21)$$

where  $B_{c2}^*$  is an effective upper critical field used for scaling (also referred to as scaling field), which is in general not identical to the upper critical field determined experimentally, for instance by means of resistivity measurements. Likewise, the reduced temperature  $t$  is defined by an effective critical temperature  $T_c^*$ :

$$t = \frac{T}{T_c^*(\varepsilon)} \quad (1.22)$$

The field dependence of the pinning force can be expressed as

$$f(b) = b^p (1 - b)^q, \quad (1.23)$$

where the low- and high-field exponents  $p$  and  $q$  must be constant for the pinning force to be shape invariant. If these parameters would exhibit a dependence on field, temperature, or strain, scaling would fail. In polycrystalline Nb<sub>3</sub>Sn (especially binary wires) the experimentally determined exponents are often close to  $p = 0.5$  and  $q = 2.0$ , which is consistent with pinning by core interaction between the vortices and normal conducting surfaces, thus implying grain boundary pinning as the dominant mechanism [30]. This is supported by the observation that the maximum value of the volume pinning force increases as the grain size decreases, as reported by Scanlan et al. [102] as well as others. The reduced field at which  $f(b)$  reaches its maximum is given by

$$b_{\max} = \frac{p}{p + q}. \quad (1.24)$$

In case of pure grain boundary pinning with the scaling exponents  $p = 1/2$  and  $q = 2$  the pinning force maximum occurs at  $b_{\max} = 0.2$ .

Assuming that the temperature and strain dependence of both  $K(t, \varepsilon)$  and  $B_{c2}^*(t, \varepsilon)$  can be

separated, (1.20) can be cast in the convenient separable form [36]

$$F_p = C g(\varepsilon) h(t) f(b). \quad (1.25)$$

In the above expression  $C$  is a constant,  $g(\varepsilon)$  and  $h(t)$  are the dimensionless strain and temperature dependences, and  $f(b)$  is the field dependence given by (1.23). By defining a temperature and a strain part

$$b_{c2}(t) = \frac{B_{c2}^*(t, \varepsilon = 0)}{B_{c2}^*(t = 0, \varepsilon = 0)}, \quad b_{c2}(\varepsilon) = \frac{B_{c2}^*(t = 0, \varepsilon)}{B_{c2}^*(t = 0, \varepsilon = 0)} \quad (1.26)$$

of the effective upper critical field, the USL in its separable form can be represented by five single-variable functions:  $b_{c2}(t)$ ,  $b_{c2}(\varepsilon)$ ,  $g(\varepsilon)$ ,  $h(t)$ , and  $f(b)$ . Since strain scaling was not investigated in the present work, only  $b_{c2}(t)$ ,  $h(t)$ , and  $f(b)$  will be relevant in the following.

The parameterization

$$b_{c2}(t) = 1 - t^\nu \quad (1.27)$$

with  $\nu \approx 1.5$  is commonly used to describe the temperature dependence of the upper critical field, and can be regarded as a good approximation to the theory developed by Maki and de Gennes [36]. It appears in the temperature scaling function of the USL together with the two additional parameters  $\mu$  and  $\eta$ :

$$h(t) = (1 - t^2)^\mu (1 - t^\nu)^{\eta - \mu} \quad (1.28)$$

The term  $(1 - t^2)$  comes from the two-fluid model temperature dependence of the thermodynamic critical field, and the exponent  $\mu$  can take the values 0, 1, or 2, the best choice still being an open question.<sup>4</sup>

Kramer proposed a flux pinning model which assumes that flux motion at low fields occurs primarily due to depinning, whereas synchronous shear of the flux line lattice is the dominant mechanism at high fields [71]. The model predicts the dependence

$$F_p \propto b^{1/2} (1 - b)^2, \quad (1.29)$$

---

<sup>4</sup>According to Ekin [36] the choice of  $\mu$  has little influence on the fitting accuracy at  $T \geq 4$  K, provided  $\eta$  is used as an adjustable parameter.

which combined with  $F_p = J_c B$  leads to

$$J_c^{1/2} b^{1/4} \propto 1 - b. \quad (1.30)$$

Expression (1.30) is the basis of a method known as Kramer plot or Kramer extrapolation, in which  $J_c^{1/2} B^{1/4}$  is plotted versus  $B$  to obtain the effective upper critical field by linear extrapolation of the plotted data to the field axis. Although large deviations of the scaling exponents from the values derived by Kramer ( $p = 1/2$ ,  $q = 2$ ) have been reported [36], Kramer extrapolation is still a widely used tool for obtaining the scaling field (or the upper critical field under the assumption  $B_{c2}(T) \approx B_{c2}^*(T)$ , which may be sufficient for an estimate). In [106] Schmucker proposed a flux pinning model which takes into account the plastic flow of the flux line lattice. The results obtained from this model imply that  $J_c^{1/2} B^{-1/4}$  plotted as a function of  $B$  is linear at high field values, thus providing another extrapolation method.

The scaling field  $B_{c2}^*$  is – independently of whether it is obtained by Kramer extrapolation or another fit procedure – a depinning field which is determined by the main part of the pinning force function  $f(b)$ . The upper critical field  $B_{c2}$ , on the other hand, is defined by the transition from the superconducting to the normal state, and is therefore susceptible to the effects of inhomogeneities which exhibit a higher  $B_{c2}$  value than the bulk material. This can result in a significant deviation from scaling behavior in the high-field part of the pinning force curve, summarized by Ekin with the words “the tail does not scale” [36]. This behavior can be expected to be particularly pronounced in materials containing two or more distinctive grain populations, such as powder-in-tube  $\text{Nb}_3\text{Sn}$  wires (cf. Subsection 2.1.1).

### 1.2.3. Irradiation effects

There is a vast amount of publications on the effects of radiation damage in superconductors, which was a particularly popular subject matter in the 1970s and 80s. Although the present work focuses on fast neutron irradiation, studies on the effects of other types of radiation are also relevant to it, as they are crucial for identifying universal relations which are independent of the radiation type. Due to the mutual similarities between different A-15 compounds an analysis of the effects of irradiation on compounds such as  $\text{V}_3\text{Si}$  can also advance the understanding of radiation effects in  $\text{Nb}_3\text{Sn}$ .

A list of articles discussing irradiation studies on A-15 materials (with no claim to completeness, but certainly diversity) read by the author and referred to in the following is presented in Table 1.1 and Table 1.2. Publications on irradiation studies using reactor neutrons as well as neutrons with higher energies (especially 14.8 MeV radiation) are listed in Table 1.1. Those articles listed under “Fission products” discuss damage caused by neutron irradiation of superconductors which contain fissionable isotopes. Table 1.2 contains the references in which irradiation experiments were carried out using electrons ( $e^-$ ), protons ( $p^+$ ), deuterons ( $d$ ), alpha-particles ( $\alpha$ ), and heavy ions (relative to the other projectiles) such as  $^{16}\text{O}$  and  $^{32}\text{S}$ . Several of these articles refer to the same data, which in some cases were only analyzed but not measured by the respective authors.

	Reactor Neutrons	Neutrons with $E > 14 \text{ MeV}$	Fission products
$\text{Nb}_3\text{Sn}$	[6, 13, 20–23, 28, 40–43, 59, 64, 66–68, 70, 90, 94–97, 112, 113, 115–117, 119, 120, 125, 127, 136]	[56, 58, 117, 139]	[6]
$\text{Nb}_3\text{Ge}$	[20, 31, 125, 127, 136]		
$\text{Nb}_3\text{Ga}$	[125, 127]		
$\text{Nb}_3\text{Al}$	[6, 20, 29, 59, 125–127, 136]		[6, 10]
$\text{Nb}_3\text{Pt}$	[31, 95]		
$\text{Nb}_3(\text{Al}, \text{Ge})$	[6, 125, 127]		[6]
$\text{Nb}_3(\text{Sn}, \text{Ga})$	[118]		
$\text{V}_3\text{Si}$	[6, 20, 72, 73, 83, 84, 95, 105, 125, 133–135]		[6, 10]
$\text{V}_3\text{Ga}$	[67, 112, 113, 125]		
$\text{V}_3\text{Ge}$	[121]		
$\text{Mo}_{0.4}\text{Tc}_{0.6}$	[53]		

**Table 1.1.:** References in which neutron irradiation studies are discussed.

## Changes in the intrinsic properties

A common feature of the effects of radiation on crystalline structures is the introduction of disorder, provided the impinging particles can transfer a sufficient amount of energy

	$e^-$	$p^+$	$d$	$\alpha$	Heavy ions
Nb <sub>3</sub> Sn		[63, 114]	[78]	[98, 141]	[1, 12, 43, 87, 89]
Nb <sub>3</sub> Ge	[101]			[98, 141]	[87, 89]
V <sub>3</sub> Si		[2]		[98]	[1, 87]
V <sub>3</sub> Ga		[114]	[109]		
V <sub>3</sub> Ge				[98]	
Mo <sub>3</sub> Ge				[57]	[76]
Mo <sub>3</sub> Si					[76]

**Table 1.2.:** References in which irradiation studies involving particles other than neutrons are discussed.

to the atoms in the target material. Fast neutrons are particularly convenient for creating homogeneously distributed defects due to their large penetration depth in most materials, which explains their predominance in irradiation studies. Notwithstanding the nature of the introduced defects (e.g. Frenkel pairs, anti-site disorder), it stands to reason that with increasing particle fluence the long range order parameter  $S$  and the mean free path  $l$  of the electrons will decrease. Therefore, the concepts discussed in Subsection 1.2.1, which relate changes in disorder to changes in  $B_{c2}$  and  $T_c$ , should also apply to radiation damaged A-15 compounds.

Such changes were indeed observed in neutron irradiated Nb<sub>3</sub>Sn. Snead and Parkin, for instance, measured changes in the critical current  $I_c$  of multifilamentary Nb<sub>3</sub>Sn wires as a function of fast neutron fluence [116]. They found an increase in  $I_c$  at low fluences (up to  $5 \cdot 10^{21} \text{ m}^{-2}$ ,  $E > 1 \text{ MeV}$ ), followed by a decrease at higher fluences, the effect being more pronounced at high applied fields. Snead and Parkin attributed this behavior to an increase in  $B_{c2}$  caused by an increase in  $\rho_n$ , and a decrease in  $T_c$  at high fluences. The same behavior was observed by Weiss et al. in binary and alloyed multifilamentary Nb<sub>3</sub>Sn wires irradiated with 14 MeV neutrons [139]. They found that the fluence at which the maximum in  $I_c$  occurs is significantly lower for alloyed wires than it is for binary ones ( $1.8 \cdot 10^{21} \text{ m}^{-2}$  as opposed to  $7 \cdot 10^{21} \text{ m}^{-2}$ ). The explanation they gave is that  $\rho_n$  and consequently  $B_{c2}$  is less sensitive to the introduction of disorder in alloyed wires due to their less ordered initial state. This result was confirmed by Hahn et al., who reported that the peak in  $J_c$  occurs at lower fluences with increasing alloy content [58].

In [97] and [96] the sensitivity of Nb<sub>3</sub>Sn and Nb-Ti multifilamentary wires to fast neutron irradiation is compared. The conclusion of these works is that Nb-Ti wires exhibit only a mild reduction in  $I_c$  even at very high fluences ( $6 \cdot 10^{23} \text{ m}^{-2}$ ,  $E > 1 \text{ MeV}$ ), whereas the critical current of Nb<sub>3</sub>Sn wires decreases drastically at fluences exceeding  $2\text{-}3 \cdot 10^{22} \text{ m}^{-2}$ . The fact that in this work no discernible increase in  $I_c$  of Nb<sub>3</sub>Sn was found at low fluences can most likely be explained by the relatively low maximum applied field of 4 T.

Another result presented in [97] is a decrease of the critical temperature of Nb<sub>3</sub>Sn with increasing neutron fluence. In [13] Bett reported a relatively linear decrease of  $T_c$  in Nb<sub>3</sub>Sn up to a fast neutron fluence of roughly  $1.8 \cdot 10^{23} \text{ m}^{-2}$  ( $E > 0.1 \text{ MeV}$ ). The  $T_c$  degradation in multifilamentary Nb<sub>3</sub>Sn was also observed by Hahn [58], who described the dependence of the critical temperature on 14.8 MeV neutron fluence using an exponential fit of the form

$$T_c(\Phi t) = T_c(0) e^{-C\Phi t}. \quad (1.31)$$

In the above expression  $T_c(0)$  is the critical temperature before irradiation, and  $C$  is a fit parameter with a value around  $10^{-23} \text{ m}^2$ . Due to the small value of  $C$  the functional dependence of (1.31) is almost linear at not too high fluences.

Söll et al. studied the  $T_c$  degradation of a Nb<sub>3</sub>Sn wire by means of stepwise fast neutron irradiation [120]. They reported a linear decrease of the critical temperature up to the maximum applied fluence of  $1.05 \cdot 10^{23} \text{ m}^{-2}$  ( $E > 0.1 \text{ MeV}$ ), which appeared to be absent below a fast neutron fluence of  $10^{22} \text{ m}^{-2}$ . The existence of such a “threshold effect” in various A-15 superconductors was suggested by other authors as well, for instance in [125] and [13]. In some cases this effect can probably be attributed to the limited accuracy of the measurement method or to an unwary interpretation of plots with a logarithmic fluence scale.

Pande, however, developed a model which could explain a real threshold effect in the  $T_c$  degradation by assuming that the irradiated superconductor consists of strongly disordered regions (defect cascades) embedded in a much less disordered matrix [94]. The critical temperature of these disordered regions is significantly lower than that of the matrix, but as long as their distance is large enough, the bulk  $T_c$  value of the whole system will exhibit only a very slight decrease relative to the matrix  $T_c$  due to the proximity effect. However, when the distance between the disordered regions is smaller than the coherence length, the critical temperature of the system will be strongly depressed. Viswanathan et al. reported

agreement between their measurement results on  $V_3Si$  and the model proposed by Pande [135]. They argued that the existence of the threshold effect depends on the initial purity of the samples, since randomly distributed impurities of sufficient density have the same depressing effect on  $T_c$  as regions damaged by radiation.

According to Aronin [4] the change in the long range order parameter  $S$  with increasing fast neutron fluence is governed by an exponential function:

$$S(\Phi t) = S(0) e^{-k\Phi t} \quad (1.32)$$

In (1.32) the factor  $S(0)$  is the initial long range order parameter, and  $k$  is a material dependent constant. Sweedler et al. [127] found an exponential dependence of the critical temperature of  $Nb_3Sn$  on  $S$ :

$$T_c(\Phi t) = T_c(0) e^{-C(1-S/S(0))} \quad (1.33)$$

They assumed an initial long range order parameter  $S(0) = 1$ , and found a value of  $5.0 \pm 1.5$  for the constant  $C$ . Maier and Seibt [78] reported the relationship

$$\ln\left(\frac{T_c(\Phi t)}{T_c(0)}\right) = -C(1 - e^{-k\Phi t}) \quad (1.34)$$

with the fit parameters  $C$  and  $k$  for  $Nb_3Sn$  irradiated with 50 MeV deuterons up to a fluence of  $2.3 \cdot 10^{22} \text{ m}^{-2}$ , in agreement with (1.32) and (1.33). It stands to reason that at low enough fluences the linear dependence found by Bett [13], the exponential dependence (1.31) reported by Hahn [58], and expression (1.34) are equally good descriptions for the experimentally determined fluence dependence of the critical temperature.

In [125] Sweedler et al. discussed measurements of  $T_c$ ,  $S$ , and the lattice parameter  $a$  of various neutron irradiated A-15 compounds. They found that a decrease in  $T_c$  is accompanied by a decrease in  $S$  as well as a slight increase in  $a$ . A plot showing the correlation between  $T_c$  and  $a$  in neutron irradiated  $Nb_3Al$  was given by Sweedler and Cox in [126]. Such a correlation can also be observed if the damage is not introduced by fast neutrons but for instance by 20 MeV sulfur ions as reported by Nölscher and Saemann-Ischenko [89]. Since the normal state resistivity  $\rho_n$  rises with increasing disorder,  $T_c$  and  $\rho_n$  should change in opposite ways with increasing radiation damage. Such behavior was indeed found, for instance in proton irradiated  $V_3Si$  [2], in sulfur ion irradiated  $Nb_3Sn$  and  $V_3Si$  [1], in alpha-particle irradiated  $Nb_3Sn$  and  $Nb_3Ge$  [141], and also in electron irradiated



Nb<sub>3</sub>Ge [101]. The martensitic transformation temperature  $T_M$  was found to decrease due to neutron irradiation in Nb<sub>3</sub>Sn as well as V<sub>3</sub>Si, leading to a suppression of the transformation at high fluences [115, 133].

Fähnle calculated the influence of disorder on the critical temperature of A-15 superconductors based on the Labbé-Friedel-van Reuth theory [74, 75], assuming that the Fermi level is localized near a sharp peak in the electronic density of states [41]. The calculated  $T_c$  dependence was found to be in good qualitative agreement with data on neutron irradiated Nb<sub>3</sub>Sn, if statistically distributed atomic defects (anti-site disorder) were assumed, which also supports the very general concept introduced by Testardi and Mattheiss (cf. Subsection 1.2.1). The assumption that all displaced atoms are confined to spherical clusters with a diameter of 3 nm, however, lead to a much too small  $T_c$  depression with increasing fluence.

The extensive experimental data on both irradiation damaged and chemically disordered A-15 compounds clearly suggests that a decrease of the critical temperature with decreasing long range order parameter, which manifests itself in an increase of the normal state resistivity, is a universal behavior of most A-15 materials, and is independent of the damage mechanism. Based on the observation that the degradation of  $T_c$  is not significant at fast neutron fluences around  $10^{22} \text{ m}^{-2}$ , and that a peak in  $J_c$  is usually found somewhere not too far from this value, fluence ranges in literature are often somewhat arbitrarily divided into a low-fluence regime ( $\lesssim 10^{22} \text{ m}^{-2}$ ) and a high-fluence regime ( $\gtrsim 10^{22} \text{ m}^{-2}$ ).

### Defect structure

Since effective pinning requires structures with sizes comparable to or larger than the coherence length as well as physical properties which differ significantly from those of the surrounding material, it stands to reason that the nature of radiation induced defects is highly relevant to their influence on the critical current density. The basics of radiation damage were discussed by Kinchin and Pease in [69]. According to them a collision between a fast neutron and an atom in a solid results in a transfer of kinetic energy from the neutron to the atom, which is subsequently distributed among other atoms in the vicinity. The number of atoms displaced in this way in each fast neutron collision is given by

$$N = \frac{E_{\max}}{4E_d}. \quad (1.35)$$

In this expression  $E_d$  is the displacement energy, which is the (average) energy required to displace an atom in the target material from its lattice site, and  $E_{\max}$  is the maximum energy which can be transferred by the impinging neutron with energy  $E$ :

$$E_{\max} = 4E \frac{M_n M_a}{(M_n + M_a)^2} \quad (1.36)$$

In (1.36)  $M_n$  is the neutron mass, and  $M_a$  is the mass of the target atom. In case of  $\text{Nb}_3\text{Sn}$  a reasonable value for  $M_a$  is the average mass of Nb and Sn atoms, weighted by their atomic fractions in the material, which gives  $M_a = 99.4$  u. The maximum in the fast neutron flux distribution of the reactor at the *Atominstitut* is located at  $E \approx 2$  MeV (cf. Section 2.3 and [137]). Using this value, expression (1.36) results in  $E_{\max} \approx 79$  keV. A large uncertainty lies in the displacement energy  $E_d$ , which is not an easy parameter to determine. Using the value  $E_d = 78$  eV for Nb given in [19], and  $E_{\max} = 79$  keV, gives  $N = 253$  according to (1.35). Assuming that all these displacements are confined to a spherical volume, and using a typical  $\text{Nb}_3\text{Sn}$  lattice constant of  $a = 0.529$  nm [50], yields defects with an average diameter of approximately 2 nm.

Holdway found disordered regions with sizes between 2 and 10 nm as well as dislocation loops with diameters between 15 and 30 nm in fast neutron irradiated  $\text{Nb}_3\text{Sn}$  by means of transmission electron microscopy (TEM) [64]. The loop density was estimated to be between  $10^{20}$  and  $10^{21} \text{ m}^{-3}$  after the samples had been exposed to a fast neutron fluence of roughly  $3 \cdot 10^{22} \text{ m}^{-2}$  ( $E > 0.7$  MeV). Föhnle reported “spots” in TEM images with diameters of approximately 10 nm, and a density of  $5 \cdot 10^{21} \text{ m}^{-3}$  in  $\text{Nb}_3\text{Sn}$  irradiated to a fast neutron fluence of  $10^{22} \text{ m}^{-2}$  (energy scale unknown) [40]. Pande estimated the volume fraction of disordered regions identified with TEM in fast neutron irradiated  $\text{Nb}_3\text{Sn}$ , and reported a value of roughly 2% at a fluence of  $10^{22} \text{ m}^{-2}$  ( $E > 1$  MeV) [95]. Unfortunately, the average defect size was not specified in this publication. Assuming spherical defects with a diameter of 10 nm, the volume fraction reported by Pande corresponds to a defect density of  $4.8 \cdot 10^{21} \text{ m}^{-3}$ , in agreement with the value claimed by Föhnle. However, using a value of 2 nm as estimated above would result in a density of  $6 \cdot 10^{23} \text{ m}^{-3}$ .

Küpfer and Manuel reported dislocation loops with an average diameter of 16 nm as well as “black dots” in TEM images of neutron irradiated  $\text{V}_3\text{Si}$  [72]. For the density of the loops in the low-fluence regime they found the fit formula

$$n_{\text{loops}} = (4.65 \text{ m}^2 \Phi_f t)^{0.82} \text{ m}^{-3}, \quad (1.37)$$

in which  $\Phi_f t$  is the fast neutron fluence for neutrons with  $E > 1$  MeV. This loop density is between one and two orders of magnitude lower than the estimation given by Holdway.

As discussed in many works on irradiated A-15 superconductors, the critical temperature can be recovered by annealing [13, 64, 66, 84, 89, 112, 125–127]. Bett found that even in heavily radiation damaged  $\text{Nb}_3\text{Sn}$   $T_c$  recovers completely when the samples are annealed at 900 °C for 2 hours, whereas annealing at significantly lower temperatures leads to an incomplete recovery [13]. In [127] Sweedler et al. attributed the reversibility of the radiation induced  $T_c$  degradation to anti-site disordering ( $A$  atoms occupying  $B$  sites and vice versa) and subsequent reordering during annealing. The reordering kinetics during annealing of A-15 compounds was investigated by Dew-Hughes, who compared results on splat-quenched and neutron irradiated materials [31].

Sweedler and Cox pointed out that the change in the lattice parameter  $a$  observed in neutron irradiated  $\text{Nb}_3\text{Al}$  is consistent with anti-site disordering, which leads to a lattice expansion due to the different radii of Nb and Al atoms [126]. Shiota found in isochronal annealing studies on neutron irradiated  $\text{V}_3\text{Ga}$  that the  $T_c$  recovery rate reaches its maximum between 400 and 500 °C, and that the transition width  $\Delta T_c$  peaks in the same temperature range [112]. Karkin et al. also observed such a peak in  $\Delta T_c$  in neutron irradiated and isochronally annealed  $\text{Nb}_3\text{Sn}$  around 700 °C, coinciding with the maximum in the  $T_c$  recovery rate [66].

Meier-Hirmer et al. investigated the effects of isochronal annealing on  $T_c$ ,  $B_{c2}$ , and  $J_c$  of neutron irradiated  $\text{V}_3\text{Si}$  [84]. They found that  $T_c$  and  $B_{c2}$  recover between 530 and 630 °C, whereas the critical current density at low fields drops below its original value between 630 and 830 °C. Their  $\Delta T_c$  measurements show two peaks, one in each of these temperature ranges. The authors attributed this recovery behavior to the existence of two different kinds of defects, one responsible for the  $T_c$  degradation, the other for the increase in  $J_c$  due to improved pinning. They suggested that dislocation loops might be the pinning relevant defect type.

Since annealing clearly has an effect on the defect structure of irradiated A-15 materials, it stands to reason that the temperature at which the irradiation is performed affects the outcome. Guinan et al. reported that annealing at 300 K results in minor changes of the critical current (roughly 10% at high fields) of  $\text{Nb}_3\text{Sn}$  wire samples irradiated with 14.8 MeV neutrons to a fluence of  $1.35 \cdot 10^{22} \text{ m}^{-2}$  at a temperature between 4 and 5 K [56]. Brown et al. found a  $J_c$  recovery of roughly 25% at low applied fields in multifilamentary  $\text{Nb}_3\text{Sn}$

wires irradiated at 6 K to a fluence of  $1.8 \cdot 10^{22} \text{ m}^{-2}$  ( $E > 0.1 \text{ MeV}$ ) after room temperature annealing [23]. In [22] Brown et al. compared the  $J_c$  enhancement in monofilamentary  $\text{Nb}_3\text{Sn}$  wires after fast neutron irradiation at 6 K and at 350 K. In samples with a high initial  $J_c$  value they found that the  $J_c$  enhancement is approximately 10% higher at low fields when the irradiation is performed at 6 K as opposed to 350 K. The irradiation temperature appeared to have little effect on the  $J_c$  enhancement in low- $J_c$  samples, however, the enhancement was much more pronounced in these samples. An insignificant  $J_c$  recovery of a few percent after room temperature annealing was reported by Snead for  $\text{Nb}_3\text{Sn}$  wire samples irradiated with 30 GeV protons at a temperature of 4.2 K [114]. Adrian et al. reported a small effect of room temperature annealing on  $T_c$  and  $\rho_n$  of  $\text{Nb}_3\text{Sn}$  and  $\text{V}_3\text{Si}$  irradiated with 20 MeV sulfur ions at temperatures below 20 K [1].

### Pinning by radiation induced defects

Radiation induced defects with dimensions comparable to the Ginzburg-Landau coherence length  $\xi_{\text{GL}}$  can be regarded as regions with different material properties (in the extreme case normal conducting behavior) than the surrounding matrix. Due to the difference in free energy between these regions and the matrix, they exert an attractive force on flux vortices, thus acting as pinning centers. It stands to reason that a sufficient density of such defects will have a significant effect on the volume pinning force  $F_p$ , which can be determined experimentally.

Indeed, changes in magnitude and functional dependence of the pinning force were reported in literature. Guinan et al. reported an increase of the  $F_p$  maximum in  $\text{Nb}_3\text{Sn}$  by a factor of two after 14.8 MeV neutron irradiation to a fluence of  $1.35 \cdot 10^{22} \text{ m}^{-2}$ , accompanied by a shift of the maximum position from  $b_{\text{max}} = 0.23$  to 0.30 [56]. Such a shift was also observed by Seibt in  $\text{V}_3\text{Ga}$  irradiated with 50 MeV deuterons [109]. Seibt reported good agreement with the Kramer model (scaling exponents  $p = 1/2$  and  $q = 2$ , as discussed in Subsection 1.2.2) in the unirradiated state, whereas a high-field exponent of  $q = 1$  produced better agreement after irradiation to a fluence of  $2.6 \cdot 10^{21} \text{ m}^{-2}$ . According to (1.24) this corresponds to  $b_{\text{max}} = 0.2$  in the unirradiated state, and  $b_{\text{max}} = 0.33$  after irradiation. In [118] Snead and Suenaga reported deviations from Kramer scaling in fast neutron irradiated  $\text{Nb}_3(\text{Sn,Ga})$ , identified by plotting  $F_p$  as a function of  $b^{1/2}(1-b)^2$ . While this plot was in good approximation linear for an unirradiated sample, it showed severe deviations from linearity with increasing fluence.

Brown et al. developed a model aimed at explaining the changes in the volume pinning force they found in Nb<sub>3</sub>Sn irradiated with fast neutrons [23]. They assumed that the volume pinning force is proportional to a function  $A(d)$  describing the microstructure dependent pinning strength and a function akin to (1.23), which depends on the reduced field:

$$F_p \propto A(d) b^n (1 - b)^2, \quad (1.38)$$

The expression for the dependence of the volume pinning force on fast neutron fluence relative to its unirradiated value  $F_p(0)$  given by Brown et al. is

$$\frac{F_p(\Phi_f t)}{F_p(0)} = 1 + \Phi_f t \left( C_1 \frac{\partial \ln(T_c)}{\partial (\Phi_f t)} + C_2(b) \frac{\partial \ln(B_{c2})}{\partial (\Phi_f t)} + C_3 \frac{\partial \ln(A(d))}{\partial (\Phi_f t)} \right), \quad (1.39)$$

where  $C_1$  and  $C_3$  are constants, and  $C_2(b)$  is a function which takes on negative values at low fields and positive values at high fields. A saturation in the pinning force due to additional defects can be expected when these defects begin to overlap, which should be reflected in the behavior of the third term in (1.39). The observed decrease of  $F_p$  at high fluences is explained by the  $T_c$  reduction described by the first term.

The exponent  $n$  in (1.38) clearly corresponds to the low-field exponent  $p$  in (1.23), and the high-field exponent was fixed to the value  $q = 2$ . In the derivation of (1.39) Brown et al. used the simplifying assumption that these exponents do not change with fluence. The need for a field dependent function  $C_2(b)$  for explaining the observation that  $F_p(\Phi_f t)$  increases at high fields but decreases at low fields is a direct result of this simplification. A more physically sound approach would be to assume that the scaling exponents  $p$  and  $q$  are fluence dependent.

This assumption was made by Okada et al., who used

$$F_p = C b^p (1 - b)^q, \quad b = \frac{B}{B_{c2}^*} \quad (1.40)$$

with the fit parameters  $C$ ,  $B_{c2}^*$ ,  $p$ , and  $q$  to describe the pinning force in fast neutron irradiated multifilamentary Nb<sub>3</sub>Sn wires [90]. Their fits yielded the results  $p = 0.50$ ,  $q = 1.9$  in the unirradiated state, and  $p = 0.87$ ,  $q = 2.0$  after irradiation to a fluence of  $3.8 \cdot 10^{22} \text{ m}^{-2}$  ( $E > 0.1 \text{ MeV}$ ). This corresponds to a shift of the maximum in  $F_p$  from  $b_{\max} = 0.21$  to  $b_{\max} = 0.30$ . The value of  $B_{c2}^*$  exhibited only a minor increase from 22.0 T to 23.1 T.

Küpfer et al. proposed that the changes in the volume pinning force of irradiated A-15

compounds can be modeled by simply adding two terms which describe the contributions of grain boundaries and dislocation loops, respectively [73]. They reported that the maximum in the pinning force contribution stemming from the loops is located at  $b = 0.45$ , but gave no explicit expression for this term. Maier and Seibt, while not specifying the nature of the radiation induced defects, used the same two-component ansatz to describe the volume pinning force in 50 MeV deuteron irradiated Nb<sub>3</sub>Sn [78].

Dew-Hughes estimated the elementary pinning force of different types of defects by assuming that the pinning force per unit length  $f_p$  equals the energy per unit length  $\Delta W$  required for depinning, divided by the effective range of the pinning interaction  $x$  [30]:

$$f_p = \frac{\Delta W}{x} \quad (1.41)$$

When the size of a defect is small compared to the Ginzburg-Landau penetration depth, the pinning arises primarily from the difference in free energy between the pinning center and the surrounding matrix, which Dew-Hughes refers to as core interaction. In this case  $\Delta W$  is equal to the change  $\Delta g$  in the Gibbs function per unit length  $g$ , which can be approximated by

$$g = \frac{-\pi \xi_{GL}^2 B_c^2 (1-b)^2}{2.32 \mu_0 (2\kappa^2 - 1)}. \quad (1.42)$$

For normal conducting pinning centers  $\Delta g$  is equal to  $g$ , and hence  $\Delta W = g$ . In case of  $\Delta\kappa$ -pinning (1.42) must be differentiated with respect to  $\kappa$  to obtain an expression for  $\Delta g$ . For spherical pinning centers the interaction range  $x$  in (1.41) should be equal to the radius of the defect. By assuming that the length of pinned flux lines per unit volume is proportional to the total length of flux lines per unit volume  $B/\Phi_0$ , Dew-Hughes found the field dependence

$$F_p \propto b(1-b)^2 \quad (1.43)$$

for point-like (small compared to the flux line spacing) defects which exert a pinning force by normal core interaction. This result corresponds to the scaling exponents  $p = 1$  and  $q = 2$  within the framework of the unified scaling law (cf. Subsection 1.2.2). A more in-depth analysis by Föhnle including a Gaussian distribution of the defect sizes yielded a rather complex field dependence of the volume pinning force, which strongly depends on the defect size distribution [39]. Consequently, Föhnle concluded, a description based on

a simple scaling law is likely to fail.

When a reasonable estimate for the elementary pinning force exists, it is easy to calculate an upper limit for the volume pinning force, provided the defect density is known with sufficient accuracy. This upper limit is given by the direct summation of the pinning forces exerted by each defect, thus yielding

$$F_p = n l_p f_p, \quad (1.44)$$

where  $f_p$  is the elementary pinning force per unit length (1.41),  $n$  is the defect density, and  $l_p$  is the length of pinned flux line per defect, which can be assumed to be equal to the defect diameter. Föhnle calculated an upper limit for the volume pinning force due to radiation induced defects of  $F_p(b = 0.2) = 1.15 \cdot 10^{11} \text{ N/m}^3$  for  $\text{Nb}_3\text{Sn}$  exposed to a fast neutron fluence of  $10^{22} \text{ m}^{-2}$  (estimated defect density  $5 \cdot 10^{21} \text{ m}^{-3}$ ) [40]. This value is comparable to typical volume pinning forces in unirradiated  $\text{Nb}_3\text{Sn}$  wires, which means that the maximum volume pinning force would be roughly doubled due to the contribution of radiation induced defects at  $\Phi_f t = 10^{22} \text{ m}^{-2}$ .

The derivation of the volume pinning force  $F_p$  from the elementary pinning force  $f_p$  and the density of pinning centers is known as the summation problem, and is unsolved as of this writing. It was suggested by Meier-Hirmer et al. based on examinations of fast neutron irradiated  $\text{V}_3\text{Si}$  that the volume pinning force exhibits a quadratic dependence  $F_p \propto n^2$  on the density of defects at low defect concentrations or at low fields, whereas at larger concentrations or higher fields the exponent of  $n$  becomes increasingly smaller [83]. Küpfer and Manuel found that neither direct summation nor the statistical summation model developed by Labusch are appropriate for calculating the volume pinning force in neutron irradiated  $\text{V}_3\text{Si}$  [72].





## 2. Sample Specifications and Preparation

Five types of multifilamentary Nb<sub>3</sub>Sn wires were included in the measurement program of this work, whose aim is outlined in Chapter 1. While all of them are state-of-the-art superconductors, they differ in terms of production process and composition. The wires were fabricated by different manufacturers, and the heat treatments necessary to produce the Nb<sub>3</sub>Sn phase were performed at *CERN* before the samples were shipped to the *Atominstitut*. The internal structure of the different wire types and the heat treatments they were subjected to are described in Section 2.1. The preparation of samples for different purposes and the irradiation procedure to which some of the samples were subjected are discussed in Section 2.2 and Section 2.3.

### 2.1. Specifications

The five wire types examined in the present work are described in the following. The most important characteristics of the wires as well as the method used to obtain the sub-element diameters are discussed in Subsection 2.1.1. For completeness, details on the heat treatments necessary to form the Nb<sub>3</sub>Sn sub-elements inside the wires are listed in Subsection 2.1.2.

#### 2.1.1. Wire types

Two of the five examined wire types are restack rod processed (RRP) strands, one alloyed with tantalum, the other with titanium. Two wires, both of which are alloyed with tantalum, were produced by the powder-in-tube (PIT) process. The fifth wire type is an unalloyed

(binary) prototype internal tin (IT) strand. What all five wire types have in common is that their  $\text{Nb}_3\text{Sn}$  sub-elements are surrounded by Nb diffusion barriers, and embedded in a copper matrix. To keep the sample labeling short and simple, three-letter designations were assigned to the five wire types. Two of them are “RRP” (referring to the Ta alloyed restack rod processed wire) and “PIT” (Ta alloyed powder-in-tube wire with a diameter of 1 mm), simply because in the early stage of this work these were the only wire types to be examined. Later on these designations were maintained anyhow to avoid confusion. The other three-letter designations are “TiR” (Ti alloyed restack rod processed wire), “BIN” (binary wire), and “P07” (Ta alloyed powder-in-tube wire with a diameter of 0.7 mm). Sample names are composed of the three-letter wire designation and a suffix which identifies the individual sample, e.g. TiR-2 is a magnetization sample of the TiR wire type with the number 2, and P07-T4 is a P07 type transport sample with the number 4.

Table 2.1 lists the most important specifications of the five wire types. The diameters refer to the heat treated wires (cf. Subsection 2.1.2), and the column “TPL” contains the twist pitch lengths of the twisted sub-elements. A feature common to all wire types is that the superconducting A-15 phase exists in the form of tubular sub-elements. For the wires produced by the powder-in-tube process this is to be expected, whereas for other wire types it means that the individual filaments have completely coalesced during the heat treatment.

Designation	$\emptyset$ (mm)	Sub-elements	Additive	TPL (mm)	$\rho_i$ ( $\mu\text{m}$ )	$\rho_o$ ( $\mu\text{m}$ )
RRP	0.82	54	Ta	12	42.1	74.3
PIT	1.03	192	Ta	24	24.7	45.0
TiR	0.82	108	Ti	14	30.7	53.4
BIN	1.25	246	—	55	34.0	53.9
P07	0.72	114	Ta	N/A	23.3	41.0

**Table 2.1.:** Specifications of the five examined types of  $\text{Nb}_3\text{Sn}$  multifilamentary wires.

The inner and outer sub-element radii  $\rho_i$  and  $\rho_o$  are required for the evaluation of the critical current density from magnetometry data, which is described in Subsection 3.4.1. They were determined from scanning electron microscope (SEM) images provided by CERN. In these images the A-15 region of the sub-elements can be distinguished from the other materials (Nb diffusion barrier around each sub-element, unreacted region in the sub-element

center, and copper matrix) by its gray-scale value. Since the magnification of the images was known, the A-15 area of a sub-element  $A_{A-15}$  could be calculated by counting the pixels within a certain gray-scale range. The area of the “void” in the sub-element center  $A_{void}$  was then obtained by counting the pixels within the inner boundary of the previously determined A-15 area. Based on the assumption that the inner and outer boundary of the A-15 region are concentric circles, the radii can be calculated:

$$\rho_i = \sqrt{\frac{A_{void}}{\pi}}, \quad \rho_o = \sqrt{\frac{A_{A-15} + A_{void}}{\pi}} \quad (2.1)$$

This pixel counting procedure was done on five sub-elements of each sample type in order to obtain the average values listed in Table 2.1. Figure 2.1(a) shows an SEM image of the cross section of the entire P07 wire, whereas Figure 2.1(b) shows a single sub-element of the TiR wire. Although the sub-element of this wire (and also the RRP wire type) is hexagonal in shape, an effective inner and outer radius were used for the critical current density evaluation.

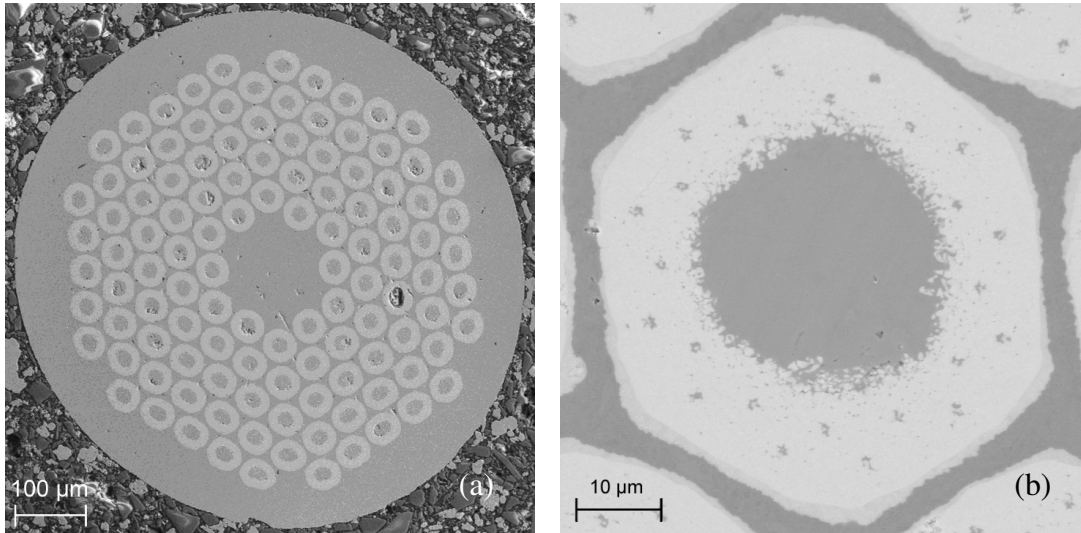


**Figure 2.1.:** SEM images of wire cross sections. **(a)** Entire P07 wire. **(b)** TiR sub-element.

The formation of  $Nb_3Sn$  grains and intermediate phases during the heat treatment is a complex subject, as discussed by Scheuerlein et al. [104] as well as Thilly et al. [129], who examined the processes occurring during different heat treatments on some of the sample types examined in the present work. Without going into details which are not relevant to the present work, it is important to know that wires produced by the powder-in-tube process (the types PIT and P07) possess a layer of significant thickness consisting

of large columnar grains near the inner boundary of each sub-element [54]. The rest of their A-15 region (and in the other three wire types the majority of it) is made up of small equiaxed grains. According to Senatore and Flükiger the small grains in state-of-the-art wires have diameters of about 200 nm, whereas the large grains are up to 2  $\mu\text{m}$  in size, and the two grain populations differ significantly in their intrinsic properties [111]. They reported two peaks in the critical temperature distribution corresponding to small grains (lower  $T_c$ ) and large grains ( $T_c$  higher by a few 100 mK), respectively, whose separation is dependent on the heat treatment. The extrapolated  $B_{c2}$  values were found to be higher in small grains by up to 6 T, which is consistent with a lower degree of atomic order due to a Sn content significantly below the stoichiometric value (cf. Subsection 1.2.1).

Since large grains do not contribute significantly to the pinning force due to their small surface-to-volume ratio (cf. Subsection 1.2.2 and [102]), using the entire A-15 cross section in (2.1) may lead to erroneous results when the thus obtained  $\rho_i$  and  $\rho_o$  values are used in the critical current density evaluation described in Subsection 3.4.1. This shortcoming may be rectified by introducing a correction factor determined from transport measurements, as described in Subsection 3.4.6. The dual grain morphology of PIT and P07 type samples has to be taken into account in the critical temperature evaluation, as described in Subsection 3.4.7.

### 2.1.2. Heat treatments

The wires examined in this work were shipped to *CERN* by the manufacturers in their unreacted state, and the heat treatments were carried out there. Since the A-15 region which is formed during the heat treatment is very brittle, the wire samples have to be shaped as desired before the reaction. For the production of samples for magnetization and upper critical field measurements (cf. Subsection 2.2.1 and Subsection 2.2.3) straight pieces of wire, a few centimeters in length, were heat treated. Wire samples intended for transport measurements were wound on barrels specifically designed for this purpose, as described in Subsection 2.2.2. The heat treatments performed on each type of wire are listed in Table 2.2.

RRP	PIT	TiR	BIN	P07
695 °C (17 h)	625 °C (250 h)	210 °C (48 h)	215 °C (24 h)	620 °C (120 h)
		400 °C (48 h)	340 °C (24 h)	640 °C (120 h)
		665 °C (50 h)	400 °C (24 h)	
			645 °C (50 h)	

**Table 2.2.:** Temperatures and durations of the heat treatments to which the different wire types were subjected.

## 2.2. Preparation

The following sub-sections describe the preparation of samples intended for different purposes. Moreover, they list the designations of all samples measured in the course of this work.

### 2.2.1. Samples for magnetization measurements

As already mentioned in Subsection 2.1.2, straight pieces of wire with lengths of a few centimeters were heat treated at *CERN* to produce samples intended for magnetization measurements. These wire pieces were then shipped to the *Atominstitut*, where samples with a length of approximately 4 mm, appropriate for measurements in a SQUID magnetometer (cf. Section 3.1), were cut from them. The cutting was done perpendicular to the wire axis with a low-speed diamond saw at roughly 150 rpm. A photograph of some of the thus obtained samples is shown in Figure 2.2(a), and Table 2.3 contains a list of all samples examined by means of magnetization measurements. Some of the sample numbers are missing because these samples were used for other purposes such as extracting sub-elements by etching away the copper matrix with nitric acid. These sub-elements, some of which are shown in Figure 2.2(b), were used for comparative magnetization measurements.

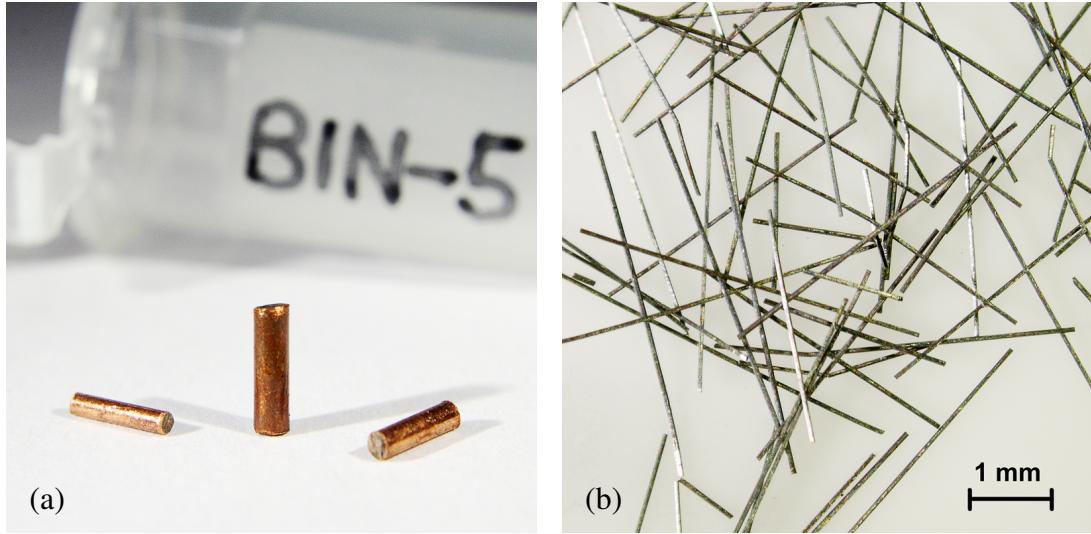


**Figure 2.2.:** Samples used for magnetization measurements. **(a)** Short wire samples of different types. **(b)** Chemically extracted sub-elements of the BIN wire.

RRP	PIT	TiR	BIN	P07
RRP-1	PIT-1	TiR-1	BIN-1	P07-1
RRP-2	PIT-2	TiR-2	BIN-2	P07-2
RRP-3	PIT-3	TiR-3	BIN-3	P07-3
RRP-4	PIT-4	TiR-7	BIN-5	P07-4
RRP-5	PIT-5	TiR-8		
RRP-7				

**Table 2.3.:** List of all samples used for magnetization measurements.

### 2.2.2. Samples for transport measurements

For transport measurements with the 1000 A sample rod, which are described in Subsection 3.3.1, the wire samples had to be wound on barrels composed of Ti-6Al-4V alloy. This material exhibits a thermal contraction very similar to that of Nb<sub>3</sub>Sn when it is cooled down to low temperatures, and is mechanically very stable. Grooves were machined into the material for supporting the wire, and copper rings were mounted on either side to serve as terminals for connecting the wire sample to the sample rod. The production of these barrels as well as the wire mounting took place at *CERN*. After the heat treatments had been completed, solder connections between the wire samples and the copper rings were established, and the finished transport samples were shipped to the *Atominstitut*.

Figure 2.3 shows a photograph of a P07 type transport sample. The barrel has an outer diameter of 23 mm, and possesses grooves for five windings. One additional winding of wire is wound on the copper rings on either side and soldered to them with Sn60Pb40 solder. In doing so, a reliable electric connection between the copper rings and the wire is established, and current transfer problems (cf. [34] and [37]) are avoided. A list of all transport samples measured in the course of this work is given in Table 2.4.



**Figure 2.3.:** Wire sample for transport measurements mounted on a Ti-6Al-4V barrel equipped with copper rings for electric connection.

RRP	TiR	P07
RRP-T1	TiR-T1	P07-T1
	TiR-T2	P07-T2
		P07-T3
		P07-T4

**Table 2.4.:** List of all samples used for transport measurements.

### 2.2.3. Samples for upper critical field measurements

The samples used for the upper critical field measurements described in Subsection 3.3.2 were cut from the same straight pieces of wire which were used for the production of magnetization samples. One sample with a length of roughly 2 cm, which is convenient for this kind of measurement, was cut from each wire type. These samples were simply cut with a wire cutter, since clean cuts are not important for resistivity measurements, contrary to magnetometry aimed at the evaluation of the critical current density. The samples intended for upper critical field measurements were named RRP-R1, PIT-R1, TiR-R1, BIN-R1, and P07-R1.

Some of the magnetization samples listed in Subsection 2.2.1 were also used for upper critical field measurements, as discussed in Subsection 3.3.2, which had initially not been intended. This was done to assess the upper critical field of irradiated samples without having to irradiate longer samples.

## 2.3. Irradiation procedure

The fast neutron irradiation of wire samples was carried out in the *TRIGA Mark-II* reactor at the *Atominstitut*, which is depicted in Figure 2.4. For that purpose the samples were sealed in quartz tubes, which were then placed in irradiation capsules made of aluminum, and inserted into the central irradiation facility of the reactor. Transport samples were sealed by the company *Linder Labortechnik*, since this was not possible at the *Atominstitut* due to the large quartz tube diameter required to accommodate these samples. After exposure to the neutron flux prevalent in the central irradiation facility for the desired duration, the capsule is removed from the reactor core, but remains in the water tank until a



reasonable decay time has passed. The samples can then be extracted and stored in a room equipped with appropriate radiation shielding until they are needed for measurements.

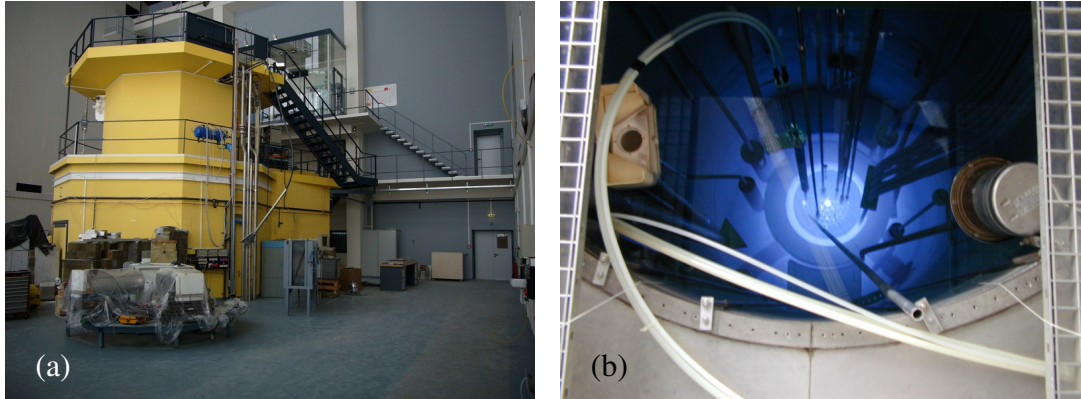


**Figure 2.4.:** Photographs of the *TRIGA Mark-II* reactor at the *Atominstitut*. (a) Reactor hall. (b) Core during operation, viewed from the top of the reactor.

In this work the fast neutron flux density  $\Phi_f$  is defined as that part of the total neutron flux density  $\Phi$  comprised of particles with kinetic energies  $E > 0.1$  MeV. At the time of the irradiation program described herein its value was approximately  $4.5 \cdot 10^{16} \text{ m}^{-2}\text{s}^{-1}$ . The neutron spectrum of the reactor was determined by Weber et al. in the 1980s [137], and is depicted in Figure 2.5. While the absolute value of the fast neutron flux density has changed significantly since then, the energy distribution can be expected to be almost identical in the fast neutron regime. A different definition of  $\Phi_f$  is used in some publications, especially  $E > 1$  MeV is common. For the *TRIGA Mark-II* reactor in Vienna the ratio  $\Phi(E > 0.1 \text{ MeV}) / \Phi(E > 1 \text{ MeV})$  is around 1.9 [137].

Sequential irradiation with relatively small step sizes was used to assess the changes of the intrinsic properties and the pinning behavior of the samples as a function of fast neutron fluence, which is given by  $\Phi_f t$ , the product of fast neutron flux density and irradiation time. The actual value of  $\Phi_f$  depends on a number of parameters such as the exact sample position, the void fraction (the contents of the capsule displace the water needed for moderation), and the time of week (due to reactor poisoning, e.g. by a build-up of  $^{135}\text{Xe}$ ). Therefore, the fast neutron fluence was measured by including a nickel monitor sample in each irradiation step.

These monitor samples were cut from a high-purity Ni foil, and had a mass of roughly 5 mg on average. They allow the assessment of the fast neutron fluence using the reaction  $^{58}\text{Ni}(n,p)^{58}\text{Co}$ , which has a threshold energy of approximately 1 MeV. The  $^{58}\text{Co}$  content

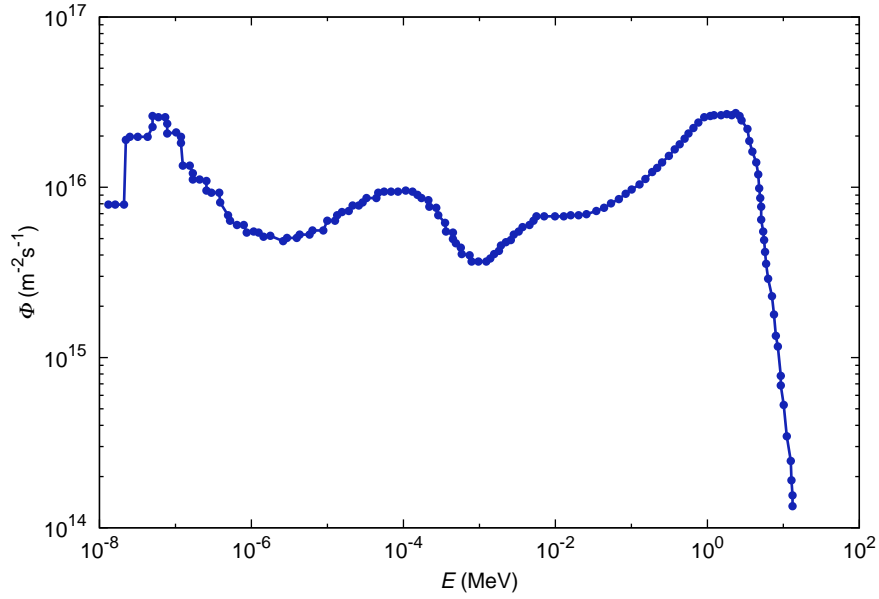


**Figure 2.5.:** Neutron spectrum of the *TRIGA Mark-II* reactor at the *Atominstut*, taken from [137].

of the Ni samples can be determined by measuring the intensity of its 811 keV gamma line using quantitative gamma spectroscopy. With the half life  $t_{1/2}$  of the isotope, which is 71 days, and the time  $\Delta t$  that has passed since irradiation, the  $^{58}\text{Co}$  content directly after irradiation can be calculated using

$$N = A \frac{t_{1/2}}{\ln(2)} e^{\ln(2)\Delta t/t_{1/2}}, \quad (2.2)$$

where  $N$  is the number of  $^{58}\text{Co}$  atoms, and  $A$  is the activity of the sample belonging to the 811 keV peak. For fast neutron fluences  $\Phi_f t$  small enough to transmute only a small fraction of the  $^{58}\text{Ni}$  atoms a linear relation between  $N$  and  $\Phi_f t$  can be assumed:

$$N = h \frac{m_{\text{mon}}}{M_a} \sigma_{\text{eff}} \Phi_f t \quad (2.3)$$

In (2.3)  $h = 0.681$  is the abundance of  $^{58}\text{Ni}$  in naturally occurring nickel,  $m_{\text{mon}}$  is the monitor sample mass,  $M_a = 58.7\text{u}$  is the atomic mass of Ni, and  $\sigma_{\text{eff}}$  is the effective cross section of the transmutation reaction. The latter can be calculated if both the energy dependence of the transmutation cross section  $\sigma_{\text{trans}}(E)$  and the fast neutron spectrum  $\Phi_f(E)$  are known:

$$\sigma_{\text{eff}} = \frac{\int \sigma_{\text{trans}}(E) \Phi_f(E) dE}{\int \Phi_f(E) dE} \quad (2.4)$$

For the fast neutron spectrum of the *TRIGA Mark-II* reactor in Vienna the value of  $\sigma_{\text{eff}}$  is assumed to be 106 mb, based on the data presented in [137]. Using this value together with (2.2) and (2.3), the fast neutron fluence attained in each irradiation step was evaluated. Since the mass and the activity of the monitor samples can be measured very accurately, the main source of error is the uncertainty in  $\sigma_{\text{eff}}$ . Based on reasonable assumptions for the uncertainties introduced by the measurement methods and by the computations from which the effective cross section was obtained, the overall accuracy of the fast neutron fluences in this work is estimated to be  $\pm 10\%$ . Figure 2.6 shows a typical gamma spectroscopy result whose counts in the 811 keV peak are used to calculate the  $^{58}\text{Co}$  activity  $A$  based on detector efficiency and geometry.

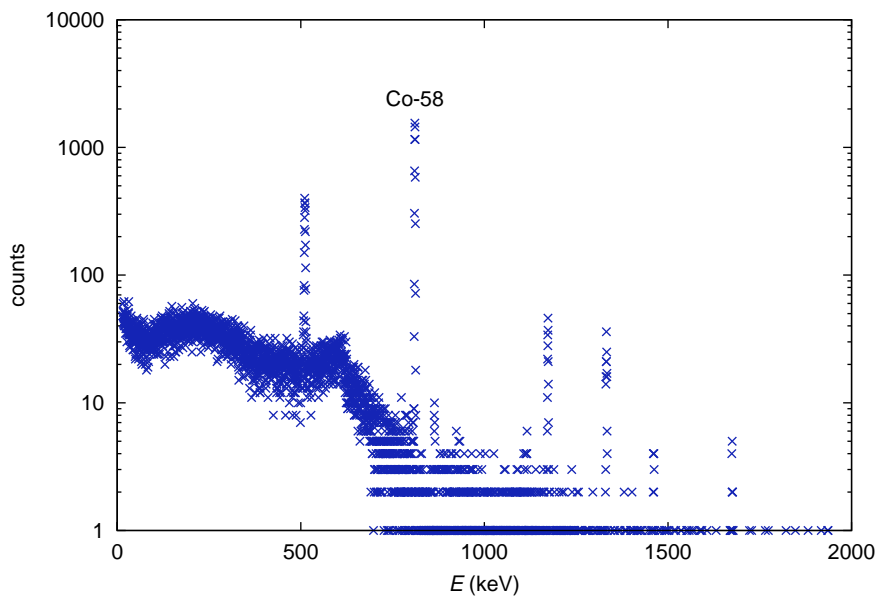


**Figure 2.6.:** Gamma spectroscopy of a nickel sample used for fluence monitoring. The distinctive peak at 811 keV is used to compute the fast neutron fluence the sample was exposed to.

The fast neutron fluences of all irradiation steps are listed in Table 2.5. They are the result of different target fluences, based on which the irradiation time  $t$  of each step was chosen, as well as the above-mentioned variation in  $\Phi_f$ . In Table 2.6 all samples which were part of the irradiation program are listed, and the symbol “ $\times$ ” is used to indicate which samples were included in which irradiation steps.

In the case of the Ni monitor samples the nuclear transmutation reaction caused by neutron irradiation is quite useful. In the wire samples, however, such reactions are unwelcome, since they produce radioactive isotopes without any benefit. They are usually caused by

Step	$\Phi_f t$ ( $10^{22} \text{ m}^{-2}$ )	Date	Step	$\Phi_f t$ ( $10^{22} \text{ m}^{-2}$ )	Date
1	0.07	July 12, 2010	8	0.20	July 28, 2011
2	0.07	July 20, 2010	9	0.09	Oct. 18, 2011
3	0.12	Aug. 18, 2010	10	0.20	Jan. 17, 2012
4	0.11	Sept. 23, 2010	11	0.26	Apr. 02, 2012
5	0.11	Nov. 17, 2010	12	0.80	Apr. 18, 2012
6	0.17	Apr. 19, 2011	13	0.37	Apr. 26, 2012
7	0.10	June 07, 2011			

**Table 2.5.:** Fast neutron fluences and completion dates of all irradiation steps.

thermal and epithermal neutrons, since  $\sigma_{\text{trans}}(E)$  of many nuclei exhibits a  $1/\sqrt{E}$  behavior in the thermal energy range, and has resonance peaks at epithermal energies, while being small at energies in the fast neutron regime. The reactions most relevant for the investigated wire types are listed in Table 2.7 along with the approximate cross sections for reasonable flux density distributions  $\Phi_{\text{th}}(E)$  and  $\Phi_{\text{ep}}(E)$ , and the half lives of the products [38].

Shortly after irradiation the decay of the copper isotopes  $^{64}\text{Cu}$  and  $^{66}\text{Cu}$  is dominant in all sample types. After a proper decay time the radiation stemming from  $^{182}\text{Ta}$  dominates in the case of the Ta alloyed wires, whereas  $^{113}\text{Sn}$  is the most intense source of radiation in Ti alloyed and binary samples. The latter two isotopes both have a half life of 115 days, but due to the large  $\sigma_{\text{trans}}$  of  $^{181}\text{Ta}$  and its natural abundance of almost 100%, samples containing Ta are more radioactive by two orders of magnitude after a decay time of several weeks. The transmutation reaction  $^{46}\text{Ti}(n,p)^{46}\text{Sc}$ , which is triggered by fast neutrons and produces an isotope with a half life of 84 days, is only relevant in transport samples due to the large amount of Ti in the Ti-6Al-4V barrel. Intense radioactivity shortly after irradiation of the barrel material is caused by the isotopes  $^{51}\text{Ti}$ ,  $^{28}\text{Al}$ , and  $^{52}\text{V}$ .

While the neutron activation tables in [38] are very comprehensive, the data presented in [7] are more practically orientated as they allow a quick estimation of the activation of a sample based on the masses of the elements it is comprised of (assuming natural isotopic composition). An impressive collection of energy dependent neutron reaction cross sections, decay schemes, and other useful data can be found on the website of the *National Nuclear Data Center* [88]. Using data from [7] as well as the dose rate constants given in [130], the radioactivity of magnetization and transport samples as a function of time was

	1	2	3	4	5	6	7	8	9	10	11	12	13
RRP-1	x		x	x	x	x		x		x	x		
RRP-2	x	x	x	x	x	x		x		x			x
RRP-3					x	x			x				
RRP-4					x	x			x				
RRP-5					x	x			x				
PIT-1	x		x	x	x	x		x		x	x		
PIT-2	x	x	x	x	x	x		x		x			x
TiR-1						x		x		x	x		
TiR-2						x	x	x		x			x
TiR-3						x							
TiR-7												x	
TiR-8													x
BIN-1						x		x		x	x		
BIN-2						x	x	x		x			x
BIN-3						x							
P07-1												x	
P07-2													x
P07-4											x		
TiR-T1												x	
TiR-T2													x
P07-T2												x	

**Table 2.6.:** Sample irradiation history. An “x” means that the respective sample was included in the corresponding irradiation step.

Reaction	$\sigma_{\text{trans}}$ (b)	$t_{1/2}$
$^{63}\text{Cu}(n,\gamma)^{64}\text{Cu}$	4.5	12.7 h
$^{65}\text{Cu}(n,\gamma)^{66}\text{Cu}$	2.2	5 min
$^{112}\text{Sn}(n,\gamma)^{113}\text{Sn}$	0.8	115 d
$^{181}\text{Ta}(n,\gamma)^{182}\text{Ta}$	21	115 d

**Table 2.7.:** Most relevant nuclear transmutation reactions occurring during neutron irradiation of the investigated wires.

computed before irradiation to predict reasonable decay times.<sup>1</sup> The result obtained for a 4 mm long P07 type magnetization sample after irradiation to  $\Phi_f t = 10^{22} \text{ m}^{-2}$  is shown in Figure 2.7. For this kind of sample a decay time of one week is a prudent choice, whereas six months or more are advisable for Ta alloyed transport samples in order to reduce the much higher  $^{182}\text{Ta}$  activity by a significant amount.

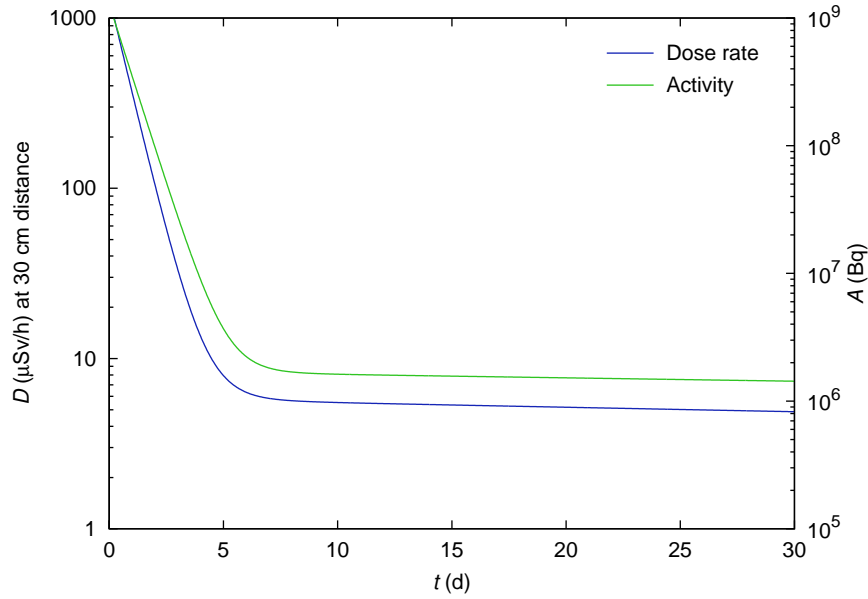


**Figure 2.7.:** Activity and dose rate at a distance of 30 cm computed for a typical Ta alloyed magnetization sample after irradiation to  $\Phi_f t = 10^{22} \text{ m}^{-2}$ , including the contributions of 20 radionuclides.

<sup>1</sup>The dose rate constants of some of the activation products are not listed in [130]. In this case the value corresponding to  $^{60}\text{Co}$  was used.

## 3. Measurements

All types of measurements performed in the course of this work are described in detail in this chapter. The magnetization measurements on the short wire samples described in Subsection 2.2.1, which were carried out in the unirradiated state and after each irradiation step (cf. Section 2.3), are discussed in Section 3.1. A description of additional measurements in a vibrating sample magnetometer, performed primarily to check the validity of the SQUID results, is given in Section 3.2. Transport measurements on unirradiated and irradiated samples as well as resistivity measurements carried out to determine the upper critical field are described in Section 3.3. The evaluation procedures used to obtain the quantities of interest from the measurement results are discussed in Section 3.4.

### 3.1. SQUID magnetometry

Magnetization measurements allow the assessment of the critical current density  $J_c$  of a wire sample as a function of temperature and applied field, provided that a sufficiently accurate model exists, which relates the measured quantity (i.e. the magnetic moment) to the critical current density. The model used in this work is based on the Bean critical state model as well as on some geometric assumptions, and is described in detail in Subsection 3.4.1. Magnetometry offers the following advantages over transport measurements:

- When working with irradiated samples, the huge difference in sample length leads to a reduction of radioactivity by roughly two orders of magnitude, assuming the same fluence and decay time.
- Magnetization measurements are less time consuming, which goes along with a lower consumption of liquid helium.
- Measurements can be performed in temperature and field ranges which are normally not accessible by means of transport measurements due to extremely high critical

currents (several 1000 A) and the problems associated with transport measurements in a gas cooled mode.

Clearly, the first point is highly relevant to safety, and if it were not for this severe reduction in radioactivity, detailed measurements involving many irradiation steps would have been irreconcilable with radiation protection regulations. Moreover, if it were not for the second and third point, the amount of experimental results presented in this work could not have been obtained within the given time frame.

All magnetization measurements whose results were used to obtain the critical current density and consequently the pinning force scaling behavior of each sample type were performed with a *Quantum Design MPMS XL*. This system employs a second order gradiometer pick-up coil assembly and allows measurements at applied fields of up to 7 T in a temperature range from 1.9 to 400 K. The wire samples were mounted perpendicular to the applied field to emulate their operating conditions as part of a magnet. The system was then programmed to automatically measure two-quadrant magnetization loops (from zero applied field to maximum and back to zero) at different temperatures in order to obtain the irreversible magnetic moment  $m_{\text{irr}}$  as a function of temperature and applied field. It can be extracted from the measured quantity, which is the total magnetic moment  $m$  of the sample, using

$$m_{\text{irr}}(B_a) = \frac{1}{2} \left( m_{\text{dec}}(B_a) - m_{\text{inc}}(B_a) \right). \quad (3.1)$$

where  $m_{\text{dec}}(B_a)$  and  $m_{\text{inc}}(B_a)$  are the magnetic moments measured in decreasing and in increasing applied field, respectively. Expression (3.1) holds as long as the background is non-hysteretic, which was the case for all SQUID magnetization measurements presented in this work. Using (3.1) and the  $J_c$  evaluation model described in Subsection 3.4.1 (in particular expression (3.33)),  $J_c(B_a)$  can be obtained from a magnetization loop.

Aside from measuring the magnetic moment of a sample, the *MPMS XL* also has the capability of performing AC susceptibility measurements in a frequency range from 0.1 Hz to 1 kHz, which was used for obtaining the critical temperature. The procedures involved in magnetization measurements with the standard sample transport and the RSO, respectively, are discussed in Subsection 3.1.1 and Subsection 3.1.3, and AC susceptibility measurements are described in Subsection 3.1.4.



### 3.1.1. Standard sample transport

The most basic measurement operation of the *MPMS XL* is to move a sample through the pick-up coil assembly in small steps, measuring the SQUID response voltage as a function of the sample position  $z$ . The magnetic moment  $m$  of the sample can then be evaluated from the voltage versus position curve (raw curve), which is automatically recorded by the system, by employing a fit procedure. For a second order gradiometer with a two-windings center coil at  $z = 0$  and two one-winding coils at  $z = \pm d$  this curve is described by the expression

$$V(z) = \frac{-a^2 m}{2} \left[ \frac{1}{((z+d)^2 + a^2)^{3/2}} - \frac{2}{(z^2 + a^2)^{3/2}} + \frac{1}{((z-d)^2 + a^2)^{3/2}} \right], \quad (3.2)$$

and its shape is shown in Figure 3.1 for the actual dimensions  $a = 1.01$  cm and  $d = 1.52$  cm used in this system. The unit responsible for moving the sample in this manner is referred to as standard sample transport to distinguish it from the RSO, which is described in Subsection 3.1.3. The so-called scan length is the distance the sample travels through the pick-up coil assembly during each measurement. It was set to 4 cm, which should provide a good field homogeneity (0.01% non-uniformity according to *Quantum Design*) while recording a large enough portion of the raw curve to keep fit errors small. Each  $m(B_a)$  data point at constant temperature was obtained by averaging over three consecutive measurements (also known as scans in this context). In this way dubious data points can often be identified based on the standard deviation of the three scans. Generally, the described measurement procedure can be expected to yield good results as long as:

- The sample is small compared to the pick-up coil assembly (2 cm coil diameter, 3 cm distance between top and bottom coil) and can thus be regarded as a magnetic dipole.
- The magnetic moment of the sample is constant during the measurement.
- The signal produced by the sample is much larger than the background signal stemming from the sample holder and any sources of noise in the system.

The first condition is purely geometric and can be met easily by cutting the wire samples to a reasonable length, as described in Subsection 2.2.1. While the third condition is usually met for high- $J_c$  wires as long as temperature and applied field are not too close to the transition to the normal state, the second one proved to be somewhat problematic, as elucidated below.

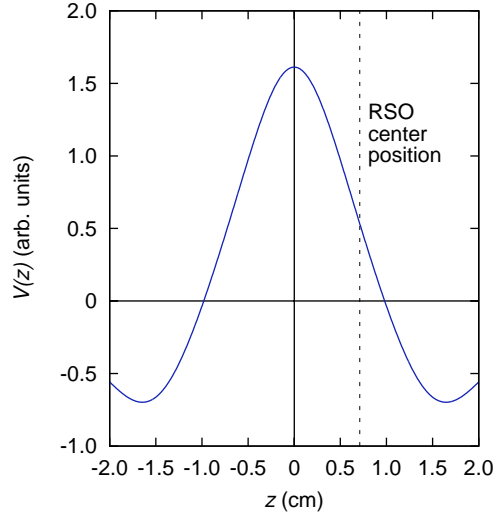


**Figure 3.1.:** SQUID magnetometer response as a function of the sample position.

During the measurement the sample is mounted on a sample holder which is connected to the transport unit via the sample rod, which consists of a stainless steel tube with a brass ending. While the sample rod is provided by *Quantum Design*, the fabrication of the sample holder is subject to the preference of the experimenter. Usually the following three design principles are considered:

- The length of the sample holder must be large compared to the distance between the top and bottom pick-up coil.
- Its cross section should be as homogeneous as possible over the entire length.
- A material with low magnetic susceptibility and non-hysteretic magnetic behavior should be used.

If the first two principles were perfectly implemented (infinitely long, absolutely homogeneous sample holder), the third would be rendered unnecessary, since the sample holder would be “invisible” to the system. Since this is not realistic, the material criterion is important. Aluminum foil with very low iron content<sup>1</sup> is frequently used to construct sample holders with a u-shaped cross section, and transparent plastic straws (dyes tend to have unfavorable magnetic properties) are also commonly used.

The sample holder used for the standard sample transport SQUID measurements presented in this work was made from a silica glass tube. The main advantage of this material is its

<sup>1</sup>Iron is a common impurity in aluminum, and due to its ferromagnetic properties its presence is particularly undesired.

small magnetic susceptibility ( $\chi \approx -9 \cdot 10^{-6}$  at low temperatures [35]), while the obvious disadvantage is its brittleness. The tube had an outer diameter of 4 mm and an inner diameter of 2 mm, and was cut to a length of 195 mm with a diamond saw. A recess for mounting the sample was milled into the material, and a copper wire loop for attaching the sample holder to the sample rod was glued into one end of the tube with epoxy resin. The connection between the sample holder and the sample rod is not rigid, allowing the sample holder to align with gravity, thus preventing a misalignment between the sample and the applied field. The construction is depicted in Figure 3.2.

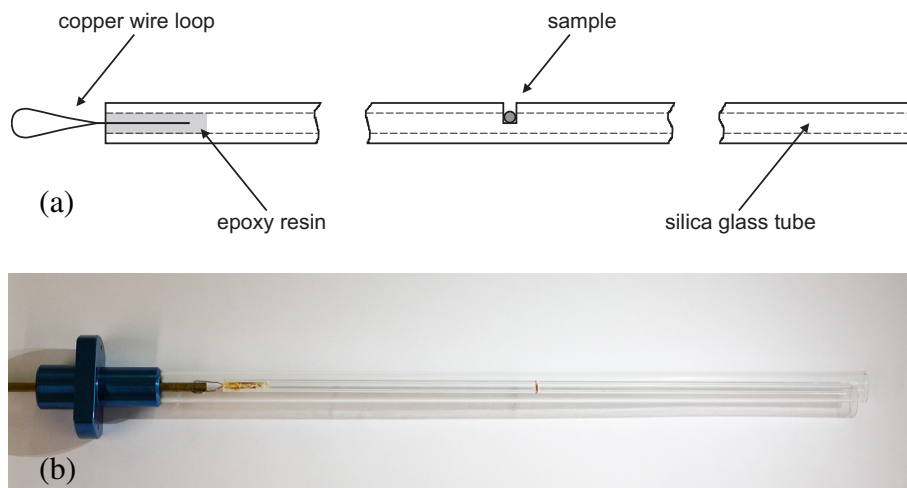


**Figure 3.2.:** Sample holder used in measurements with the standard sample transport. (a) Design drawing. (b) Photograph of the sample holder attached to the *MPMS XL* sample rod, protected by a glass tube.

#### 3.1.2. Problems with the standard sample transport

As stated above, the magnetic moment must remain constant during the measurement in order to obtain reliable results. If, however, it does for some reason decay with time, there will be two consequences. Firstly, each of the three pick-up coils will “see” a different magnetic moment, which results in an asymmetric response curve. And secondly, when averaging over several (three in this case) measurements, the amplitude of this asymmetric raw curve will decrease from one measurement to the next. The result of a computer simulation of these two effects is shown in Figure 3.3 for a magnetic moment decreasing linearly with time. The output value of the *MPMS XL* software obtained by fitting (3.2) to the average of the raw curves will be lower than the initial magnetic moment. Such a

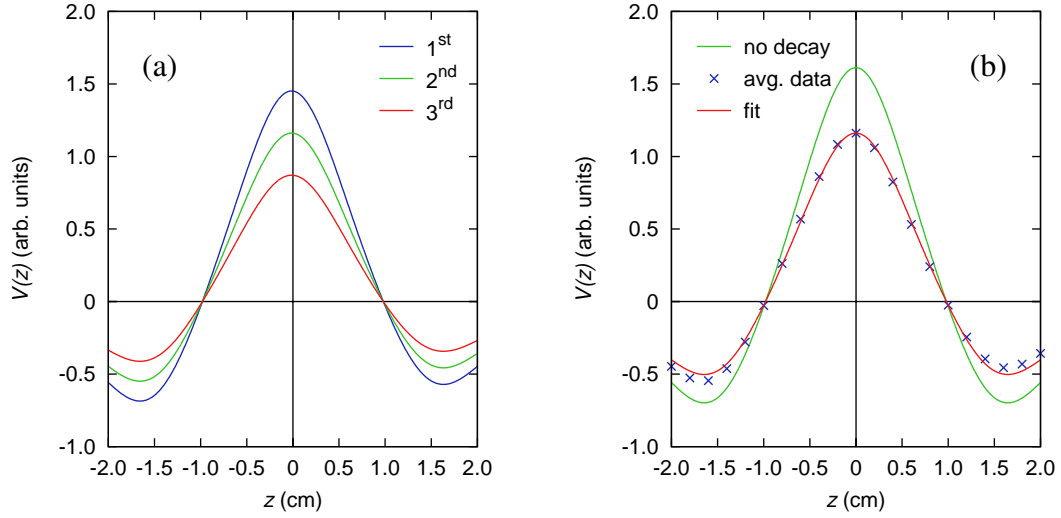


**Figure 3.3.:** A decreasing magnetic moment causes the raw curves to become smaller in magnitude as well as asymmetric. **(a)** Individual curves of three scans. **(b)** Expected signal without decay, average of the three curves, and fit function.

behavior was indeed observed. It was first discovered when SQUID magnetometry was performed with the RSO (cf. Subsection 3.1.3) instead of the standard sample transport. Measuring the same sample with the RSO and with the standard sample transport at the same temperature yielded different magnetization curves. The observed deviation was not simply the effect of a mismatched calibration factor, but rather a function of applied field and temperature. Figure 3.4(a) illustrates the effect using data obtained from sample PIT-3: The magnetization loops measured with the standard sample transport are smaller in magnitude than those measured with the RSO, and the difference between the two types of measurements increases with increasing applied field, leading to an apparently lower value of the upper critical field in standard sample transport measurements. The effect exhibits a pronounced temperature dependence as shown in Figure 3.4(b).

## Relaxation

The first hypothesis drawn from these facts was that the relaxation of the magnetization profile in the sample might be responsible for this behavior. Strictly speaking, the Bean profile created by magnetizing a type-II superconductor is a non-equilibrium state which is only stable at  $T = 0$ . At finite temperatures it strives to equilibrate, leading to a flattening of the magnetization gradients in the sample and hence to a reduction of the magnetic moment. Experimentally a power law is often found to describe the time dependence of

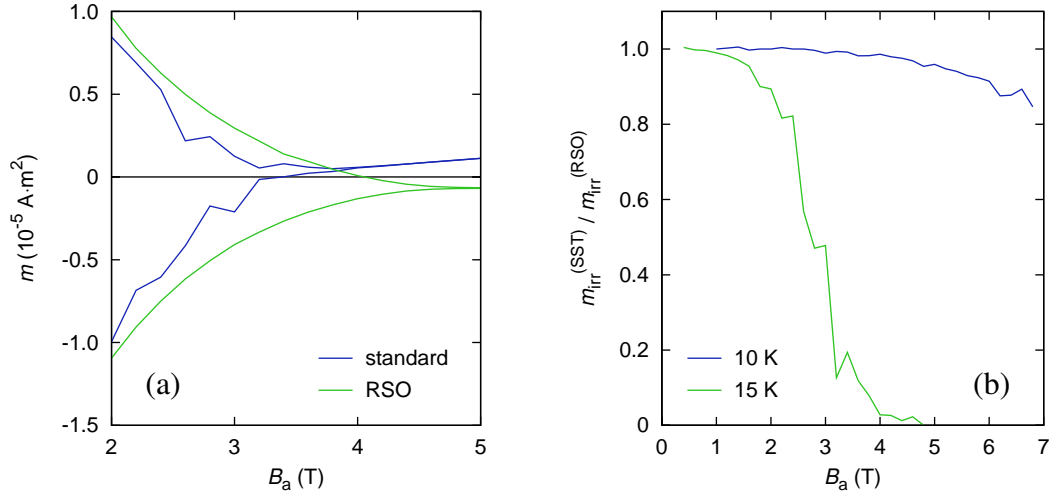


**Figure 3.4.:** Comparison of magnetization measurements with the standard sample transport and with the RSO on sample PIT-3. **(a)** Magnetization loops at 15 K. **(b)** Ratio of the irreversible magnetic moments at two temperatures.

the irreversible magnetic moment:

$$m_{\text{irr}}(t) = m_{\text{irr}}(0) t^{-C} \quad (3.3)$$

In (3.3)  $m_{\text{irr}}(0)$  is the irreversible magnetic moment at an arbitrary origin  $t = 0$ , and  $C$  is a constant for the given sample and parameters. With the device settings used in the measurements presented in this work, the measurement of one data point (three scans) with the standard sample transport takes approximately 150 s, whereas it takes only 15 s when the RSO is used. It stands to reason that this difference of one decade in measurement time may result in a difference in the measured magnetic moment due to relaxation.

To test this hypothesis, a relaxation measurement was performed on sample PIT-3 at a temperature of 15 K by applying a field of 3 T and repeatedly measuring the magnetic moment with the RSO over a duration of several hours. Figure 3.5 depicts the results in a log-log plot together with a linear fit whose slope corresponds to the constant  $C$  in (3.3). The relaxation rate obtained from the linear fit is 7% per decade, which is not enough to explain the difference of approximately 50% observed in Figure 3.4(b) at the same field and temperature. Relaxation could therefore be ruled out as the cause of the difference between standard sample transport and RSO measurements.

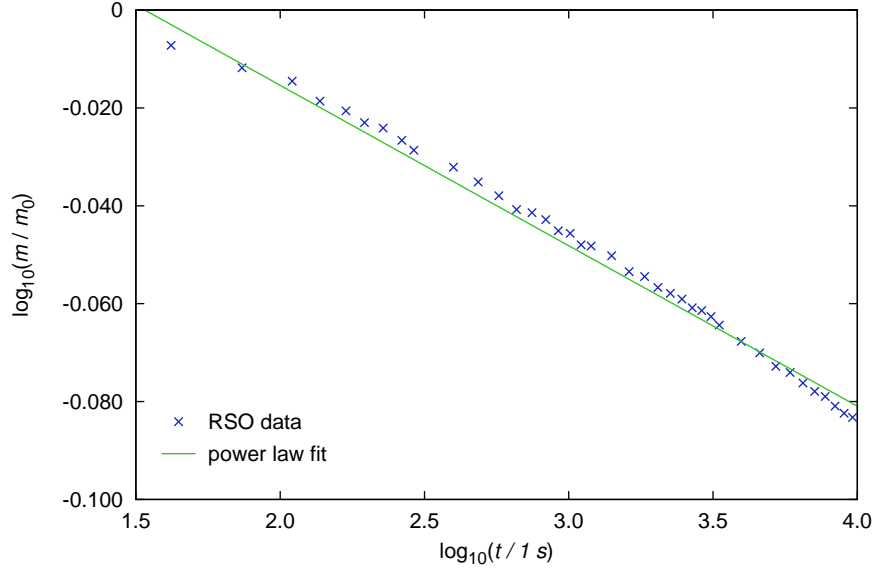


**Figure 3.5.:** Relaxation of the magnetic moment of sample PIT-3 at 15 K after magnetizing it in a field of 3 T, measured with the RSO (cf. Subsection 3.1.3).

### Profile reversal

Another possible explanation for the observed behavior is the non-uniformity of the applied field in the SQUID magnetometer. According to the Bean model [9], a small change  $\Delta B$  in the applied field  $B_a$  causes a reversal of the magnetization profile near the surface of the superconductor if  $\Delta B < 0$  when measuring in increasing field, or  $\Delta B > 0$  when measuring in decreasing field. The penetration depth of this reversed profile is approximately given by

$$d = \frac{\Delta B}{\mu_0 J_c}. \quad (3.4)$$

Based on the hollow cylinder approximation used in the  $J_c$  evaluation method described in Subsection 3.4.1, the change of the magnetic moment of a superconducting sub-element due to this profile reversal can be calculated. Assuming that the reversed profile penetrates the sub-element perpendicular to the applied field from either side, the resulting current distribution is the one depicted in Figure 3.6. The irreversible magnetic moment  $\Delta m_{\text{irr}}$  generated by the reversed profile can be calculated analogously to the derivation in Subsection 3.4.1 by integrating over the infinitesimal magnetic moments of current loops with

the cross section  $dx dy$ , described by

$$dm = 2J_c L x dx dy. \quad (3.5)$$

Using the integral bounds corresponding to the above-mentioned field penetration (parallel to the  $x$ -axis, with  $\rho_o$  denoting the outer sub-element radius), the irreversible moment caused by the reversed profile in one sub-element takes the form<sup>2</sup>

$$\begin{aligned} \Delta m_{\text{irr}} &= 2 \int_{y=0}^{\rho_o} \int_{x=\sqrt{\rho_o^2-y^2}-d}^{\sqrt{\rho_o^2-y^2}} dm = 4J_c L \int_0^{\rho_o} \int_{\sqrt{\rho_o^2-y^2}-d}^{\sqrt{\rho_o^2-y^2}} x dx dy \\ &= 2J_c L \int_0^{\rho_o} \left[ \rho_o^2 - y^2 - \left( \sqrt{\rho_o^2 - y^2} - d \right)^2 \right] dy \\ &= 2J_c L \int_0^{\rho_o} \left[ 2d \sqrt{\rho_o^2 - y^2} - d^2 \right] dy \\ &= 2J_c L \left[ d y \sqrt{\rho_o^2 - y^2} + d \rho_o^2 \arctan \left( \frac{y}{\sqrt{\rho_o^2 - y^2}} \right) - d^2 y \right]_{y=0}^{\rho_o} \\ &= 2J_c L d \rho_o \left( \frac{\pi}{2} \rho_o - d \right). \end{aligned} \quad (3.6)$$

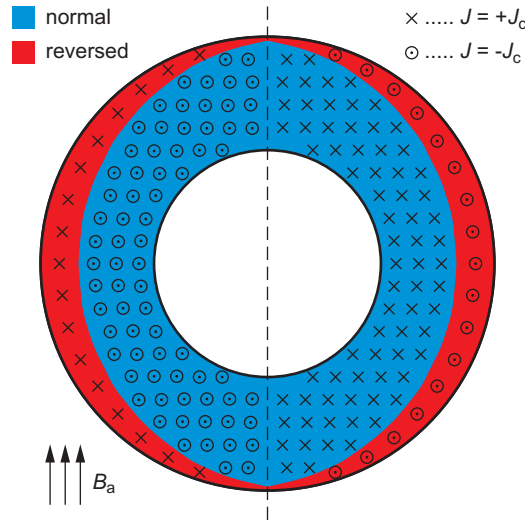


**Figure 3.6.:** Reversal of the magnetization profile in a superconducting sub-element due to a decrease of the applied field.

Since  $\Delta m_{\text{irr}}$  is not only “missing” from the undisturbed irreversible moment  $m_{\text{irr}}^{(0)}$ , but

<sup>2</sup>The following identity was used in (3.6):

$$\int \sqrt{a^2 - x^2} dx = \frac{1}{2} \left( x \sqrt{a^2 - x^2} + a^2 \arctan \left( \frac{x}{\sqrt{a^2 - x^2}} \right) \right)$$

rather points in the opposite direction, the total magnetic moment of the sub-element is given by  $m_{\text{irr}}^{(0)} - 2\Delta m_{\text{irr}}$ . Hence the ratio of the magnetic moment including profile reversal and the undisturbed magnetic moment is

$$r = \frac{m_{\text{irr}}^{(0)} - 2\Delta m_{\text{irr}}}{m_{\text{irr}}^{(0)}}. \quad (3.7)$$

Inserting the expression for the undisturbed moment  $m_{\text{irr}}^{(0)} = 4/3 J_c L (\rho_o^3 - \rho_i^3)$ , which is derived in Subsection 3.4.1, yields

$$r = 1 - \frac{3d \rho_o \left( \frac{\pi}{2} \rho_o - d \right)}{\rho_o^3 - \rho_i^3}. \quad (3.8)$$

At a temperature of 15 K and an applied field of 3 T the critical current density of sample PIT-3 obtained from the RSO data shown in Figure 3.4(a) is approximately  $3.6 \cdot 10^8 \text{ A/m}^2$ . Using this value and the geometry of this sample type (cf. Subsection 2.1.1) expression (3.8) can be evaluated as a function of  $d$ , as shown in Figure 3.7. According to this plot

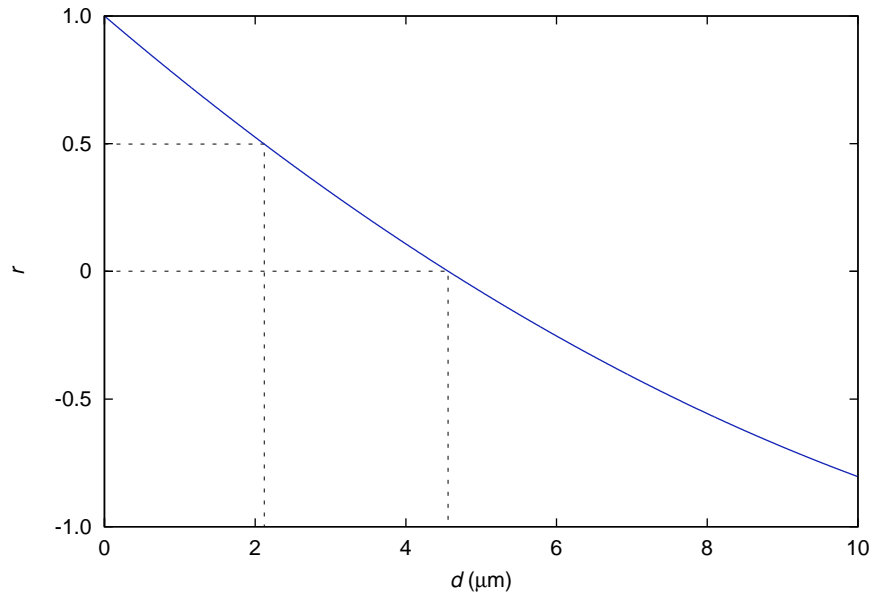


**Figure 3.7.:** Relative change of the irreversible magnetic moment due to profile reversal as a function of the Bean penetration depth  $d$ , calculated for sample PIT-3 assuming  $J_c = 3.6 \cdot 10^8 \text{ A/m}^2$ . A reduction by 50% requires a penetration depth of roughly  $2 \mu\text{m}$ , and for  $d > 4.6 \mu\text{m}$  the measured magnetic moment changes sign.

$d$  must assume a value of approximately  $2 \mu\text{m}$  to produce the 50% difference between the standard sample transport data and the RSO data seen in Figure 3.4(b) at 15 K and 3 T.



Using (3.4) the corresponding field change can be calculated from  $d$ , yielding the result  $\Delta B = 0.9 \text{ mT}$ , which is 0.03% of the applied field. This is in the same order of magnitude as the 0.01% non-uniformity claimed by *Quantum Design*, but it left some doubt as to whether profile reversal is the correct explanation. Therefore, yet another hypothesis was formulated, namely the decay of the irreversible magnetic moment due to the shaking field effect.

#### Shaking field

The term “shaking field” refers to an alternating magnetic field which is perpendicular to and much smaller than the static magnetic field applied to a superconducting sample. As derived by Brandt and Mikitik in [18] such a shaking field can cause the irreversible currents and thus the magnetic moment of a sample to relax rapidly. Since the two above-mentioned explanations for the decay of the magnetic moment were questionable, the possibility of a shaking field effect was investigated, as this may arise from a swaying motion of the sample holder inside the superconducting magnet of the SQUID magnetometer.

The time dependence of the magnetic moment (per unit length) of a thin strip is calculated for longitudinal (AC field parallel to the long side) as well as transverse (AC field perpendicular to the long side) shaking in [18]. Although both situations may arise from sample holder motion, only transverse shaking will be considered, since it has a much more pronounced effect than longitudinal shaking. Obviously the geometry of the sub-elements in the samples examined in this work is more complex than thin strips, but the simple geometry assumed in the article by Brandt and Mikitik should suffice for a rough estimation of the magnitude of the effect. Substituting the width of the strip of  $2w$  with the sub-element diameter  $2\rho_0$ , their expression for the time dependence of the magnetic moment due to transverse shaking takes the form

$$m(t) = m(0) e^{-t/\tau} \quad (3.9)$$

with

$$\tau = 0.25 \frac{\pi \rho_0 \mu_0 J_c}{\omega B_{AC}}, \quad (3.10)$$

where  $m(0)$  is the magnetic moment of the strip directly before the shaking field with the amplitude  $B_{AC}$  is “switched on”, and  $\omega$  is the angular frequency of that field. By finding a

reasonable value for  $\omega$ , the value of  $B_{AC}$  required to produce the effect seen in Figure 3.4 can be estimated.

The moment of inertia of a homogeneous, thin rod of mass  $m$  and length  $L$  rotating about an axis perpendicular to its symmetry axis and passing through one of its ends is

$$\Theta = \frac{mL^2}{3}, \quad (3.11)$$

and the angular frequency of a generic pendulum is given by

$$\omega = \sqrt{\frac{mgd}{\Theta}}, \quad (3.12)$$

where  $g$  is the gravitational acceleration of the Earth, and  $d$  is the distance between the suspension point and the center of mass. Using  $d = L/2$ , (3.11) and (3.12) can be combined to obtain the angular frequency of the swaying sample holder:

$$\omega = \sqrt{\frac{3g}{2L}} \quad (3.13)$$

Inserting the sample holder length of 195 mm yields  $\omega = 8.7 \text{ s}^{-1}$ . Using this value and a  $J_c$  of  $3.6 \cdot 10^8 \text{ A/m}^2$ , as found from Figure 3.4 at 15 K and 3 T, the shaking field required for the observed 50% reduction within the standard sample transport measurement time of 150 s can be calculated from (3.10):

$$\tau = -\frac{150 \text{ s}}{\ln(0.5)} = 216 \text{ s} \quad \Rightarrow \quad B_{AC} = 4.3 \mu\text{T} \quad (3.14)$$

Denoting the maximum angle between the sample rod axis and the center axis of the superconducting magnet inside the *MPMS XL* by  $\varphi$ , the shaking field amplitude is given by

$$B_{AC} = B_a \sin(\varphi). \quad (3.15)$$

Using (3.15) and the value of  $B_{AC}$  found in (3.14), the angle  $\varphi$  can be calculated. The result is  $1.4 \mu\text{rad}$  ( $0.29''$ ), corresponding to a tiny lateral deflection of the sample holder. Even though the assumption of a swaying motion with constant amplitude and direction (transverse shaking) throughout the entire duration of the measurement is certainly exaggerated, and the averaging over three scans has been neglected, the result of the estimation

shows that the shaking field effect can easily cause the observed decay of the irreversible magnetic moment.

A control experiment was performed to verify the above explanation. In this experiment the sample holder was equipped with a damper designed to attenuate its swaying motion. This damper was comprised of two elements, one at the top and one at the bottom of the sample holder, consisting of several flat springs cut from aluminum foil, as shown in Figure 3.8(a). The flat springs gently press against the interior surface of the sample chamber, thus stabilizing the lateral position of the sample holder. The result of a magnetization measurement on sample PIT-3 at 15 K with the damper installed on the sample holder is shown in Figure 3.8(b). Measurements performed with the undamped sample holder and with the RSO are also shown for comparison. Clearly the use of the damper increases the quality of the measurement and shifts the  $m_{\text{irr}}$  curve obtained with the standard sample transport towards the curve measured with the RSO. This fact supports the shaking field explanation, as further elucidated in the following sub-section.

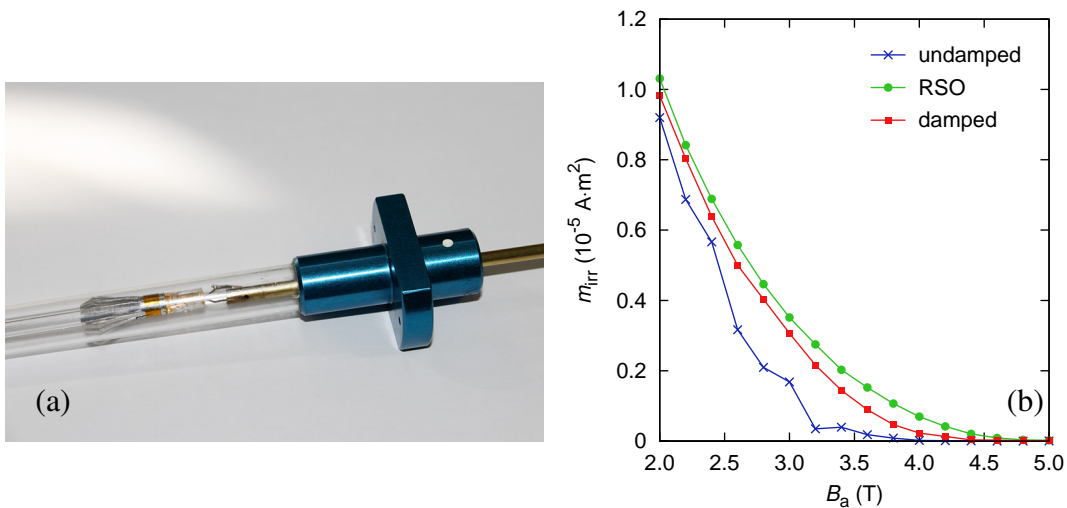


**Figure 3.8.:** Standard sample holder with damper. **(a)** Photograph of the upper section inside a protective glass tube. **(b)** Comparison of magnetization measurements performed with and without damper, and with the RSO.

Given the calculations and measurement results presented above, a decay of the irreversible magnetic moment due to the shaking field effect appears to be the most plausible explanation for the problems encountered with the standard sample transport. It must be pointed out, though, that profile reversal can also lead to significant measurement errors in the case of wires containing very thin sub-elements (a few micrometers), since much smaller values

of  $\Delta B$  are then sufficient to cause a non-negligible field penetration. Relaxation may also produce a notable contribution at field and temperature values where the critical current density is low.

### 3.1.3. RSO

The RSO is an accessory of the *MPMS XL*, intended to increase the sensitivity of the system. RSO is an acronym for “Reciprocating Sample Option” and essentially means that the sample is moved periodically inside the pick-up coil assembly, thus converting the system into a vibrating sample magnetometer with a SQUID sensor. The RSO consists of an airlock, which is a brass tube sealed on one end, containing a sample rod to which a sample holder can be attached. Contrary to the standard sample transport a rigid connection is made, usually by gluing the sample holder to the sample rod with vacuum grease. After mounting the sample holder and the sample itself, the RSO is attached to the top of the *MPMS XL* cryostat. A vacuum is then established inside the airlock, and the sample holder is lowered into the sample chamber inside the cryostat by means of a magnetic coupling between the sample rod and a ring on the outside of the airlock.

A transparent straw with a diameter of roughly 7 mm is recommended by *Quantum Design* for use as RSO sample holder. This recommendation was followed, but the straw was modified by inserting a small silica glass tube oriented transverse to its axis into the center of the straw. It was fixed with *ICEoxford Low Temperature Varnish* and allowed short wire samples to be inserted easily and in a reproducible manner. Figure 3.9 shows photographs of the RSO sample holder and the SQUID magnetometer with the RSO installed.

During measurements with the RSO the sample oscillates around its center position, which is the maximum slope position between the center pick-up coil and the upper pick-up coil (cf. Figure 3.1). Amplitude and frequency of this oscillation as well as the number of cycles within one measurement can be adjusted individually. The settings used in the RSO measurements presented in this work are specified in Table 3.1. The SQUID response during an RSO measurement is in good approximation linear, especially when a small amplitude is used. The magnetic moment is obtained by the *MPMS XL* software by computing a linear fit through the data points collected in all cycles (20 in this case).

In Subsection 3.1.2 the difference between measurements carried out with the standard sample transport and with the RSO were attributed to the shaking field effect. When using

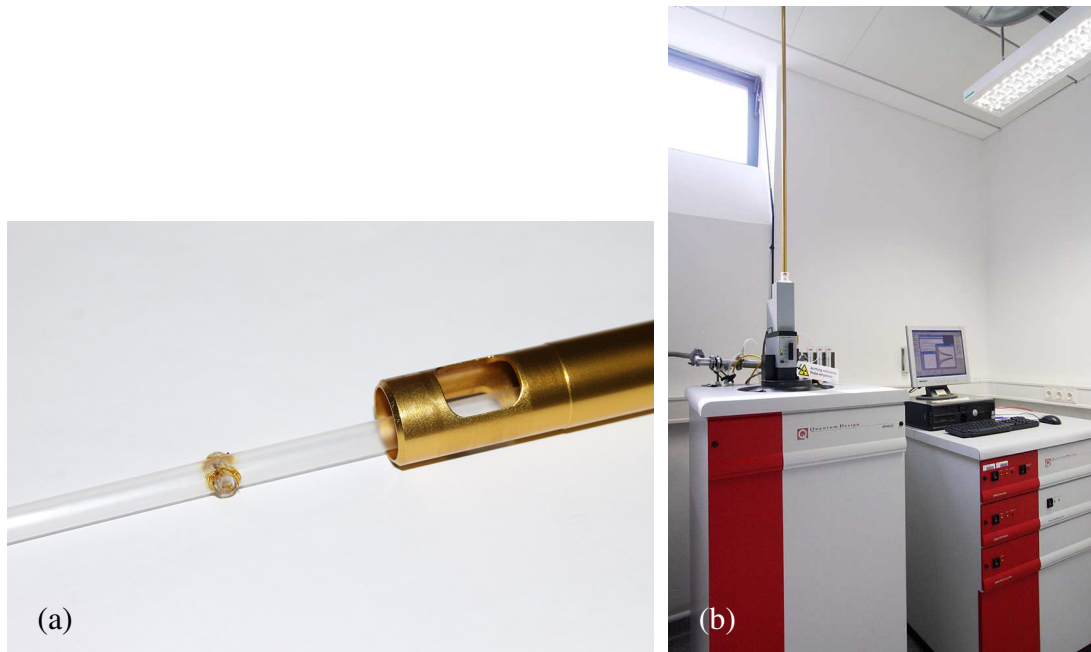


**Figure 3.9.:** Reciprocating Sample Option (RSO) of the *MPMS XL*. (a) RSO sample holder made from a transparent straw and a silica glass tube. (b) SQUID magnetometer with the RSO installed.

Parameter	Setting
Amplitude	2 mm
Frequency	4 Hz
Number of cycles	20

**Table 3.1.:** Settings used for RSO measurements.

the RSO, the rigid (glued with vacuum grease) connection between the sample rod and the sample holder prevents the swaying motion which is the cause of the shaking field. Hence RSO measurements are much less susceptible to the shaking field effect, and are thus more reliable than measurements performed with the standard sample transport. After this had been discovered, all further magnetization measurements were performed with the RSO. Since earlier measurements could not be repeated due to the sequential irradiation of the samples (cf. Section 2.3), a correction function for standard sample transport measurements was devised, as explained in Subsection 3.4.3.

As an example of the magnetization data obtained from RSO measurements, the full set of measurement results (12 temperature values ranging from 4.2 K to 15 K, field steps of 0.2 T up to a maximum field of 7 T) obtained from sample TiR-7 before irradiation is shown in Figure 3.10. The irregularities in the 4.2 K curve were caused by flux jumps, which often occur in magnetization measurements at low temperatures and low fields. Measurements such as these were performed on each sample in its unirradiated state as well as after each irradiation step. The critical current density as a function of magnetic field was then evaluated for each of the temperatures using (3.1) and the  $J_c$  evaluation model described in Subsection 3.4.1 in order to obtain the  $J_c(T, B)$  characteristics of each wire type as a function of fast neutron fluence. Details regarding this evaluation procedure can be found in Subsection 3.4.5, and the results for unirradiated and irradiated samples are discussed in Subsection 4.1.1 and Subsection 4.2.1, respectively.

To check the validity of the assumption made in the  $J_c$  evaluation model that the individual sub-elements inside magnetization samples exhibit no significant coupling, magnetization loops of individual sub-elements were also measured with the RSO. These sub-elements were extracted from wire samples by means of etching, as mentioned in Subsection 2.2.1. The results of these measurements confirmed the validity of the  $J_c$  evaluation model used in this work, as discussed in Subsection 3.4.5.

#### 3.1.4. AC susceptibility

The so-called “AC Option” of the *Quantum Design MPMS XL* is an accessory which facilitates magnetic susceptibility measurements in an alternating magnetic field within a frequency range from 0.01 Hz to 1 kHz. During the measurement a small coil wound around the sample chamber produces an AC field  $B_{AC}$  with a maximum amplitude of 0.4 mT. The

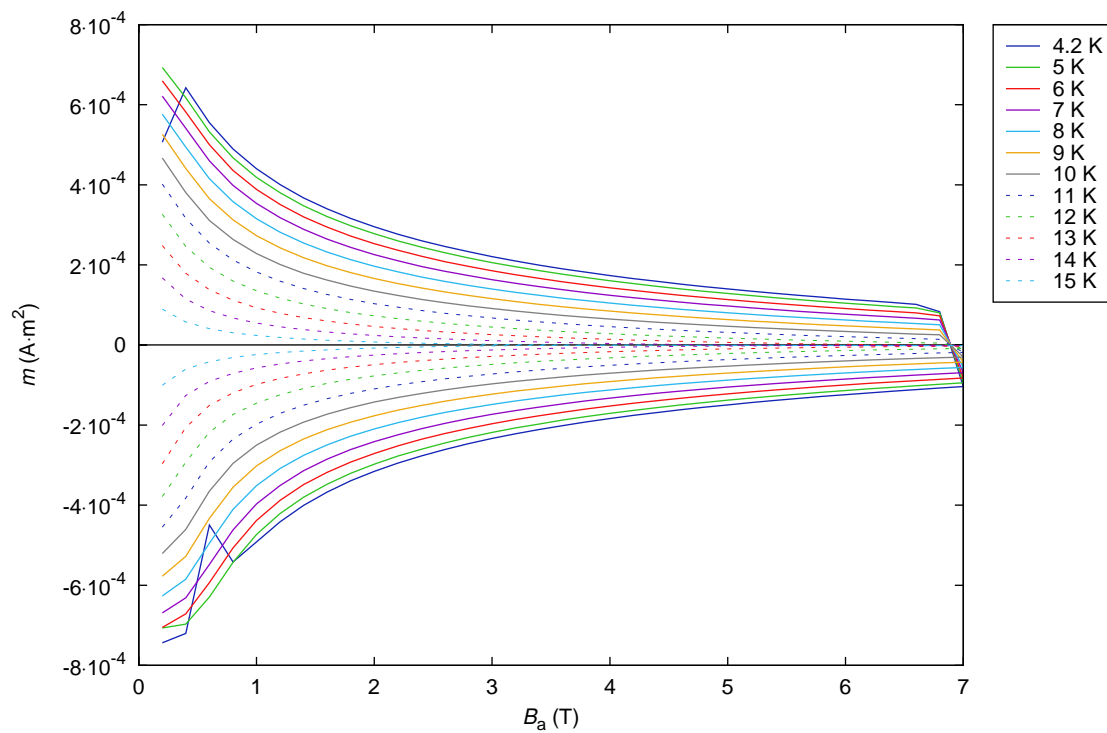


**Figure 3.10.:** Magnetization loops of sample TiR-7 (unirradiated) at 12 different temperatures, measured with the RSO.

system measures the first harmonics of the in-phase component  $m'$  and of the out-of-phase component  $m''$  of the magnetic moment the sample exhibits in response to the applied AC field. The real and imaginary components of the volume susceptibility, the latter of which is a measure for the energy loss in the sample, are given by

$$\chi' = \frac{\mu_0}{V B_{AC}} m' \quad \text{and} \quad \chi'' = \frac{\mu_0}{V B_{AC}} m'', \quad (3.16)$$

where  $V$  is the superconducting sample volume. The measurement process can be broken down into blocks, each of them corresponding to two complete sine wave cycles, and a certain number of blocks comprises one measurement. Each data point in the output file is the result of averaging over a user-defined number of measurements.

As long as no DC field is applied, and the conditions  $B_{AC} < B_{c1}$  as well as  $T < T_c$  are met, the  $m'$  signal obtained from a superconducting sample will correspond to  $\chi' \approx -1$  and  $\chi'' \approx 0$ . At  $T = T_c$  the transition to the normal state occurs, which is reflected in a change of the susceptibility to  $|\chi'| \ll 1$  for most materials. This change can be used to determine  $T_c$  by changing the sample temperature in small steps and performing AC measurements after it has stabilized. From the resulting  $m'(T)$  data the critical temperature as well as its transition width  $\Delta T_c$  can be determined.

For AC measurements it does not matter whether the standard sample transport or the RSO is used, since the problems described in Subsection 3.1.2 can only arise in DC magnetization measurements. AC measurements were performed on all magnetization samples before irradiation and after each irradiation step in order to obtain the dependence of the critical temperature on fast neutron fluence. The settings used in these measurements are listed in Table 3.2.

Parameter	Setting
Amplitude	30 $\mu$ T
Frequency	30 Hz
Blocks per measurement	3
Measurements per data point	3

**Table 3.2.:** Settings used in AC susceptibility measurements.

The typical result of an AC measurement is depicted in Figure 3.11(a) for sample TiR-7



in its unirradiated state. In the vicinity of  $T_c$  a temperature resolution of 0.1 K was used, whereas a lower resolution was used further from the transition to save measuring time. The smaller transition around 9 K stems from the niobium in the diffusion barriers of the sub-elements (cf. Subsection 2.1.1). The simple structure of the transition of the  $\text{Nb}_3\text{Sn}$  around 18 K allows a straightforward evaluation of  $T_c$  and  $\Delta T_c$  by using linear fits. The situation is a bit more complex in Figure 3.11(b), which shows the AC measurement data of sample P07-1 near  $T_c$ . As discussed in Subsection 2.1.1, the grain morphology of wires produced by the powder-in-tube process can be roughly divided into two grain types: small grains on the outside and large grains on the inside of the sub-element. The  $T_c$  of the large grains is somewhat higher (by about 0.7 K) than that of the small grains. When  $T$  approaches  $T_c$  from below, the small grains become normal conducting while the large grains are still superconducting. The result is the two-stage transition found in Figure 3.11(b).

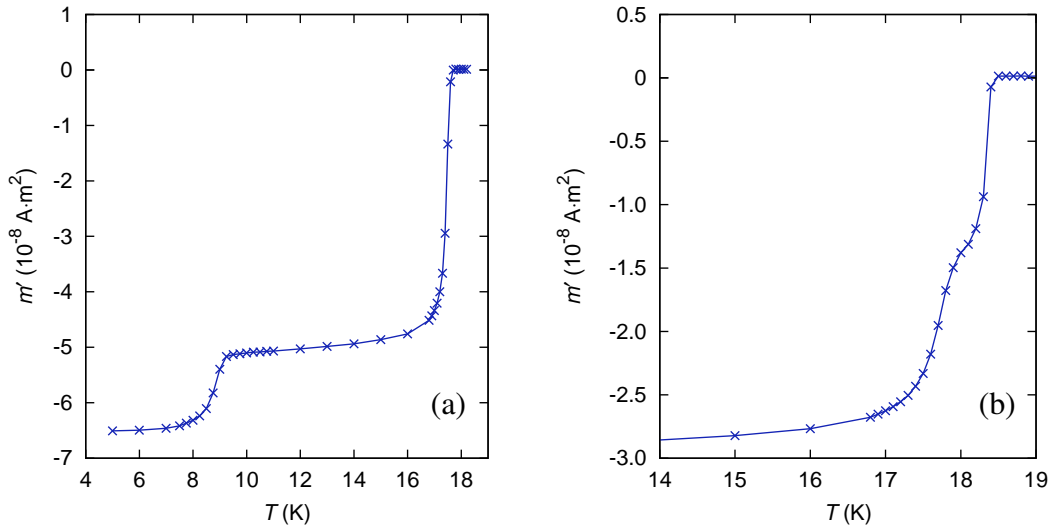


**Figure 3.11.:** AC susceptibility measurements in zero applied field for  $T_c$  evaluation. **(a)** Data of sample TiR-7 including the transition of the Nb diffusion barrier around 9 K. **(b)** Sample P07-1 exhibits a two-stage transition due to the grain morphology of powder-in-tube wires.

With an appropriate evaluation algorithm the critical temperature can be obtained with higher accuracy than the 0.1 K resolution used in the AC measurements. This is important for quantifying the small changes in  $T_c$  that occur due to fast neutron irradiation in the low-fluence regime ( $\Phi_f t \lesssim 10^{22} \text{ m}^{-2}$ , cf. Subsection 1.2.3). The  $T_c$  evaluation algorithm used in this work is discussed in Subsection 3.4.7, and the results obtained from unirradiated and irradiated samples are presented in Subsection 4.1.2 and Subsection 4.2.2, respectively.

## 3.2. VSM measurements

Magnetization measurements with a vibrating sample magnetometer (VSM) were performed primarily to verify the results obtained from SQUID magnetometry (cf. Section 3.1) and to ascertain whether a small misalignment between the sample and the applied field can lead to significant measurement errors. The system used for these measurements was manufactured by *Oxford Instruments* and is capable of measuring two components of the magnetic moment of a sample in applied fields of up to 5 T: one parallel to the field which is applied perpendicular to the axis of vibration, the other perpendicular to the field and to the axis of vibration. By rotating the sample about the axis of vibration the influence of the angle between the sample and the applied field can be investigated. As this was a control experiment, only two samples (PIT-5 and RRP-7, both unirradiated) were measured at only one temperature, which was 5 K. The frequency of the vibration was set to 55 Hz, and the amplitude was 1.5 mm.

### 3.2.1. Comparison with SQUID magnetization data

To obtain a quantitative verification of the SQUID magnetometry results, magnetization loops were measured at a temperature of 5 K on the samples PIT-5 and RRP-7. This was done by aligning the samples perpendicular to the applied field and continually ramping the field from 0 to 5 T and back while measuring the magnetic moment parallel to the field. The main difference from SQUID measurements is the continuous sweep of the applied field, which according to

$$\nabla \times \vec{E} = - \frac{\partial \vec{B}}{\partial t} \quad (3.17)$$

generates an electric field  $\vec{E}$  inside the sample. Due to the power law dependence

$$E \propto J^n \quad (3.18)$$

between the electric field and the current density  $J$ , which is valid in the vicinity of the critical current density, different sweep rates will lead to different measurement results. When comparing VSM measurements at reasonably high sweep rates to SQUID measurements, a difference is bound to arise from the fact that the electric field is much smaller in the

latter. At low temperatures and applied fields well below  $B_{c2}$ , however, this effect is not very pronounced due to the high value of  $n$ .

The irreversible magnetic moment was obtained from the magnetization loops in the same way as described Section 3.1, the only difference being a linear interpolation between adjacent data points necessitated by their uneven distribution. A comparison of the magnetization data obtained from a VSM measurement on sample RRP-7 at a sweep rate of 500 mT/min and from SQUID magnetometry with the RSO (cf. Subsection 3.1.3) on the same sample is shown in Figure 3.12. The difference in the values of  $m_{irr}$  is between 1 and 3%, and increases with increasing field, as can be expected due to the above-mentioned difference in the electric field.

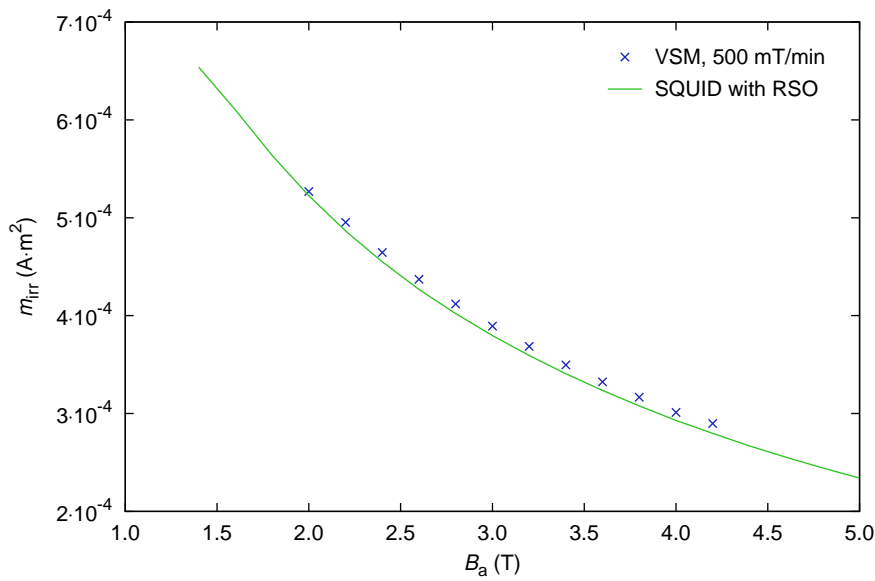


**Figure 3.12.:** Irreversible magnetic moment of sample RRP-7 at 5 K as a function of applied field, measured with the VSM and with SQUID magnetometry.

#### 3.2.2. Angular dependence of the magnetic moment

In the SQUID measurements described in Section 3.1 a slight misalignment of the axis of the wire sample relative to the applied magnetic field can occur due to imperfections of the sample holder or the guideway of the sample rod inside the cryostat. Such a misalignment might lead to faulty results when evaluating the critical current density from magnetization data, since the  $J_c$  evaluation model described in Subsection 3.4.1 assumes perpendicularity

of the sample axis and the applied field. The ability of the VSM to rotate the sample during the measurement was used to assess the magnitude of this effect.

The two components of the magnetic moment measured by the VSM can easily be transformed into components in the sample frame of reference using the angle  $\beta$  between the axis of the sample and the applied field:

$$\begin{pmatrix} m_{\parallel} \\ m_{\perp} \end{pmatrix} = \begin{pmatrix} \cos(\beta) & -\sin(\beta) \\ \sin(\beta) & \cos(\beta) \end{pmatrix} \cdot \begin{pmatrix} m_p \\ m_o \end{pmatrix} \quad (3.19)$$

In the above expression  $m_{\parallel}$  and  $m_{\perp}$  are the components of the magnetic moment parallel and orthogonal to the sample axis, and the components  $m_p$  and  $m_o$  are the measured components parallel and orthogonal to the applied field.

Figure 3.13 shows the results of an angle dependence measurement on sample PIT-5. As apparent from Figure 3.13(b) the component  $m_{\perp}$  remains almost constant over a wide range when the angle between the sample axis and the applied field is varied from the ideal value of  $\beta = 90^\circ$ . This result demonstrates that small misalignments cannot have a significant effect on the quality of the data obtained by means of SQUID magnetometry.

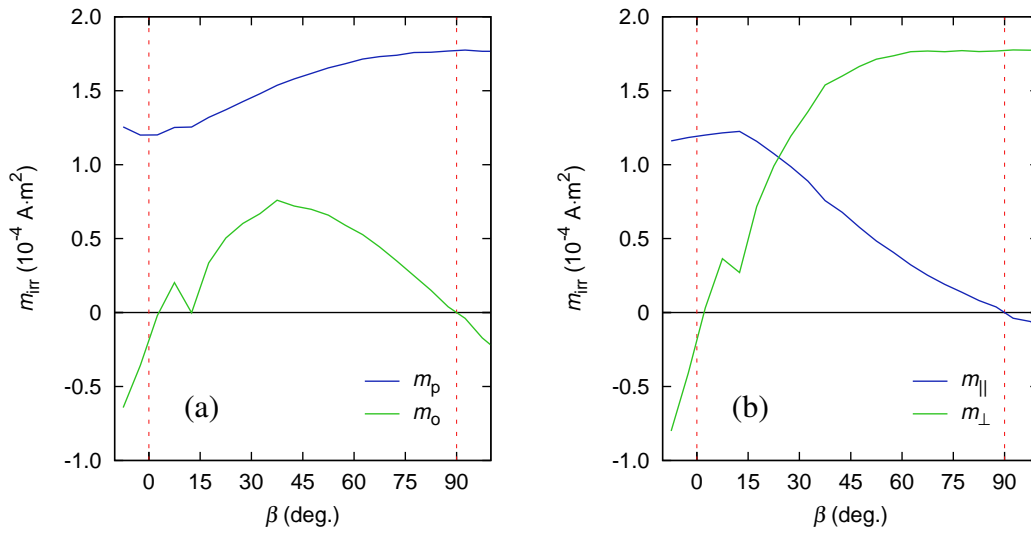


**Figure 3.13.:** Components of the irreversible magnetic moment as a function of the angle between the sample axis and the applied field. (a) VSM frame of reference. (b) Sample frame of reference.

## 3.3. Measurements in the 17 T system

The experimental set-up hereafter referred to as the 17 T system is comprised of a cryostat containing a superconducting magnet, several peripheral devices such as nanovoltmeters and a temperature controller, and a PC which controls all components of the system via GPIB. The cryostat is equipped with a VTI (variable temperature insert) which facilitates a precise control of the sample temperature in the gas cooled mode, and can also be flooded with liquid helium. The superconducting magnet is capable of generating magnetic fields of up to 15 T when the helium bath is at ambient pressure, and up to 17 T when the bath temperature is lowered sufficiently by reducing the pressure. Since this procedure is rather helium consuming (and hence costly), the magnet is usually not operated at field values in excess of 15 T. A photograph of the 17 T system is shown in Figure 3.14.

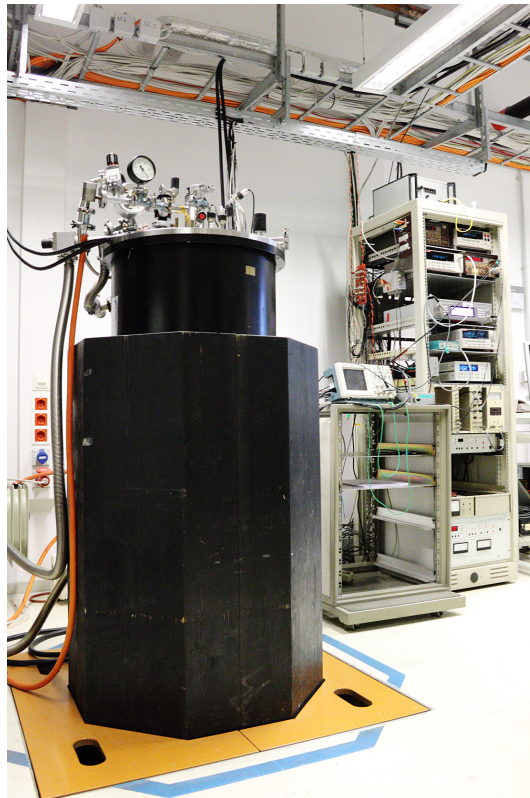


**Figure 3.14.:** Cryostat and instrument rack belonging to the 17 T system.

The 17 T system was used in combination with a current source capable of delivering 1000 A to perform transport measurements on samples prepared for this purpose (cf. Subsection 2.2.2). It was also used to measure the temperature dependence of the upper crit-

ical field of short wire samples by recording resistive transitions in an applied field while changing the temperature. The transport measurements are described in detail in Subsection 3.3.1, and the  $B_{c2}(T)$  measurements in Subsection 3.3.2.

### 3.3.1. Transport current measurements

The magnetization measurements described in Section 3.1 can be used to obtain the critical current density of the examined wire samples as well as its dependence on fast neutron fluence. Nevertheless, assessing  $J_c$  by means of transport critical current measurements was crucial for the following reasons:

- The  $J_c$  evaluation model described in Subsection 3.4.1 is based on simplifying assumptions and cannot be expected to yield exact results. Therefore, the validity of the  $J_c$  values obtained from the model had to be checked by means of transport measurements.
- The remaining deviation between magnetization data and transport results can be minimized by introducing an experimentally determined correction factor (cf. Subsection 3.4.6).
- In the SQUID magnetometer the maximum applied field is limited to 7 T, whereas transport measurements were carried out in applied fields of up to 15 T, which is much closer to the operating conditions the wires would be faced with in their intended application (cf. Section 1.1).

Before the commencement of the measurements for the *LHC Upgrade* project, the 17 T system was equipped for measuring critical currents of up to 300 A. Since this was insufficient for the examined wire types, a sample rod capable of carrying 1000 A as well as a current source capable of providing such high currents were provided by *CERN*.

#### Sample rod design

The dimensioning of the 1000 A sample rod was done by the author, whereas the design and fabrication were carried out at *CERN*. A software based on the sample rod dimensioning procedure described in [108] was implemented and used to simulate the performance of different designs. It assumes an initial value for the heat load  $\dot{Q}_L$  dissipated at the lower end of the rod by evaporation of liquid helium, and computes the temperature distribution

throughout the rod by subdividing it into thin slices. The heat flow conducted through an element with the index  $k + 1$  (the index increases towards the warm end) is given by

$$\dot{Q}_{k+1}^{\text{cond}} = \dot{Q}_k^{\text{cond}} + \dot{Q}_k^{\text{gas}} - \dot{Q}_k^{\text{Joule}}, \quad (3.20)$$

where  $\dot{Q}_k^{\text{gas}}$  and  $\dot{Q}_k^{\text{Joule}}$  are the heat flow into the gas and the Joule heating stemming from the element with the index  $k$ . The Joule heating is

$$\dot{Q}_k^{\text{Joule}} = \rho(T_k) \frac{\Delta z}{A_k} I^2, \quad (3.21)$$

where  $\rho(T_k)$  is the electric resistivity of the conductor element with the index  $k$ , its cross section is denoted by  $A_k$ ,  $\Delta z$  is the thickness of the slices, and  $I$  is the current. The heat flow into the gas can be described by the expression

$$\dot{Q}_k^{\text{gas}} = \dot{m} c_p \Delta T_k^{\text{gas}}. \quad (3.22)$$

In (3.22)  $\dot{m}$  is the helium mass flow, which is given by the heat load  $\dot{Q}_L$  and the enthalpy of vaporization of helium,  $c_p$  is the specific heat capacity of the gas, and  $\Delta T_k^{\text{gas}}$  describes the temperature change of the gas caused by the element with the index  $k$ . In [26] this temperature change is described by

$$\Delta T_k^{\text{gas}} = \frac{\Delta z}{\dot{m} c_p} h P (T_k - T_k^{\text{gas}}), \quad (3.23)$$

where  $h$  is a heat transfer coefficient (whose value was taken from [35]),  $P$  is an effective perimeter depending on surface properties (the circumference of the gas facing surface was used), and  $T_k - T_k^{\text{gas}}$  is the temperature difference between the conductor and the gas at the element with the index  $k$ . Using the above equations, the temperature distribution can be computed using

$$T_{k+1} = T_k + \frac{\dot{Q}_k^{\text{cond}}}{A_k \lambda(T_k)} \Delta z, \quad (3.24)$$

where  $\lambda(T_k)$  is the thermal conductivity of the element with the index  $k$ . If the computed temperature of the uppermost slice is different from room temperature by more than an allowed value, a new value for  $\dot{Q}_L$  is assumed and the computation starts again. Given an appropriate adjustment procedure for  $\dot{Q}_L$  this iteration converges quickly toward the correct heat load and temperature distribution.

A coaxial arrangement of the current leads was favored, since it facilitates a flow of helium gas between the conductors, thus providing efficient cooling. Designs with different numbers of stages (sections of constant conductor cross section) and different materials (copper and brass) were analyzed using the software. A three-stage sample rod consisting of coaxial brass leads in the upper section, coaxial copper leads in the middle section, and copper bus bars in the lower section appeared to be the most promising design. The brass reduces the heat conduction from the upper section into the cryostat, and the copper bus bars make it easy to disassemble and modify the lower section. A design drawing and a photograph of the 1000 A sample rod are shown in Figure 3.16, and Figure 3.15 shows the corresponding temperature profiles computed with the above described algorithm for the extreme cases of zero current and maximum current. The kink in the temperature profiles located at  $z \approx 0.9$  m (height measured from the cold end) corresponds to the transition from copper to brass.

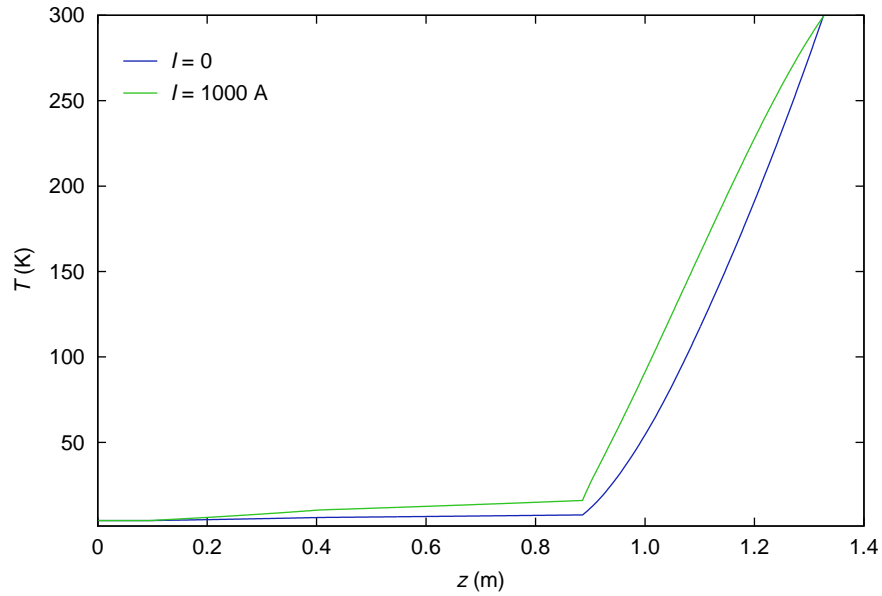


**Figure 3.15.:** Computed temperature profiles of the 1000 A sample rod, calculated by fixing the temperatures of the cold and the warm end to 4.2 K and 300 K, respectively.

### Measurement procedure

The wire samples used for transport measurements were wound on Ti-6Al-4V barrels equipped with copper rings at both ends, as described in Subsection 2.2.2. The lower end of the sample rod described above was designed for mounting such barrels by fastening a copper nut. This nut establishes electrical contact between one of the copper rings



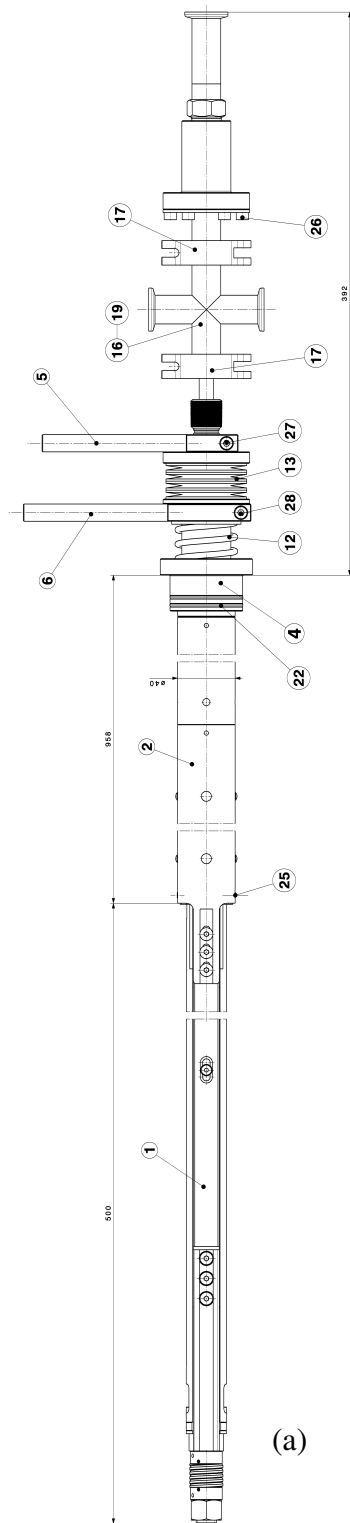


**Figure 3.16.:** 1000 A sample rod used for transport measurements. (a) Design drawing (broken at three points to keep the aspect ratio reasonable). (b) Photograph.

on the barrel and a threaded copper rod which is the lower end of the inner current lead. The other end of the barrel is pressed against a ring-shaped copper structure belonging to the outer current lead when the nut is fastened. In order to obtain a sufficiently low contact resistance, flat indium rings were inserted between the copper rings of the barrel and the parts in contact with them. These rings were made from indium wire by forming circles and hammering them until their width was approximately equal to the width of the copper rings on the transport sample barrels. Figure 3.17 shows a photograph of a transport sample mounted on the 1000 A sample rod. Some of the copper parts of the sample rod are gold coated, hence their color is yellowish in the picture.

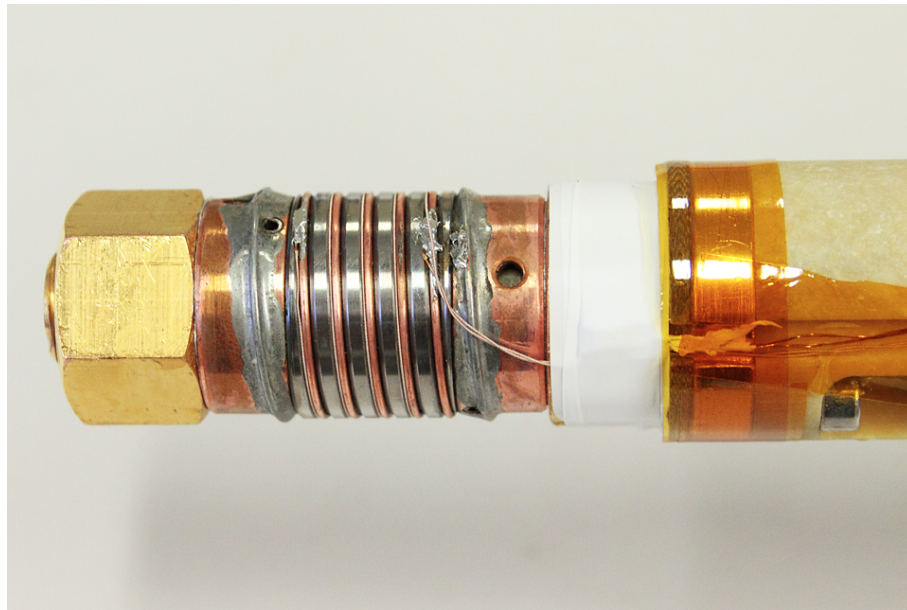


**Figure 3.17.:** Transport sample TiR-T1 mounted on the 1000 A sample rod. Electrical contact is established via flat indium rings by fastening the nut at the end of the rod.

A calibrated type *CX-1050-SD* temperature sensor purchased from *Lake Shore Cryotronics* was mounted on the ring-shaped structure directly above the barrel (covered with white PTFE tape in the photograph). *Apiezon N* grease was used to establish a good thermal contact between the metal and the sensor. Voltage taps were made by soldering thin copper wires insulated with varnish and tissue to the wire sample at two points approximately 28 cm (four windings) apart. The one closer to the lower end of the sample rod was then wound back along the sample until it met the other wire. From this point the two wires continued as a twisted pair line to a small circuit board mounted on the sample rod, where they were soldered to wires leading to a connector located at the top end of the rod. This

procedure is crucial for keeping the induced voltage low when high current ramp rates are used.

After finishing the sample mounting procedure, the 1000 A rod was inserted into the cryostat of the 17 T system, and slowly cooled down. Meanwhile the current leads of the sample rod were connected to the computer controlled current source using suitable copper cables. When the temperature measured by the sensor near the barrel indicated that the sample was immersed in liquid helium, a resistance measurement was carried out to ensure a good electrical connection. This was done by ramping up the current to 100 A while measuring the voltage drop across the lower end of the sample rod (from the center of one bus bar to the center of the other). If the connection is good, which was usually the case, the measured resistance is around  $2\ \mu\Omega$ .

Transport measurements were performed at different values of the applied field, starting at 15 T and decreasing the field in steps of 1 T or 0.5 T, depending on the expected field value at which  $I_c$  exceeds 1000 A. The software used to control the current source is capable of performing a two-stage measurement with different current ramp rates: a fast ramp rate up to a value close to  $I_c$ , followed by a slower ramp rate until a certain voltage criterion (corresponding to a field criterion well above  $10\ \mu\text{V/m}$ ) is reached. The fast ramp rate keeps the duration of the measurement short, thereby reducing Joule heating, whereas the slower one ensures that enough data points are collected in the flux creep domain. Typical ramp rates at high critical currents were 100 A/s and 25 A/s, while a single ramp rate around 20 A/s was sufficient at comparatively low critical current values ( $I_c \lesssim 300\ \text{A}$ ). The sample voltage was measured with a *Keithley 2182A* nanovoltmeter at a rate of approximately four measurements per second, and saved to a data file on the controller PC. The exact current was determined by measuring the voltage drop across a  $50\ \mu\Omega$  shunt with a *Keithley 2000* multimeter.

As an example for the raw data obtained by the method described above, the voltage-current data points (commonly referred to as V-I curve) of the unirradiated sample TiR-T1 at an applied field of 12 T is shown in Figure 3.18. The deviations from a flat line occurring well below the critical current are probably the result of thermoelectric voltages. Such voltage drifts are undesirable, but they can be ironed out in the evaluation.

All transport measurements were performed in liquid helium at ambient pressure, which corresponds to a temperature of 4.2 K. Nonetheless, the output of the temperature sensor

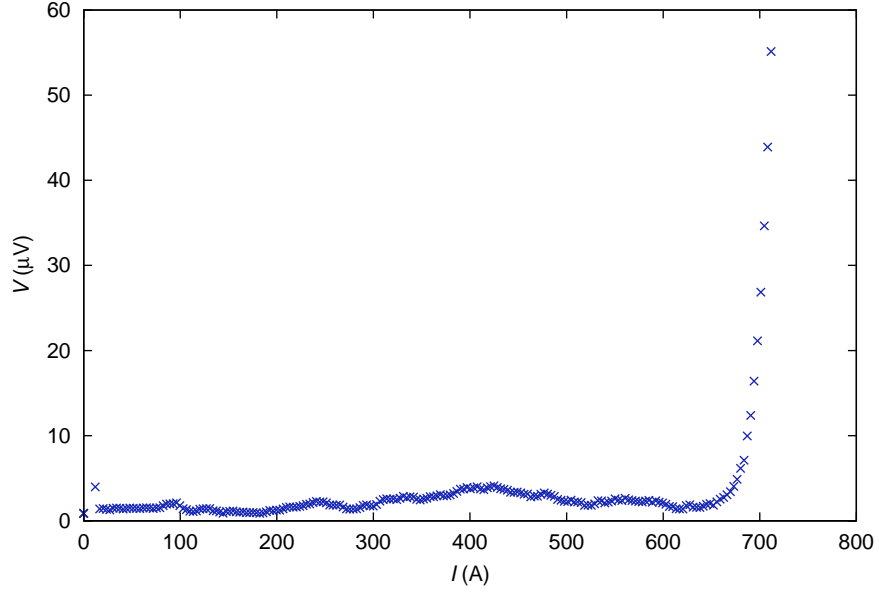


**Figure 3.18.:** Raw data (V-I curve) of a transport measurement performed on sample TiR-T1 at an applied field of 12 T.

near the sample was monitored during the measurements, and the temperature values measured at the beginning and at the end of each transport measurement process were recorded. This was done to assess the sample warming, which is caused by two effects: the Joule heating in the normal conducting components near the sample (copper rings on the barrel, indium rings, copper parts in the lower end of the sample rod), and the pressure increase in the VTI due to evaporation of helium, leading to an increase of the boiling point. Near the critical current the dissipation within the wire sample is an additional heat source. The temperature increase measured by the sensor was 7 mK on average for measurements in which  $I_c$  exceeded 500 A. Significantly higher temperature increases were observed when the fast current ramp rate was set too low, which usually lead to a quench of the sample.

Special care had to be taken when working with irradiated transport samples (cf. Section 2.3). Long tweezers with silicon rubber pads at the ends were used for sample handling instead of directly touching the samples, thus reducing radiation exposure (the dose rate of the most radioactive transport sample was 400  $\mu\text{Sv/h}$  at a distance of 30 cm at the time of the measurement). Since the samples had been sealed in normal air atmosphere before irradiation, the copper rings as well as the copper matrix of the wire sample suffered from oxidation during irradiation. The result of this process is a black layer of cupric oxide ( $\text{CuO}$ ), which prevents soldering as well as low-resistance pressure contacts. It had to be removed with hydrochloric acid before mounting the samples on the sample rod.

The four unirradiated transport samples RRP-T1, TiR-T1, TiR-T2, and P07-T2 were successfully measured, and three of them (TiR-T1, TiR-T2, and P07-T2) were subsequently irradiated. Unfortunately, three samples of the P07 type turned out to be broken during the measurement (P07-T1, P07-T3, and P07-T4), which is why only one sample of this type was included in the irradiation program. After irradiation only sample TiR-T2 (irradiation step 13,  $\Phi_f t = 3.7 \cdot 10^{21} \text{ m}^{-2}$ ) was measured successfully, whereas samples TiR-T1 and P07-T2 (irradiation step 12,  $\Phi_f t = 8.0 \cdot 10^{21} \text{ m}^{-2}$ ) turned out to be broken. The former exhibited transitions at currents lower than the expected critical current by a factor of 10, and the latter quenched at currents about 50% below the expected  $I_c$ . A visual inspection gave no clue as to how these samples were damaged. Since both samples were irradiated in the same step (and hence the same aluminum capsule), it appears likely that the damage occurred during sealing or in the course of the irradiation procedure.

The evaluation procedure used to obtain critical current values from the raw data files as well as the self-field correction, which is necessary due to the high values of  $I_c$ , are described in Subsection 3.4.4 and Subsection 3.4.2. The results of the transport measurements on the unirradiated samples and on irradiated sample TiR-T2 are discussed in Subsection 3.4.6 and Subsection 4.2.1, respectively.

#### 3.3.2. Upper critical field measurements

The 17 T system was also used to measure the upper critical field of short wire samples as a function of temperature. Actually, the critical temperature at constant applied field was measured by applying a current of 100 mA and lowering the temperature in the VTI from above  $T_c$  while measuring the voltage drop across the sample. Since the applied field was limited to 15 T (the helium bath pressure was not reduced),  $B_{c2}$  could only be determined at high temperatures ( $T \gtrsim T_c/2$ ).

These measurements were carried out with straight wire samples roughly 2 cm in length, which are described in Subsection 2.2.3, as well as irradiated magnetization samples (cf. Subsection 2.2.1). The samples were mounted perpendicular to the applied field on an epoxy sample holder equipped with copper paths designed for four-terminal sensing. Electrical contact (as well as mechanical fixing) was established by soldering in case of the longer samples, and by applying silver conductive paint in case of the magnetization samples. Both situations are shown in Figure 3.19.

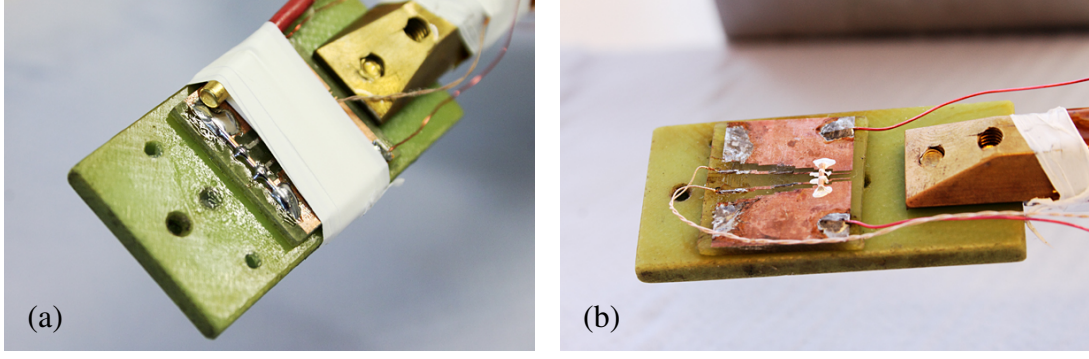


**Figure 3.19.:** Samples mounted for  $B_{c2}(T)$  measurements. (a) Sample P07-R1 (prepared for this purpose). (b) Irradiated sample TiR-2 (normally used for magnetization measurements).

One unirradiated sample of each type (RRP-R1, PIT-R1, TiR-R1, BIN-R1, and P07-R1) was measured in the above described way, as well as the irradiated samples BIN-2 (step 13), TiR-2 (step 13), and P07-1 (step 12). Figure 3.20 shows the raw data of a  $B_{c2}$  measurement on sample P07-R1 at an applied field of 9 T. The evaluation procedure used to obtain  $B_{c2}(T)$  curves from the raw data is described in Subsection 3.4.8, and the results obtained from unirradiated and irradiated samples are discussed in Subsection 4.1.3 and Subsection 4.2.3, respectively.

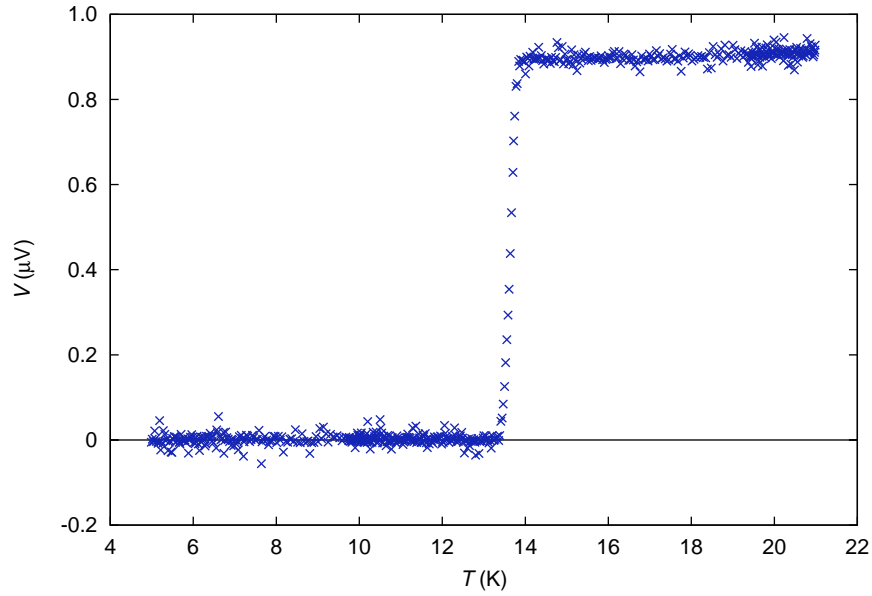


**Figure 3.20.:** Raw data of a  $B_{c2}$  measurement performed on sample P07-R1 at an applied field of 9 T using a constant current of 100 mA.

## 3.4. Data evaluation

### 3.4.1. Model for the evaluation of $J_c$ from magnetometry data

Magnetization measurements were used to obtain the critical current density of short wire samples in the unirradiated state and after each irradiation step (cf. Section 3.1 and Section 3.4.5). This  $J_c$  evaluation requires knowledge of the relationship between the critical current density and the irreversible magnetic moment of the sample. In general, the magnetic moment of a current distribution  $\vec{J}(\vec{r})$  is given by

$$\vec{m} = \frac{1}{2} \int \vec{r} \times \vec{J}(\vec{r}) d^3r. \quad (3.25)$$

The following derivation is based on the Bean model [9], which assumes that the local critical current density can only take on the values  $\pm J_c$ . With this assumption the current density inside a fully penetrated superconductor can be cast in the form

$$\vec{J}(\vec{r}) = J_c \vec{e}_J(\vec{r}), \quad (3.26)$$

where  $\vec{e}_J(\vec{r})$  is the local direction of the current. In this case (3.25) becomes

$$\vec{m}_{\text{irr}} = \frac{J_c}{2} \int \vec{r} \times \vec{e}_J(\vec{r}) d^3r, \quad (3.27)$$

which means that the irreversible magnetic moment<sup>3</sup> of the superconductor is proportional to its critical current density, and that the proportionality factor is determined by the sample geometry and the magnetization history.

In a multifilamentary wire consisting of several twisted hollow sub-elements, the basic superconductor geometry is a helical tube. Since the goal is to evaluate the field dependence of  $J_c$  the wire would exhibit in its intended application as part of a magnet, it is prudent to apply the field perpendicular to the wire. The critical state of a helical tube oriented transverse to the applied field is not obvious, and its calculation is rather complex. Therefore, it is practical to assume a similar geometry which simplifies the calculation of the proportionality factor: parallel hollow cylinders. This approximation should be valid if the twist

---

<sup>3</sup>The reversible moment  $m_{\text{rev}}$  does not depend on  $J_c$ , and can be subtracted easily from the measured total magnetic moment  $m = m_{\text{irr}} + m_{\text{rev}}$  (cf. Section 3.1).

pitch length is much greater than the wire diameter, and if the sub-element cross section does not differ significantly from a circular geometry.

In the following calculation the coordinate system is such that the  $x$ -axis coincides with the symmetry axis of a hollow cylinder in an applied magnetic field which is parallel to the  $z$ -axis. The magnetic moment of the hollow cylinder can be calculated by integrating the contributions of current loops with infinitesimal cross sections. Assuming that the current flows in planes perpendicular to the applied field (parallel to the  $x$ - $y$ -plane), these current loops are flat, and the infinitesimal magnetic moment of such a loop is given by

$$d\vec{m} = dA J_c A_l \vec{e}_z. \quad (3.28)$$

In the above expression  $dA$  is the infinitesimal cross section through which a current with the density  $J_c$  flows,  $A_l$  is the area spanned by the loop, and  $\vec{e}_z$  is the unit vector in  $z$ -direction. Obviously the assumption of flat current loops is an approximation, since the hole in the cylinder must lead to a deviation from this simple geometry. Assuming that this effect is localized near the ends of the hollow cylinder (bending of current paths which would otherwise intersect the void), this calculation should be valid provided the length of the hollow cylinder is much greater than its inner diameter. Using cylindrical coordinates, the cross section and the area of a loop can be cast in the following form.

$$dA = dr r d\varphi \quad (3.29)$$

$$A_l = 2r \cos(\varphi) L \quad (3.30)$$

In (3.30)  $L$  is the length of the current loop in  $x$ -direction. If the length of the hollow cylinder is much greater than its diameter,  $L$  can be set equal to the cylinder length for all infinitesimal current loops without introducing a significant error. Using the above expressions, (3.28) becomes

$$d\vec{m} = J_c 2L r^2 dr d\varphi \cos(\varphi) \vec{e}_z. \quad (3.31)$$

The irreversible magnetic moment of a superconducting hollow cylinder can be obtained by integrating (3.31) over the volume of the hollow cylinder. Assuming that coupling effects between the sub-elements in a short sample of a multifilamentary wire are negligible, the irreversible magnetic moment of the sample is the product of the hollow cylinder



moment and the number of sub-elements  $N$ :

$$\begin{aligned}\vec{m}_{\text{irr}} &= 2N \int_{r=\rho_i}^{\rho_o} \int_{\varphi=0}^{\pi/2} d\vec{m} = 4J_c NL \vec{e}_z \int_{\rho_i}^{\rho_o} r^2 dr \int_0^{\pi/2} \cos(\varphi) d\varphi \\ &= \frac{4}{3} J_c NL (\rho_o^3 - \rho_i^3) \vec{e}_z\end{aligned}\tag{3.32}$$

In (3.32)  $\rho_i$  and  $\rho_o$  are the inner and outer sub-element radii, and the prefactor 2 takes into account that integrating over  $\varphi$  from 0 to  $\pi/2$  includes only current loops above the  $x$ - $y$ -plane. Using the above result, the critical current density of the sample can be evaluated by measuring its irreversible magnetic moment parallel to a magnetic field which is applied perpendicular to the sample axis. The hollow cylinder model equation used in this work for evaluating  $J_c$  from magnetization data is

$$J_c = \frac{3m_{\text{irr}}}{4NL(\rho_o^3 - \rho_i^3)}.\tag{3.33}$$

This model as well as results obtained by using it to evaluate magnetization measurements<sup>4</sup> were published by the present author et al. in [8]. An expression equivalent to (3.33) was used by Lindenhovius et al. to assess the sub-element diameters of powder-in-tube  $\text{Nb}_3\text{Sn}$  wires based on magnetization and transport measurements [77]. Ghosh and Suenaga pointed out that bridging between filaments can lead to large deviations between the actual filament diameter and the one obtained from magnetometry. Results which support the assumption of negligible coupling between the sub-elements of the wires examined in the present work are presented in Subsection 3.4.5. In [54] Godeke et al. used the expression given in [77] to evaluate the critical current density of powder-in-tube wires from magnetization measurements. An alternative derivation of the magnetization of a hollow cylinder as a function of  $J_c$  was published by Sumption et al. in [124].

All  $J_c$  values presented in this work are to be understood as critical current densities in the A-15 region of the respective wire, in accord with the above described evaluation model. The engineering critical current density  $J_E$ , which is the current density averaged over the wire cross section, can be calculated by multiplying  $J_c$  with the ratio of the A-15 cross

---

<sup>4</sup>These measurements were performed with the standard sample transport before the problems arising from this method (cf. Subsection 3.1.2) were known. Hence the standard sample transport correction (cf. Subsection 3.4.3) was not applied, and the results are thus obsolete.

section  $N\pi(\rho_o^2 - \rho_i^2)$  and the wire cross section  $\pi R^2$ , yielding

$$J_E = J_c \frac{N(\rho_o^2 - \rho_i^2)}{R^2}, \quad (3.34)$$

where  $R$  is the radius of the wire (cf. Subsection 2.1.1).

### 3.4.2. Self-field correction

When measurements on a superconductor are carried out while a transport current is applied or a current pertaining to the irreversible magnetization of the sample is present, the magnetic field generated by this current may need to be considered. This field is referred to as the self-field  $B_{sf}$ , whose presence is relevant if its magnitude is not negligible compared to the applied field  $B_a$ .

The results obtained from transport measurements (cf. Subsection 3.3.1) were self-field corrected using a method described by Bordini, which is based on a finite element calculation [15]. The analysis in the cited reference was done for a multifilamentary wire wound on an *ITER VAMAS* barrel with its axis parallel to the applied field, and the Lorentz force pressing the wire towards the barrel. The result is that the peak transverse field experienced by the wire can be approximated by

$$B_p = B_a + B_{sf} \quad \text{with} \quad B_{sf} = I \left( \frac{\mu_0}{2\pi R} - 9 \cdot 10^{-5} \text{ T/A} \right), \quad (3.35)$$

where  $I$  is the current, and  $R$  is the distance between the center of the wire and its outermost sub-element. Although the barrels used in the present work are smaller than *ITER VAMAS* barrels (cf. Subsection 2.2.2), the above result can still be used for self-field corrections, since the main contribution in (3.35) stems from the internal structure of the wire, and the angle between the wire and the applied field is comparable to the value in [15].

In SQUID magnetization measurements (cf. Section 3.1) the irreversible magnetic moment  $m_{irr}$  of the sample is obtained from the difference between the magnetic moments measured in decreasing and in increasing applied field. The slope of the magnetization profile and hence the direction of the irreversible currents in the sample has a different sign in the increasing and the decreasing branch of the magnetization curve. When the magnetic moment is plotted as a function of the magnetic field inside the superconductor, the increasing field branch is thus shifted towards lower values, and the decreasing field branch towards

higher values relative to the applied field. Therefore, the irreversible magnetic moment as a function of magnetic field is given by

$$m_{\text{irr}}(B) = \frac{1}{2} \left( m_{\text{dec}}(B = B_a + B_{\text{sf}}) - m_{\text{inc}}(B = B_a - B_{\text{sf}}) \right), \quad (3.36)$$

where  $m_{\text{dec}}(B)$  and  $m_{\text{inc}}(B)$  denote the magnetic moments measured in decreasing and in increasing field, respectively, and  $B_{\text{sf}}$  is an effective self-field which depends on the critical current density. From (3.36) it is clear that the method by which  $m_{\text{irr}}$  is obtained already entails a first-order self-field correction, leaving only higher order terms which arise from the non-linearity of  $m_{\text{irr}}(B)$ .

The effect of the self-field present during the magnetization measurements described in Section 3.1 was analyzed using a software code which carries out the following computations:

- Break up a single sub-element into line elements, each one carrying a fraction of the total current.<sup>5</sup>
- Compute the magnetic field distribution generated by this single sub-element.
- Obtain the field distribution in the entire wire cross section by superposition of the contributions generated by each sub-element.
- Use a weighting function  $f_w$  to calculate an effective value of the self-field.

The necessity of a weighting function arises from the fact that in the hollow cylinder model the contribution of each infinitesimal current loop (cf. Subsection 3.4.1) is proportional to its width. Hence, the weighting function within the sub-element cross section is simply  $f_w = C|x|$ , where  $x$  is the distance of the point of interest from the vertical (parallel to the applied field) symmetry axis, and  $C$  is a factor required for normalization. An effective self-field within each sub-element can then be calculated by averaging the weighted field values over the sub-element cross section. After that the effective self-field  $B_{\text{sf}}$  of the entire sample can be obtained by averaging over the self-field values of all sub-elements.

In Figure 3.21 the results obtained from the above described software code are shown for an RRP type magnetization sample and a critical current density of  $5.8 \cdot 10^{10} \text{ A/m}^2$ , which was previously found to be the approximate zero-field  $J_c$  value of a particular RRP sample at a temperature of 10 K. The absolute values of the self-field as a function of position within the wire cross section are depicted in Figure 3.21(a), and the average weighted

---

<sup>5</sup>The hollow cylinder approximation described in Subsection 3.4.1 was used to simplify the geometry, and the change of the current direction at the ends of the sub-element was neglected.

self-field components parallel to the applied field (the other components are significantly smaller) for each sub-element are shown in Figure 3.21(b). Even though self-field values of close to 1.25 T can be found within small regions of the sub-elements, the weighted average values for each sub-element do not exceed 0.35 T at the specified critical current density. Calculating the average of all the sub-element average values in order to obtain an effective self-field for the entire sample yields  $B_{\text{sf}} = 0.140$  T. The influence of the self-field

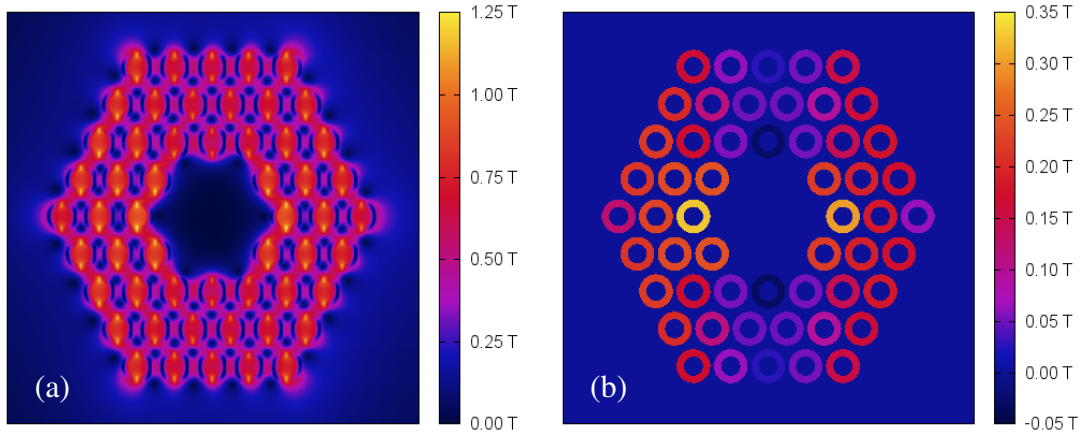


**Figure 3.21.:** Simulated self-field of an RRP type sample for  $J_c = 5.8 \cdot 10^{10}$  A/m<sup>2</sup>. **(a)** Field distribution in the wire cross section (absolute values). **(b)** Average weighted values for each sub-element (component parallel to the applied field).

can be directly observed by measuring a four-quadrant magnetization loop: The minimum of the curve measured in increasing field and the maximum of the curve measured in decreasing field are shifted relative to the  $B_a = 0$  axis by a value which can be regarded as the effective self-field present at the zero-field critical current density. This experiment was carried out with the RRP sample whose  $J_c$  in zero applied field at  $T = 10$  K was used in the simulation. Figure 3.22 shows the measurement results including parabolic fits which were used to locally approximate the curves in order to determine the positions of the extreme values, which are located at  $B_a = -0.146$  T and  $B_a = 0.144$  T. The resulting average shift of 0.145 T is in very good agreement with the simulation result of  $B_{\text{sf}} = 0.140$  T. The small value of the effective self-field at a relatively high critical current density of  $5.8 \cdot 10^{10}$  A/m<sup>2</sup> and the fact that a first-order correction is inherent in the calculation of  $m_{\text{irr}}$  suggest that no additional self-field correction of magnetization measurements is necessary. Therefore, the  $J_c$  data obtained from SQUID magnetometry were not self-field corrected, and the equality  $B = B_a$  was assumed for these measurements.

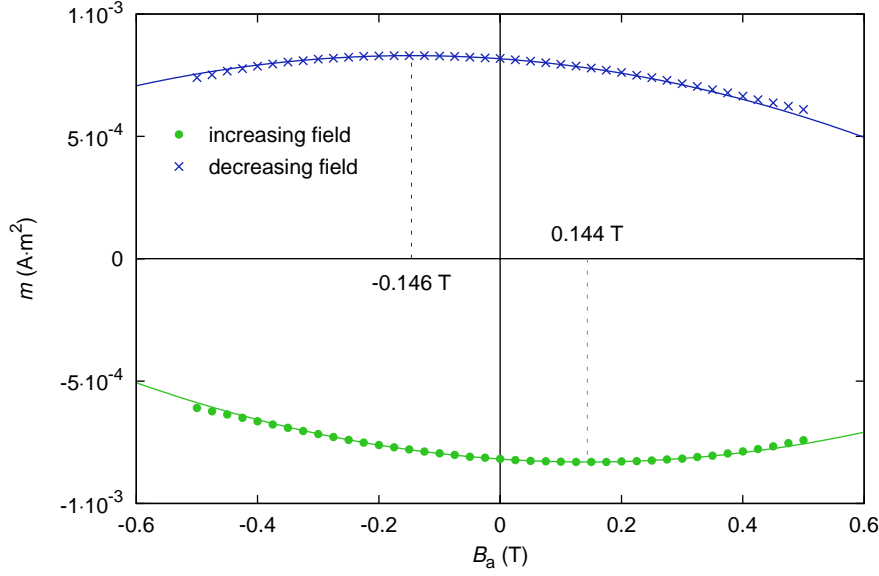


**Figure 3.22.:** Four-quadrant magnetization measurement of sample RRP-2 at  $T = 10$  K, showing the effect of the self-field. The shifts of the extreme values (dashed lines) of the curves were assessed using a parabolic fit function.

### 3.4.3. Standard sample transport correction

It was pointed out in Subsection 3.1.2 that magnetization measurements in the *MPMS XL* SQUID magnetometer suffered from an untoward decrease of the measured magnetic moment when the standard sample transport was used. This effect, which is particularly pronounced at high temperatures and applied field values, was found when the results of such measurements were compared to measurements performed with the RSO (cf. Subsection 3.1.3), and was attributed to the shaking field effect. In most cases the “old” standard sample transport measurements could not be redone using the RSO, since the samples had meanwhile been irradiated. Therefore, a correction formula was devised which reconciles the differences between the two measurement methods by adjusting the values obtained using the standard sample transport. The expression

$$\frac{m_{\text{irr}}^{(\text{SST})}(T, B)}{m_{\text{irr}}^{(\text{RSO})}(T, B)} = 1 - a(T) B^{1+hT} \quad (3.37)$$

was found to accurately describe the ratio of the irreversible magnetic moments obtained using the standard sample transport and the RSO, respectively. Note that this is a purely empirical expression, which was used owing to the failure of reasonably simple physically

motivated formulas. Average values of standard sample transport and RSO measurement results obtained from unirradiated samples were used as input data of a fit procedure which determines the most suitable  $a(T)$  and  $h$ . The parameter  $a(T)$  was determined for each sample type and temperature value separately, whereas  $h$  only depends on the sample type.

The standard sample transport correction is demonstrated for unirradiated P07 samples in Figure 3.23: Significant deviations between RSO measurements (solid lines) and data obtained using the standard sample transport (the error bars indicate the standard deviation) can be seen in Figure 3.23(a). When the standard sample transport data are corrected according to (3.37), the agreement with the RSO measurements is satisfactory, as shown in Figure 3.23(b). When applied to data obtained from irradiated samples, the procedure was also found to produce a satisfactory correction.

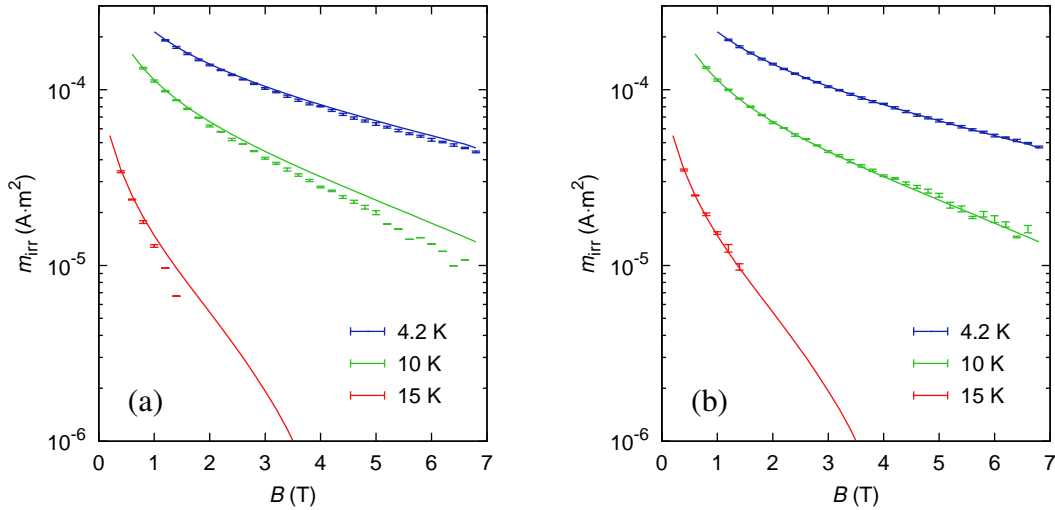


**Figure 3.23.:** Irreversible magnetic moment of P07 samples (average values) as a function of field measured at different temperatures. Solid lines represent RSO data, error bars indicate  $\pm 1\sigma$  of the standard sample transport measurements. (a) Original data. (b) Values after standard sample transport correction.

The above described correction was applied to all magnetization measurements performed with the standard sample transport. All critical current density and volume pinning force results presented in the following, which were obtained from SQUID magnetometry, are either based on RSO data or corrected data from standard sample transport measurements.

### 3.4.4. $I_c$ from transport measurements

The critical current of wire samples wound on Ti-6Al-4V barrels (cf. Subsection 2.2.2) was obtained from transport measurements performed at a temperature of 4.2 K in applied fields of up to 15 T, as described in Subsection 3.3.1. In transport measurement data the transition from the superconducting to the normal state can usually be described in good approximation by the power law

$$V = C I^n, \quad (3.38)$$

where  $I$  is the applied current,  $V$  is the measured voltage, and  $n$  is the index of the transition (often simply referred to as the  $n$ -value). The prefactor  $C$  is usually not of interest in the context of critical current measurements. The evaluation of the raw data was performed using an algorithm which takes advantage of the fact that power functions appear linear in log-log plots. It performs the following tasks:

- Prompt the user for two current values which define the baseline, and compute a linear fit to the data between these values.
- Perform a baseline correction by subtracting the baseline function from the data.
- Detect the onset of the transition by comparing the average voltage of a certain number of data points to a threshold criterion.
- Calculate the logarithm of the current  $I$  and voltage  $V$  of each data point, and remove points whose voltage is below a threshold value.
- Fit a linear function to the logarithmic data, including only points whose  $I$  value is greater than the onset current.
- Obtain the critical current  $I_c$  by calculating the intersection of the fit function with a (logarithmic) voltage criterion. The  $n$ -value is given by the slope of the linear fit.
- Perform a self-field correction by calculating the effective magnetic field inside the superconductor using (3.35) with  $I = I_c$ .

The deviations of the raw transport measurement data from a flat line occurring well below the critical current are probably the result of thermoelectric voltages. Since they tend to be different in each measurement, the current range within which the baseline fit was computed was determined by visual inspection of the data. Omission of the baseline correction leads to a change in the resulting  $I_c$  value of typically  $\pm 1\%$ . The voltage criterion was calculated by multiplying an electric field criterion of  $E_c = 10^{-5}$  V/m, which is commonly used for transport measurements on low-temperature superconductors, with the length of

wire between the voltage taps. This length was typically 28 cm, corresponding to four windings on the barrel (cf. Subsection 2.2.2), which gives a voltage criterion of  $2.8 \mu\text{V}$ .

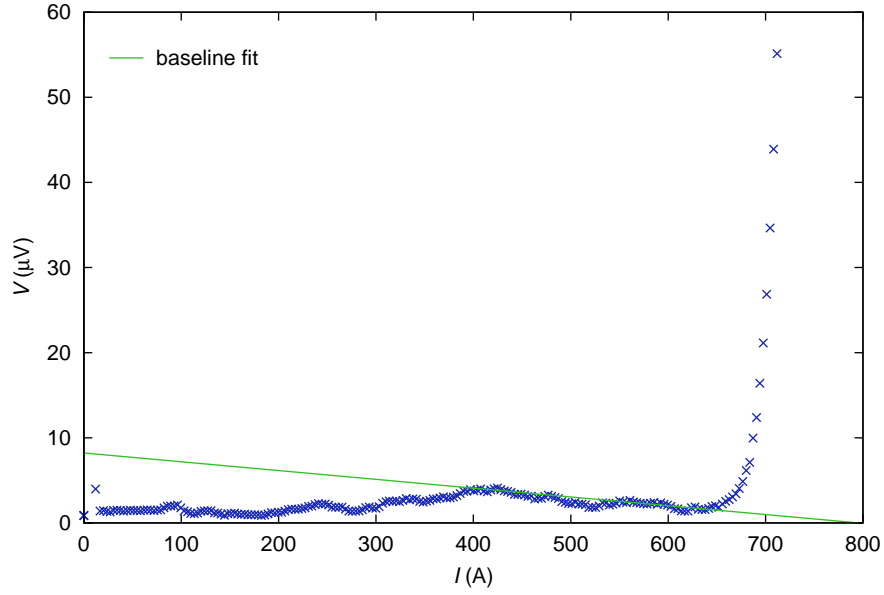


**Figure 3.24.:** Raw data of a transport measurement on unirradiated sample TiR-T1 at 4.2 K and 12 T. The baseline fit is a linear function based on data within a user-defined range.

The above described method was used to evaluate the critical current of all examined transport samples as a function of magnetic field including the self-field contribution, which was calculated as described in Subsection 3.4.2. Results obtained from this procedure are discussed in Subsection 3.4.6 and Subsection 4.2.1.

### 3.4.5. $J_c$ from SQUID magnetometry

The critical current density  $J_c$  of magnetization samples (cf. Subsection 2.2.1) was evaluated from their irreversible magnetic moment, which was obtained from the SQUID data using

$$m_{\text{irr}}(B_a) = \frac{1}{2} \left( m_{\text{dec}}(B_a) - m_{\text{inc}}(B_a) \right). \quad (3.39)$$

In (3.39)  $m_{\text{inc}}(B_a)$  is the magnetic moment measured in increasing field, and  $m_{\text{dec}}(B_a)$  is the value measured in decreasing field. As explained in Subsection 3.4.2, a self-field correction of SQUID measurements is not necessary, which is why the field  $B$  inside the



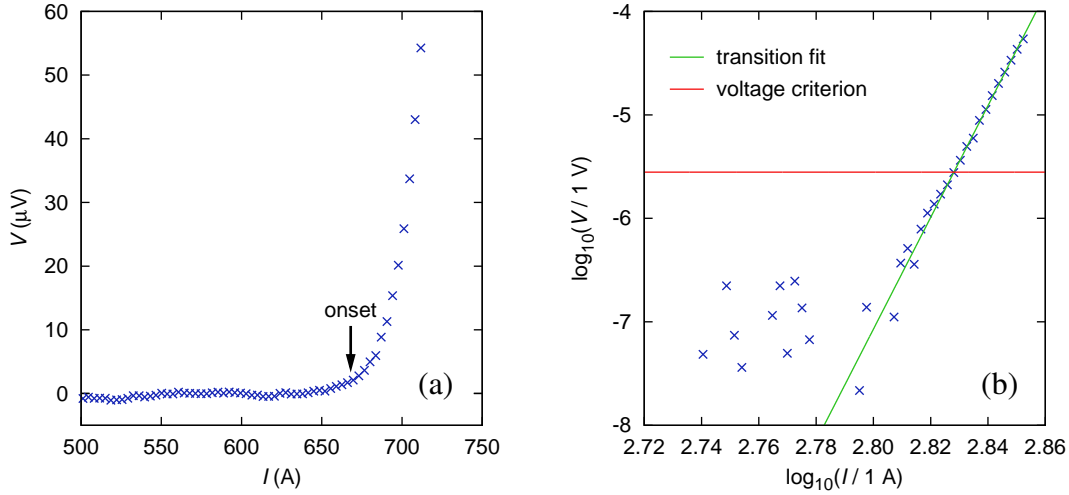


**Figure 3.25.:** Illustration of the  $I_c$  evaluation algorithm. **(a)** Baseline corrected data and transition onset determined from threshold criterion. **(b)** Transition region viewed in a log-log plot, logarithmic voltage criterion, and linear fit to data points in the transition region.

superconductor can be assumed to be equal to the applied field  $B_a$ . The relationship between  $J_c$  and  $m_{\text{irr}}$  is given by

$$J_c = \frac{3m_{\text{irr}}}{4NL(\rho_o^3 - \rho_i^3)}, \quad (3.40)$$

as derived in Subsection 3.4.1. In the above expression  $N$  is the number of sub-elements in the sample,  $L$  is the sample length, and  $\rho_o$  and  $\rho_i$  are the outer and inner sub-element radii. The latter were obtained from scanning electron microscopy, as discussed in Subsection 2.1.1. The evaluation of  $J_c(T, B)$  from SQUID magnetometry data was automated by designing a software code which performs the following operations:

- Locate the relevant SQUID data files, and extract  $m_{\text{irr}}(B)$  for each temperature value at which magnetization loops were measured.
- In case of measurements carried out using the standard sample transport, perform the correction procedure described in Subsection 3.4.3.
- Calculate  $J_c(B)$  for each temperature value using (3.40).
- Exclude data points which suffer from flux jumps or incomplete penetration of the magnetization profile.
- Remove data points whose  $J_c$  value is below a certain threshold which depends on

the resolution limit of the measurement method.<sup>6</sup>

The above described  $J_c$  evaluation was carried out for each magnetization sample and each irradiation step in which that sample was included. This procedure allowed the detailed assessment of fast neutron irradiation induced changes in the critical current density, as discussed in Subsection 4.2.1. The results obtained from unirradiated samples as well as the homogeneity of the magnetization along the wire are the subject matter of Subsection 4.1.1.

The  $J_c$  evaluation model described in Subsection 3.4.1 is based on the assumption that the coupling between the sub-elements is negligible. The validity of this assumption was tested by performing magnetization measurements on individual sub-elements with the RSO (cf. Subsection 3.1.3). These sub-elements were extracted from short wire samples by means of etching with nitric acid, as described in Subsection 2.2.1. Figure 3.26 shows a comparison of the irreversible magnetic moment of a TiR wire sample with the results obtained from three individual sub-elements extracted from another TiR sample. The sub-element data are scaled with the number of sub-elements in the wire (108 in this case), and a factor which compensates for the slightly different lengths of the sub-elements and the wire sample (4.4 mm as opposed to 4.1 mm). Considering that large deviations can be found in the shape of the sub-element cross sections in SEM images, the agreement between the magnetization curve of the wire sample and the data obtained from individual sub-elements is very good, which supports the assumption of negligible sub-element coupling. An absence of sub-element coupling was also reported by Bordini et al. who performed magnetization measurements on two of the wire types examined in this work (RRP and PIT), and found no dependence of the magnetization (magnetic moment per volume) on wire length [16].

### 3.4.6. Comparison of magnetometry and transport results

The critical current values obtained from transport measurements (cf. Subsection 3.4.4) and the critical current density data obtained from SQUID magnetometry (cf. Subsection 3.4.5) were compared in order to assess the quality of the  $J_c$  evaluation model and to calculate correction factors. Due to the limitations of the two measurement methods

---

<sup>6</sup>For measurements performed with the standard sample transport the relatively high threshold value of  $10^9$  A/m<sup>2</sup> had to be used to ensure a reasonable accuracy of the data corrected according to Subsection 3.4.3.

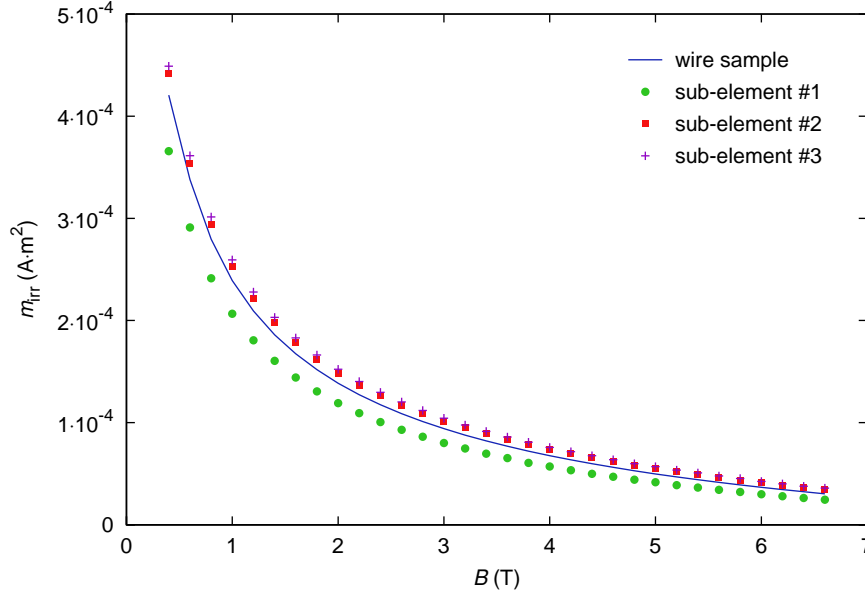


**Figure 3.26.:** Comparison of the irreversible magnetic moment of a TiR type magnetization sample with the moments of three individual sub-elements of the same type, scaled by the number of sub-elements in the wire and a length correction factor.

(1000 A maximum transport current, and 7 T maximum applied field, respectively), there is no overlap in the field values, thus making a direct comparison impossible. The comparison was made by extrapolating the magnetometry results to the field range in which critical current values obtained from transport measurements are available. The function

$$F_p^{(\text{mag})}(B) = C \left( \frac{B}{B_{c2}^*} \right)^p \left( 1 - \frac{B}{B_{c2}^*} \right)^q \quad (3.41)$$

was fit to the volume pinning force values  $F_p^{(\text{mag})} = J_c^{(\text{mag})} B$  obtained from SQUID magnetometry using the average critical current density values at  $T = 4.2$  K of unirradiated samples of each type (cf. Subsection 4.1.1).  $C$ ,  $p$ , and  $B_{c2}^*$  were used as fit parameters, whereas the high-field exponent  $q$  was taken from the scaling computations which optimize  $p$  and  $q$  for all data sets in the temperature range from 4.2 to 15 K (cf. Subsection 4.1.4), since the magnetometry results do not contain sufficient high-field data at 4.2 K to obtain a reliable value for  $q$ . For the reasons given in Subsection 4.2.4 the parameters  $C$ ,  $p$ , and  $B_{c2}^*$  were fit to the 4.2 K magnetometry data instead of using the scaling parameters obtained by minimizing the global error throughout the entire temperature range.

The comparisons are depicted in Figure 3.27 (RRP wire), Figure 3.28 (PIT wire), Fig-

ure 3.29 (TiR wire), Figure 3.30 (BIN wire), and Figure 3.31 (P07 wire). The magnetometry data points in the plots were calculated by multiplying the  $J_c^{(\text{mag})}$  values with the cross section of the A-15 phase in the respective wire, which is given by

$$A_{\text{A-15}} = N\pi(\rho_o^2 - \rho_i^2), \quad (3.42)$$

where  $N$  denotes the number of sub-elements in the wire,  $\rho_o$  their outer radius, and  $\rho_i$  their inner radius. The  $I_c^{(\text{mag})}(B)$  curves were calculated using the parameters obtained from the volume pinning force fit function (3.41):

$$I_c^{(\text{mag})}(B) = A_{\text{A-15}} \frac{C}{B} \left( \frac{B}{B_{c2}^*} \right)^p \left( 1 - \frac{B}{B_{c2}^*} \right)^q \quad (3.43)$$

The transport critical current values shown in the plots were obtained as described in Subsection 3.4.4 in case of the RRP, the TiR, and the P07 wire types, whereas the transport data on the PIT and the BIN wires were provided by *CERN*. The  $I_c^{(\text{mag})}$  curves exhibit certain deviations relative to the  $I_c$  values obtained from transport measurements, as can be expected owing to the simplifying assumptions in the critical current density evaluation model (cf. Subsection 3.4.1) and the uncertainties in the sub-element radii obtained from SEM images (cf. Subsection 2.1.1). An empirical correction factor  $K$ , which relates magnetometry data to transport results, was calculated for each sample type by fitting the function  $K I_c^{(\text{mag})}(B)$  to the transport results using  $K$  as the only adjustable parameter. These correction factors as well as the maximum deviations between the extrapolated critical current obtained from magnetometry and the transport critical current values are given in Table 3.3 for each sample type. A comparison of magnetization and transport data obtained from irradiated samples is presented in Subsection 4.2.1.

Wire type	$K$	Remaining maximum deviations			
RRP	1.167	+0.5%	(13.4 T)	−0.6%	(15.3 T)
PIT	1.062	+0.8%	(8.6 T)	−1.6%	(12.3 T)
TiR	1.059	+3.4%	(10.5 T)	−7.2%	(15.2 T)
BIN	1.076	+5.0%	(12.2 T)	−1.7%	(9.5 T)
P07	1.118	+3.3%	(8.5 T)	−10.0%	(15.2 T)

**Table 3.3.:** Correction factors for critical current values obtained from magnetometry, and remaining maximum deviations between magnetometry and transport results after the correction.

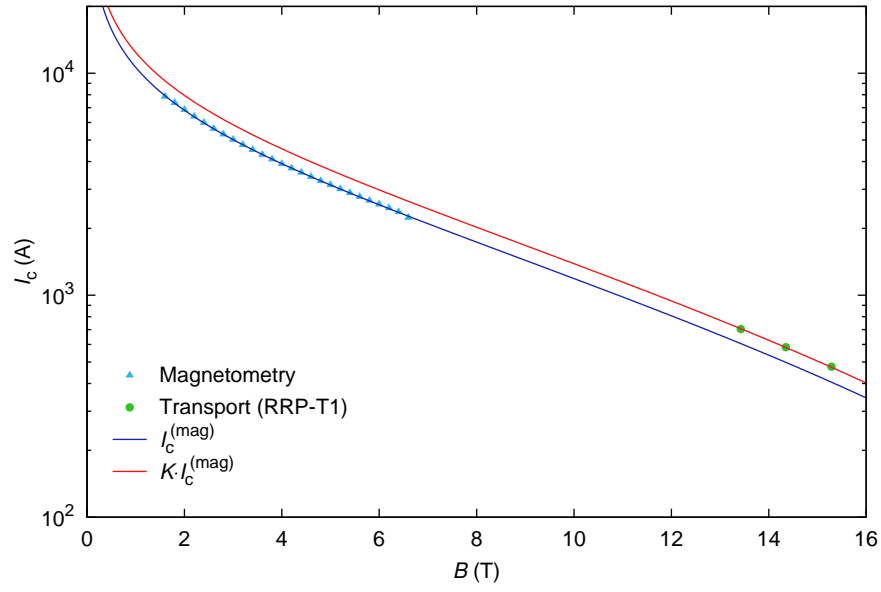


**Figure 3.27.:** Comparison of magnetometry results and transport measurements for the RRP wire.

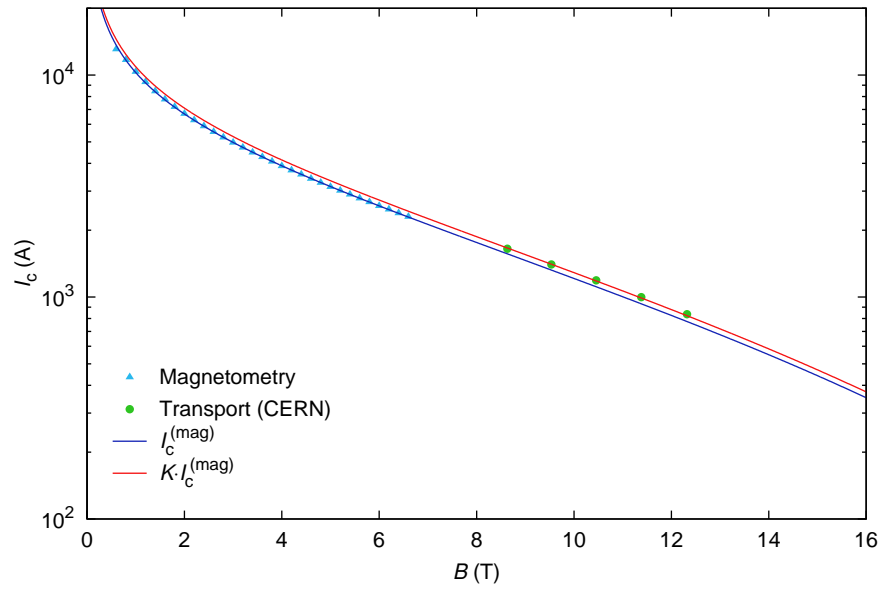


**Figure 3.28.:** Comparison of magnetometry results and transport measurements for the PIT wire.

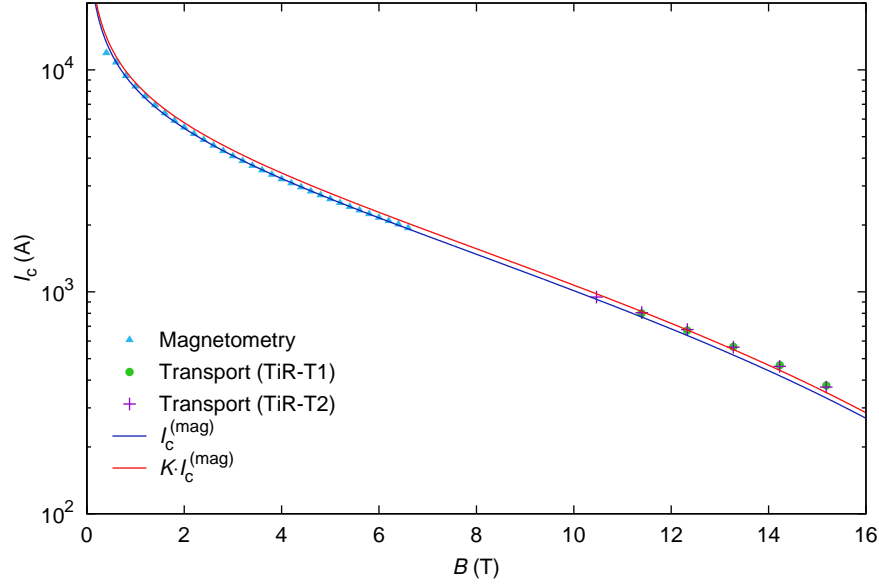


**Figure 3.29.:** Comparison of magnetometry results and transport measurements for the TiR wire.

### 3.4.7. $T_c$ from AC susceptibility

In Subsection 3.1.4 the method used for measuring the AC susceptibility of magnetization samples as a function of temperature is described. The resulting  $m'(T)$  and  $m''(T)$  data (in-phase and out-of-phase components of the measured magnetic moment) were used to obtain the critical temperature of each sample before irradiation and after each irradiation step. This task was automated by implementing an algorithm which performs the following operations:

- Shift the  $m'(T)$  data so that its maximum (normal state) value is zero.
- Normalize the data such that the maximum value of  $m'(T)$  is 1.
- Detect the peak in  $m''(T)$  whose position approximately corresponds to  $T_c$ .
- Determine the temperature range around this peak in which the transition occurs using a slope criterion.
- Compute a linear fit  $f_1(T)$  to the  $m'(T)$  data within this temperature range.
- Compute a linear fit  $f_2(T)$  to the  $m'(T)$  data for temperatures below  $T_c$ .
- Calculate the temperature values  $T_1$  and  $T_2$  at which  $f_1(T)$  intersects  $f_2(T)$  and the  $m' = 0$  line.

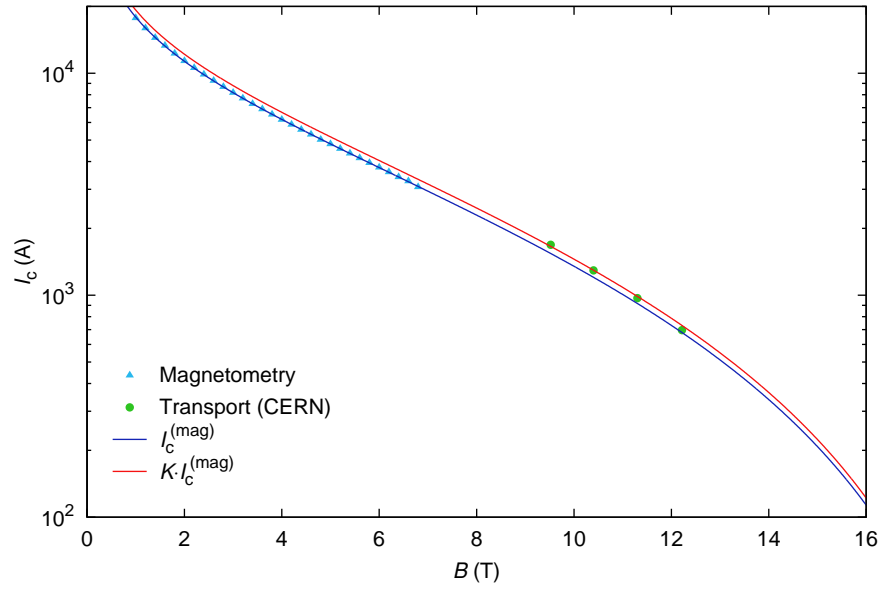


**Figure 3.30.:** Comparison of magnetometry results and transport measurements for the BIN wire.

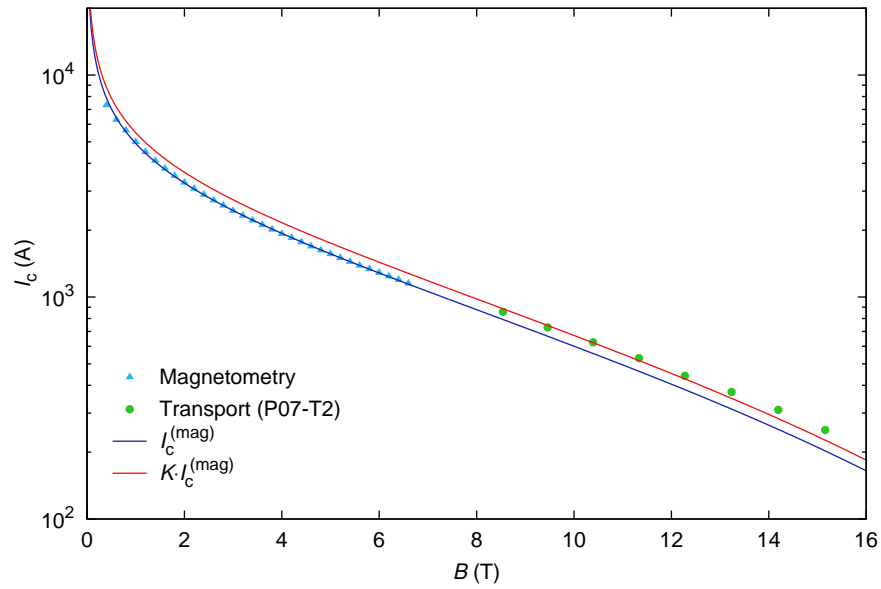


**Figure 3.31.:** Comparison of magnetometry results and transport measurements for the P07 wire.

The critical temperature was taken as the mid-point of the transition given by

$$T_c = \frac{T_2 - T_1}{2}, \quad (3.44)$$

and the transition width was defined as<sup>7</sup>

$$\Delta T_c = T_2 - T_1. \quad (3.45)$$

When evaluating measurements on samples produced by the powder-in-tube process (sample types PIT and P07), the two-stage transition which occurs due to the grain morphology of these wires must be considered (cf. Subsection 2.1.1 and Subsection 3.1.4). In this case the evaluation algorithm detects another peak in  $m''(T)$ , which corresponds to the transition of the large grains, about 0.7 K above that of the small grains. Since the latter dominate the transport properties of the wires, only the transition of the small grains was evaluated. For that purpose the intersection of  $f_1(T)$  with  $m' = C$  instead of  $m' = 0$  was calculated, where  $C$  is the value of  $m'(T)$  in the middle between the two peaks in  $m''(T)$ . The evaluation method is illustrated for both cases, single-stage and two-stage transitions, in Figure 3.32, for which the raw data shown in Subsection 3.1.4 were used.

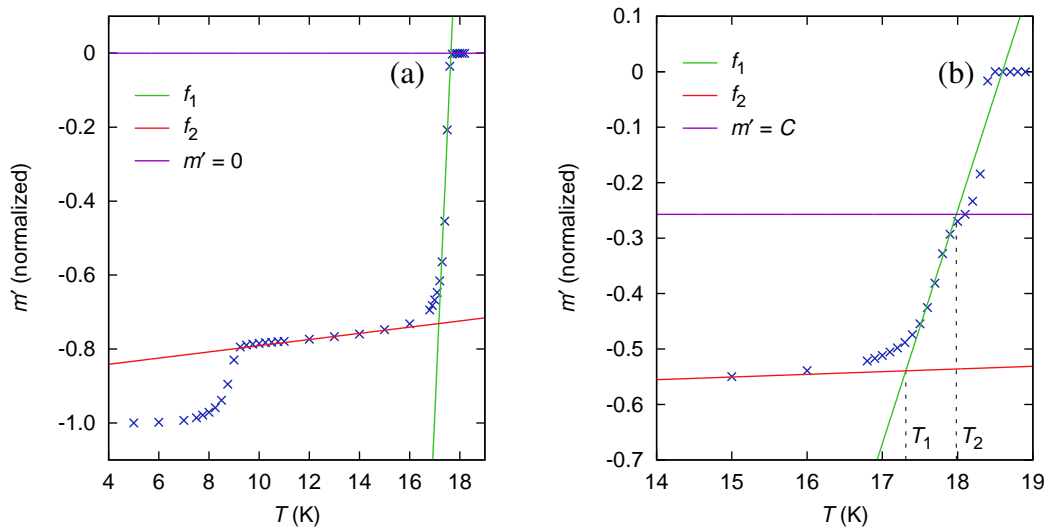


**Figure 3.32.:** Illustration of the  $T_c$  evaluation method. **(a)** The AC susceptibility data points of sample TiR-7 as well as the linear fits  $f_1(T)$  and  $f_2(T)$  are shown. **(b)** In powder-in-tube wire samples such as P07-1 the critical temperatures of the small grains is evaluated.

<sup>7</sup>The transition width strongly depends on the measurement method and how it is defined, which must be considered when  $\Delta T_c$  values reported by different authors are to be compared.



The evaluation procedure described above allows the assessment of the critical temperature with higher precision than the temperature resolution of 0.1 K used in the measurements. This is of particular importance when small changes of  $T_c$  due to irradiation within the low-fluence regime are to be detected. The critical temperatures of the five examined wire types in the unirradiated state are given in Subsection 4.1.2. Changes in  $T_c$  due to fast neutron irradiation are discussed in Subsection 4.2.2.

#### 3.4.8. $B_{c2}(T)$ from resistivity measurements

The upper critical field of several wire samples was determined by means of resistivity measurements in the temperature range where  $B_{c2}(T) < 15$  T, as described in Subsection 3.3.2. The resulting data are voltage vs. temperature curves recorded at different values of constant applied field.  $B_{c2}$  values were obtained from the data using a method similar to that applied in the  $T_c$  evaluation described in Subsection 3.4.7. As illustrated in Figure 3.33, linear fits were computed within the temperature range of the transition (function  $f_1(T)$ ) as well as below (function  $f_2(T)$ ) and above it (function  $f_3(T)$ ). The function  $f_2(T)$  is needed to compensate for offset voltages as well as transfer length problems, which can lead to deviations from the zero line. The intersection points of  $f_1(T)$  with  $f_2(T)$  and  $f_3(T)$  were calculated to obtain the temperatures  $T_1$  and  $T_2$  at which the transition starts and ends. The transition temperature at an applied field  $B_a$  was taken as the average of  $T_1$  and  $T_2$ , allowing the construction of the  $B_{c2}(T)$  curve using

$$B_{c2}\left(\frac{T_1 + T_2}{2}\right) = B_a. \quad (3.46)$$

The results of the upper critical field evaluation described above for each sample type before irradiation are given in Subsection 4.1.3. The irradiation induced changes in  $B_{c2}(T)$  are discussed in Subsection 4.2.3.

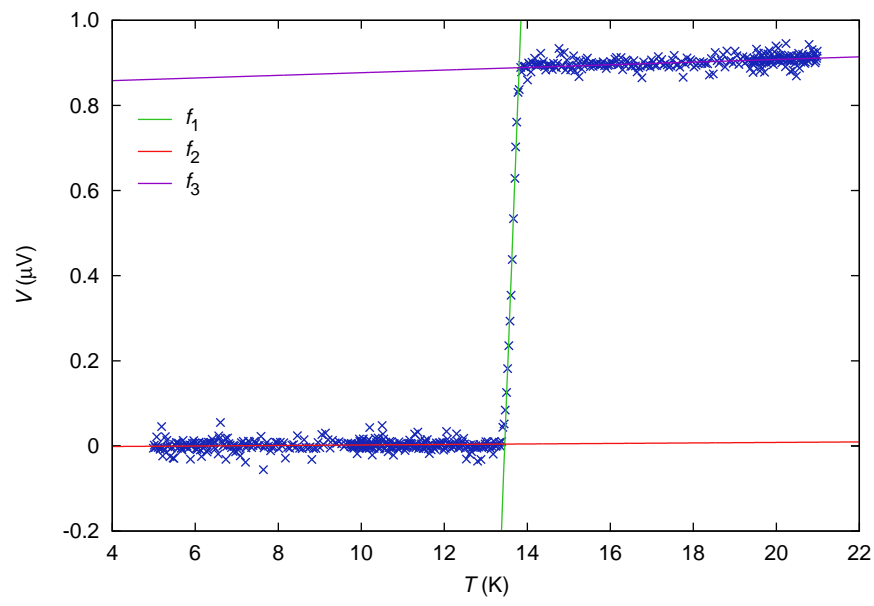


**Figure 3.33.:**  $B_{c2}$  evaluation of data obtained from sample P07-R1 at an applied field of 9 T.

## 4. Results and Discussion

The results obtained from the measurements and evaluation procedures described in Chapter 3 are analyzed and discussed in the following. The properties of unirradiated samples are discussed in Section 4.1, whereas the changes in these properties induced by fast neutron irradiation are the subject matter of Section 4.2. In Section 4.3 conclusions are presented based on the results discussed in this chapter.

### 4.1. Properties in the unirradiated state

In order to assess the effects of neutron irradiation induced defects on the properties of the examined wires, accurate measurements of these properties in the unirradiated state are required. For that purpose the critical current density and the critical temperature of several unirradiated short samples of each wire type were obtained by means of SQUID magnetometry (cf. Section 3.1), using the evaluation methods described in Subsection 3.4.5 and Subsection 3.4.7. The results of these measurements are discussed in Subsection 4.1.1 and Subsection 4.1.2. The upper critical field as a function of temperature was measured on one unirradiated sample of each wire type using the measurement procedure and the evaluation method described in Subsection 3.3.2 and Subsection 3.4.8, respectively. Results obtained from these measurements are given in Subsection 4.1.3. The volume pinning force scaling behavior of the unirradiated wires was analyzed based on the data presented in Subsection 4.1.1, and is discussed in Subsection 4.1.4.

#### 4.1.1. Critical current density

The plots in this sub-section depict the critical current density  $J_c$  of the five examined wire types as a function of magnetic field at different temperatures. The data were obtained

from SQUID magnetometry (cf. Section 3.1), using the evaluation procedure described in Subsection 3.4.5. In the plots average  $J_c$  values

$$\bar{J}_c = \frac{1}{N} \sum_{i=1}^N J_c^i \quad (4.1)$$

are shown, where  $N$  is the number of samples which contributed to the data point in question, and  $J_c^i$  is the  $J_c$  value obtained from the  $i$ -th sample. The error bars indicate the standard deviation  $\pm\sigma_{J_c}$  of each data point, which was calculated using

$$\sigma_{J_c} = \sqrt{\frac{1}{N} \sum_{i=1}^N (J_c^i - \bar{J}_c)^2}. \quad (4.2)$$

The results are shown in Figure 4.1 for the RRP wire (based on six samples), in Figure 4.2 for the PIT wire (based on five samples), in Figure 4.3 for the TiR wire (based on five samples), in Figure 4.4 for the BIN wire (based on four samples), and in Figure 4.5 for the P07 wire (based on four samples).<sup>1</sup> A comparison of the critical current densities of the five examined wire types is shown in Figure 4.6.

The evaluation of the critical current density from SQUID magnetometry data is only viable if results obtained from different samples of the same type are in good agreement. The relative standard deviations  $\sigma_{J_c}/\bar{J}_c$  of the average  $J_c$  values presented above are a measure for this agreement, and are shown in Figure 4.7 for all wire types at a temperature of 4.2 K. For the PIT and TiR samples the relative standard deviations are mostly between 3 and 4%, for the RRP and BIN samples around 2%, and for the P07 samples around 1%. Since the magnitude of  $\sigma_{J_c}/\bar{J}_c$  does not appear to correlate with the ratio of the number of standard sample transport and RSO measurements (the correction of the former could introduce an additional error; cf. Subsection 3.4.3) or with the sub-element geometry, it stands to reason that these relative standard deviations reflect the actual homogeneity of the magnetization along the respective wires. The small values of  $\sigma_{J_c}/\bar{J}_c$  indicate good homogeneity of the magnetization, which supports the concept of obtaining the critical current density from short wire samples.

---

<sup>1</sup>Some of the average  $J_c$  values are based on data obtained from fewer samples than stated above due to the exclusion of unreliable data points.

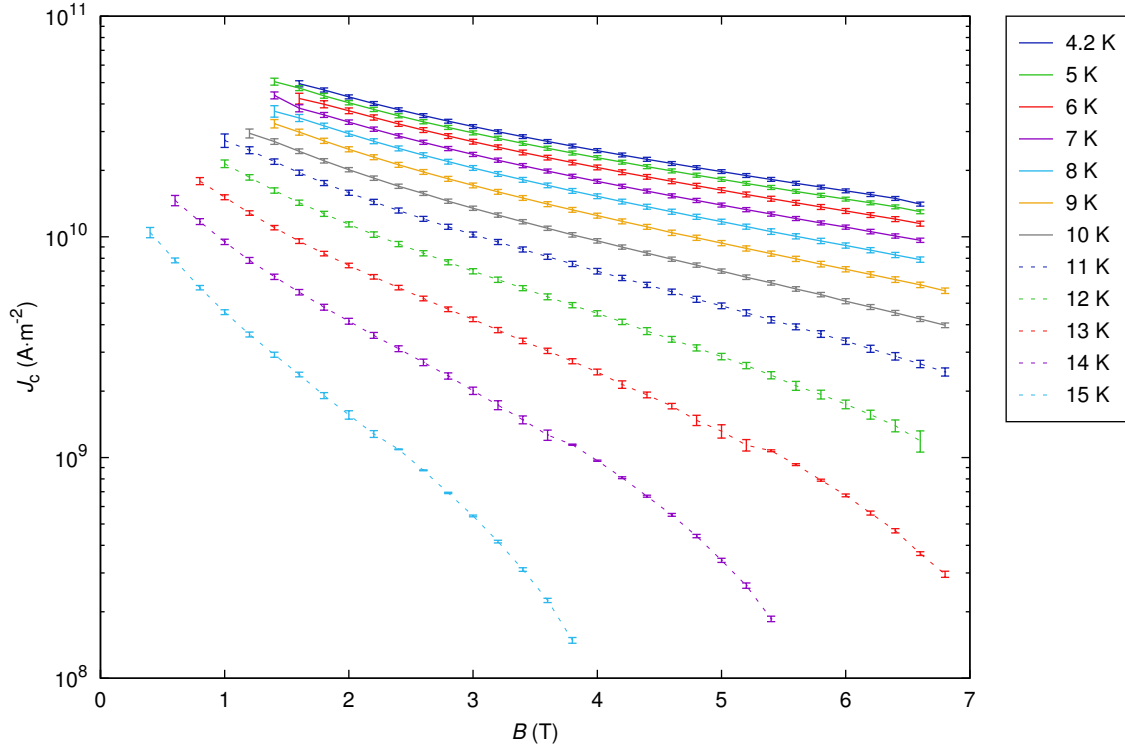


**Figure 4.1.:** Critical current density of RRP samples, obtained from SQUID magnetometry.

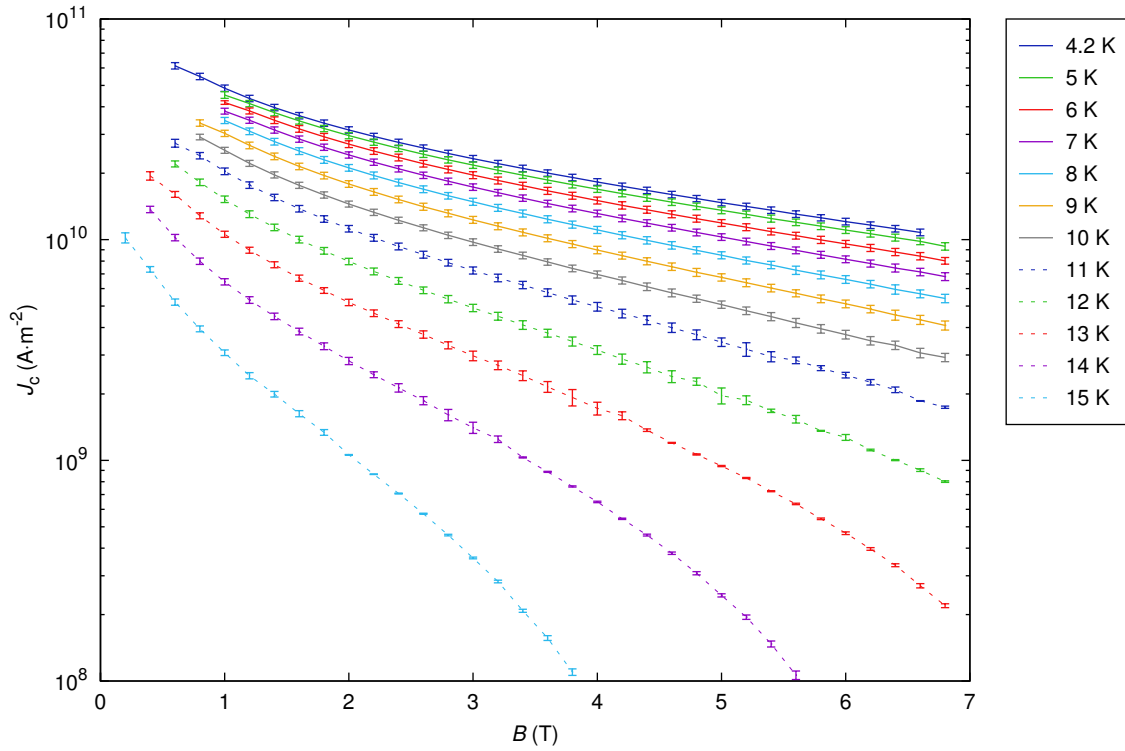


**Figure 4.2.:** Critical current density of PIT samples, obtained from SQUID magnetometry.

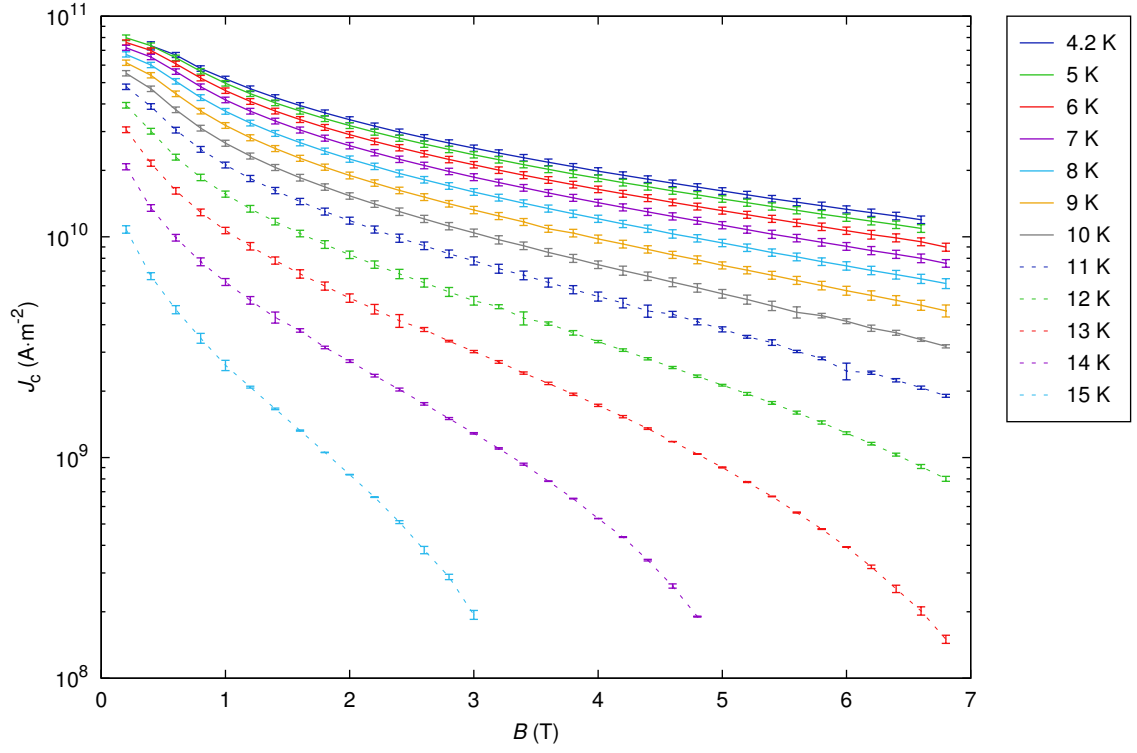


**Figure 4.3.:** Critical current density of TiR samples, obtained from SQUID magnetometry.

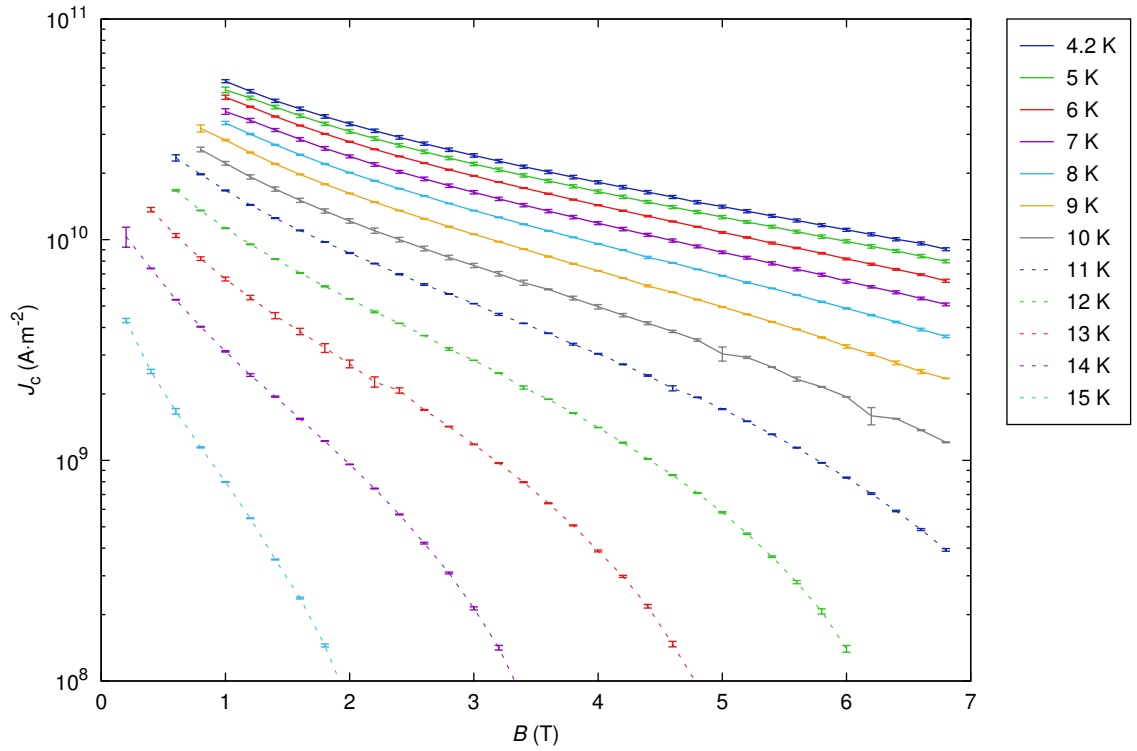


**Figure 4.4.:** Critical current density of BIN samples, obtained from SQUID magnetometry.

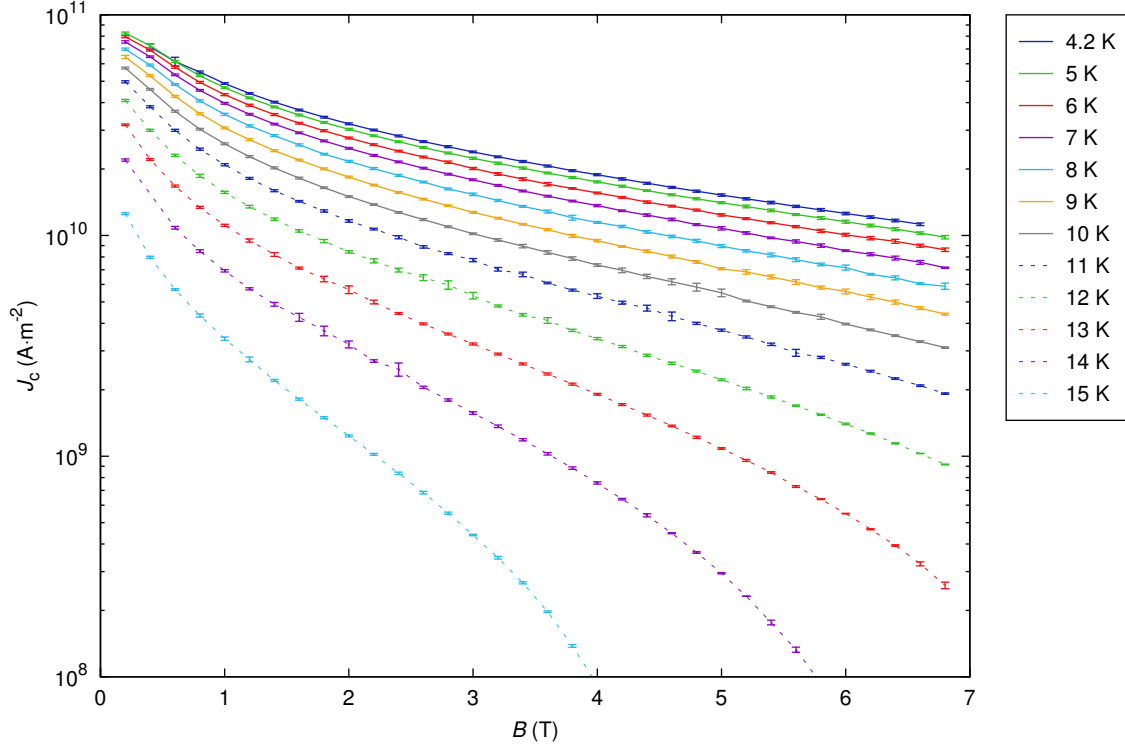


**Figure 4.5.:** Critical current density of P07 samples, obtained from SQUID magnetometry.

#### 4.1.2. Critical temperature

The critical temperature  $T_c$  of short wire samples as well as its transition width  $\Delta T_c$  was obtained by means of AC susceptibility measurements in a SQUID magnetometer, as described in Subsection 3.1.4 and Subsection 3.4.7. The average  $T_c$  and  $\Delta T_c$  values of the unirradiated samples of each examined wire type together with the number of samples on which the averages are based are given in Table 4.1. The critical temperatures and transition widths obtained from the upper critical field measurements described in Subsection 3.3.2 (the voltage-temperature curve recorded in zero applied field was used) are included for comparison. The agreement between the  $T_c$  values obtained from the two methods is excellent (less than 0.5% deviation) in case of the RRP, TiR, and BIN wires. Owing to the fact that the PIT and P07 wires were produced with the powder-in-tube process, the agreement is significantly worse (around 4%) in these wires. While the evaluation procedure used on the AC susceptibility data is designed to obtain the critical temperature of the small grains, resistivity measurements only “see” the large grains (cf. Subsection 2.1.1).

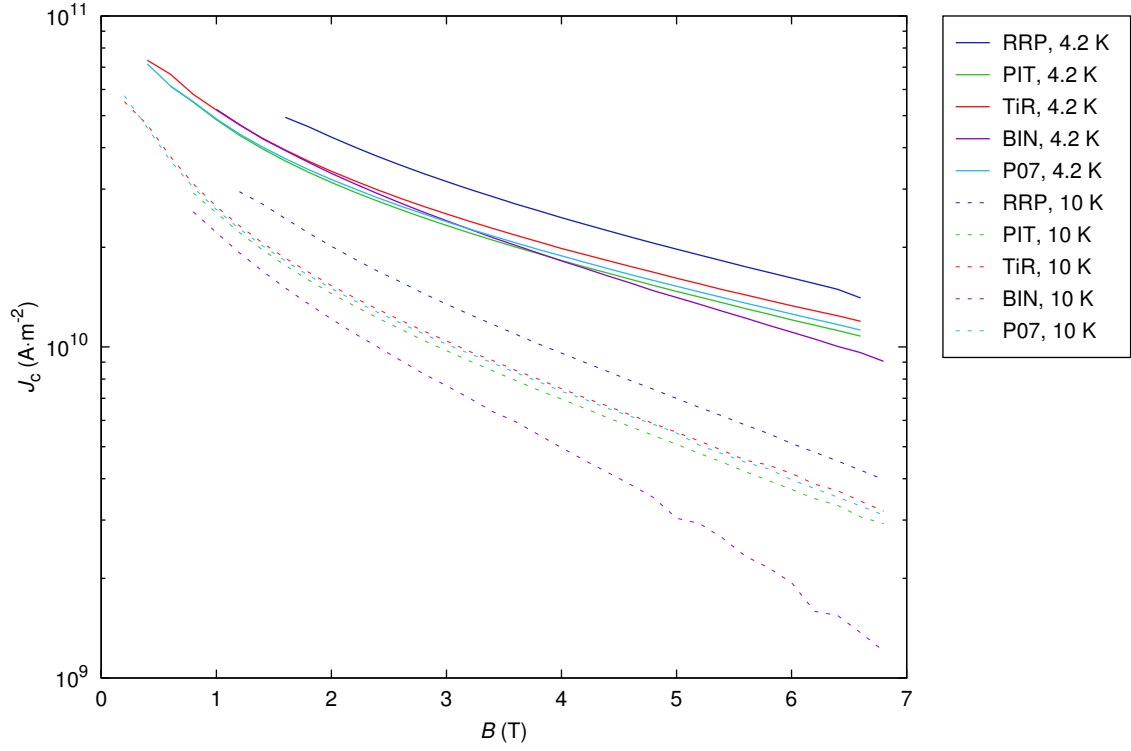


**Figure 4.6.:** Comparison of the critical current densities of the five examined wire types at 4.2 K and at 10 K.

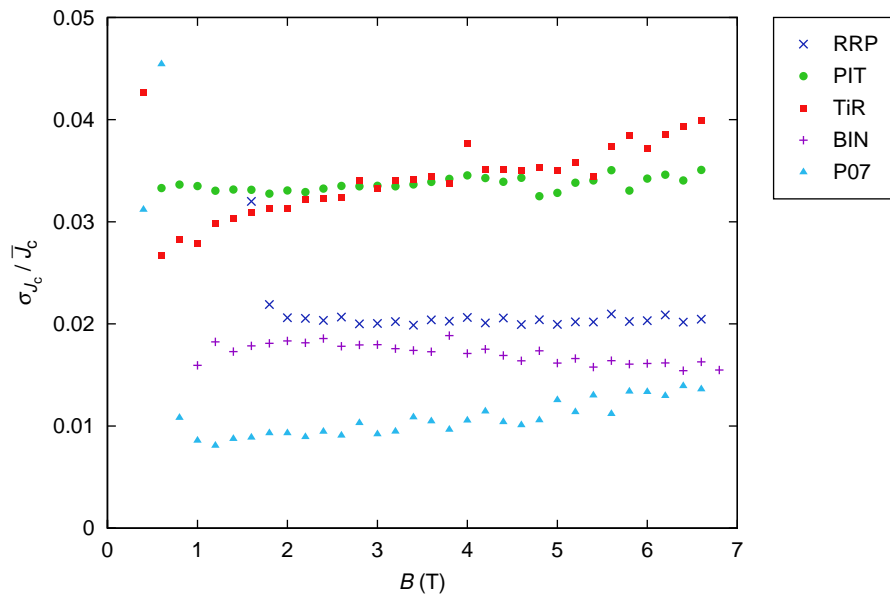


**Figure 4.7.:** Relative standard deviations of the above discussed average  $J_c$  values at  $T = 4.2$  K.



Wire type	AC susceptibility			Resistivity	
	$T_c$ (K)	$\Delta T_c$ (K)	Samples	$T_c$ (K)	$\Delta T_c$ (K)
RRP	17.85	0.39	3	17.87	0.16
PIT	17.64	0.65	3	18.26	0.08
TiR	17.43	0.53	5	17.37	0.10
BIN	17.17	0.54	3	17.11	0.14
P07	17.66	0.58	4	18.28	0.19

**Table 4.1.:** Critical temperatures and transition widths of unirradiated samples obtained from SQUID magnetometry and resistivity measurements.

The smaller values of the transition widths found in resistivity measurements can be explained by percolation: Even when a large fraction of the grains is in the normal state, the current can still find a path consisting entirely of grains which are still in the superconducting state. Magnetometry on the other hand measures the superconducting volume more directly, thus being more susceptible to the transition of low- $T_c$  grains, unless they are completely shielded by high- $T_c$  grains, which is fortunately not the case in the wires examined in this work (cf. Subsection 2.1.1). Therefore, and because the transition of the small grains in powder-in-tube wires cannot even be detected by means of resistivity measurements, the  $T_c$  and  $\Delta T_c$  data obtained from SQUID magnetometry are more reliable than the resistivity based results.

### 4.1.3. Upper critical field

The temperature dependence of the upper critical field  $B_{c2}$  of each wire type in its unirradiated state was obtained from resistivity measurements, as described in Subsection 3.3.2 and Subsection 3.4.8. Since the applied field in these measurements was limited to 15 T, only the high-temperature part ( $T \gtrsim T_c/2$ ) of the  $B_{c2}(T)$  curves could be measured. Within this temperature range the  $B_{c2}(T)$  data are virtually linear, hence not allowing an extrapolation to low temperatures without assuming a certain functional dependence. Since Nb<sub>3</sub>Sn multifilamentary wires can be regarded as superconductors in the dirty limit, the zero-field value of the upper critical field can be calculated using the WHH<sup>2</sup> expression (1.11) dis-

<sup>2</sup>After Werthamer, Helfand, and Hohenberg; cf. Subsection 1.2.1 as well as [61], [62], and [140].

cussed in Subsection 1.2.1:

$$B_{c2}(0) = 0.693 T_c \left( -\frac{dB_{c2}}{dT} \right)_{T=T_c}, \quad (4.3)$$

A linear fit to the measurement results was computed for all data points at  $T > T_c/2$ , excluding the zero-field point to reduce the influence of inhomogeneities (e.g. large grains with higher  $T_c$  values in powder-in-tube wires; cf. Subsection 2.1.1 and Subsection 3.4.7). The zero-temperature upper critical field, the slope of  $B_{c2}$  at  $T_c$ , and the critical temperature obtained from this fit procedure are listed in Table 4.2 under “WHH slope fit”. In the WHH paper [62] the function

$$h^*(t) = \frac{B_{c2}(t)}{\left( -\frac{dB_{c2}}{dt} \right)_{t=1}}, \quad (4.4)$$

which describes the dependence of the upper critical field on the reduced temperature, was computed numerically for various degrees of purity. Its value at  $t = 0$  gives the prefactor of 0.693 in (4.3). It was found by the present author that the dirty limit  $h^*(t)$  curve can be approximated quite accurately by the function

$$h_{\text{fit}}^*(t) = 1 - t - C_1 (1 - t)^2 - C_2 (1 - t)^4, \quad (4.5)$$

with  $C_1 = 0.153$  and  $C_2 = 0.152$ , as determined by fitting. This function is shown in Figure 4.8 together with data points taken from [62]. Using (4.4), (4.3), and the linearity of the data at  $T > T_c/2$ , the temperature dependence of the upper critical field can be expressed by

$$\begin{aligned} B_{c2}(T) &= -h^*(t) \left( \frac{dB_{c2}}{dT} \frac{dT}{dt} \right)_{T>T_c/2} = -h^*(T/T_c) T_c \left( \frac{dB_{c2}}{dT} \right)_{T>T_c/2} \\ &= B_{c2}(0) \frac{h^*(T/T_c)}{h^*(0)}. \end{aligned} \quad (4.6)$$

According to (4.6) it should be possible to obtain  $B_{c2}(T)$  at arbitrary temperatures using the approximation to  $h^*(t)$  defined in (4.5), and the values of  $B_{c2}(0)$  and  $T_c$  obtained from the above-mentioned linear fit. It was found, however, that better agreement with the measurement results can be obtained by using the latter two quantities as fit parameters, and fitting the function

$$B_{c2}(T) = \frac{B_{c2}(0)}{0.693} h_{\text{fit}}^*(T/T_c) \quad (4.7)$$

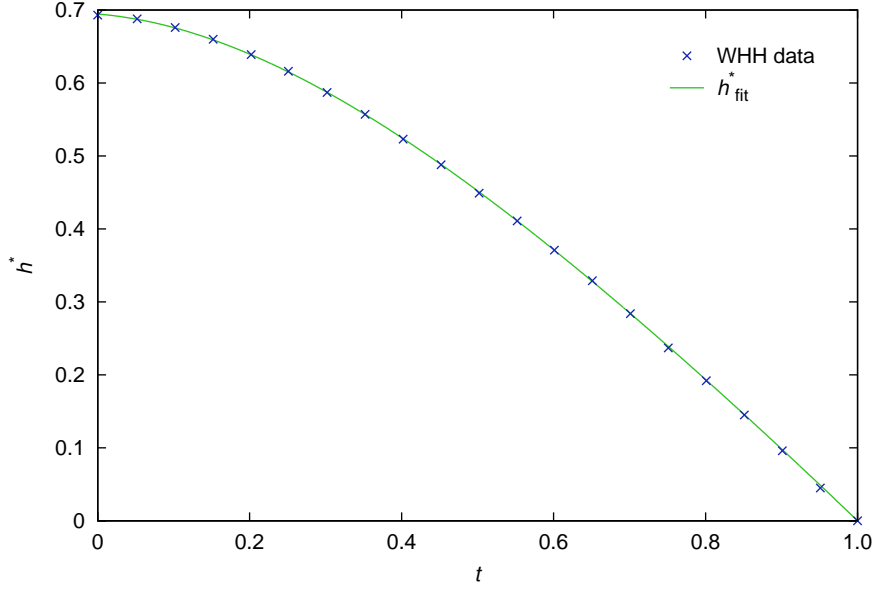


**Figure 4.8.:** Comparison of expression (4.5) to the theoretical dirty limit values of  $h^*(t)$ , taken from the WHH paper [62].

to the data, including all points. The reason for this is a deviation between the actual slope of  $B_{c2}(T)$  and the theoretical dirty limit curve. The thus obtained values of  $B_{c2}(0)$  and  $T_c$  are listed in Table 4.2 under “Global fit”. Due to the better agreement with the measurements, these  $B_{c2}(0)$  values are probably more accurate than those obtained from (4.3), assuming that Pauli paramagnetic limiting can be neglected, as indicated by the results discussed in Subsection 1.2.1. Figure 4.9 shows the measured  $B_{c2}(T)$  data as well as the fits which can be used to extrapolate to temperatures outside of the measurement range.

The expression

$$B_{c2}(T) = B_{c2}(0) \left( 1 - \left( \frac{T}{T_c^*} \right)^\nu \right) \quad (4.8)$$

is commonly used in literature to describe the temperature dependence of the upper critical field [36]. In (4.8)  $T_c^*$  is an effective critical temperature, and the exponent  $\nu$  is usually reported to have a value around 1.5, as mentioned in connection with scaling behavior in Subsection 1.2.2. Using the  $B_{c2}(0)$  values obtained from (4.3) (fourth column in Table 4.2), values between 1.578 and 1.661 were obtained for the parameter  $\nu$  by fitting (4.8) to the  $B_{c2}(T)$  data. These  $\nu$  values are in general agreement with those reported in literature, but the deviations between fits and data are larger than they are when using (4.7).

Wire type	WHH slope fit			Global fit	
	$(dB_{c2}/dT)_{T=T_c}$ (T/K)	$T_c$ (K)	$B_{c2}(0)$ (T)	$T_c$ (K)	$B_{c2}(0)$ (T)
RRP	-2.16	17.75	26.57	17.73	28.18
PIT	-2.11	18.00	26.32	18.04	27.72
TiR	-2.35	17.28	28.08	17.26	29.72
BIN	-1.85	16.87	21.67	16.86	23.34
P07	-2.10	17.95	26.09	18.01	27.40

**Table 4.2.:** Parameters obtained from the upper critical field measurements on unirradiated samples using the WHH method.

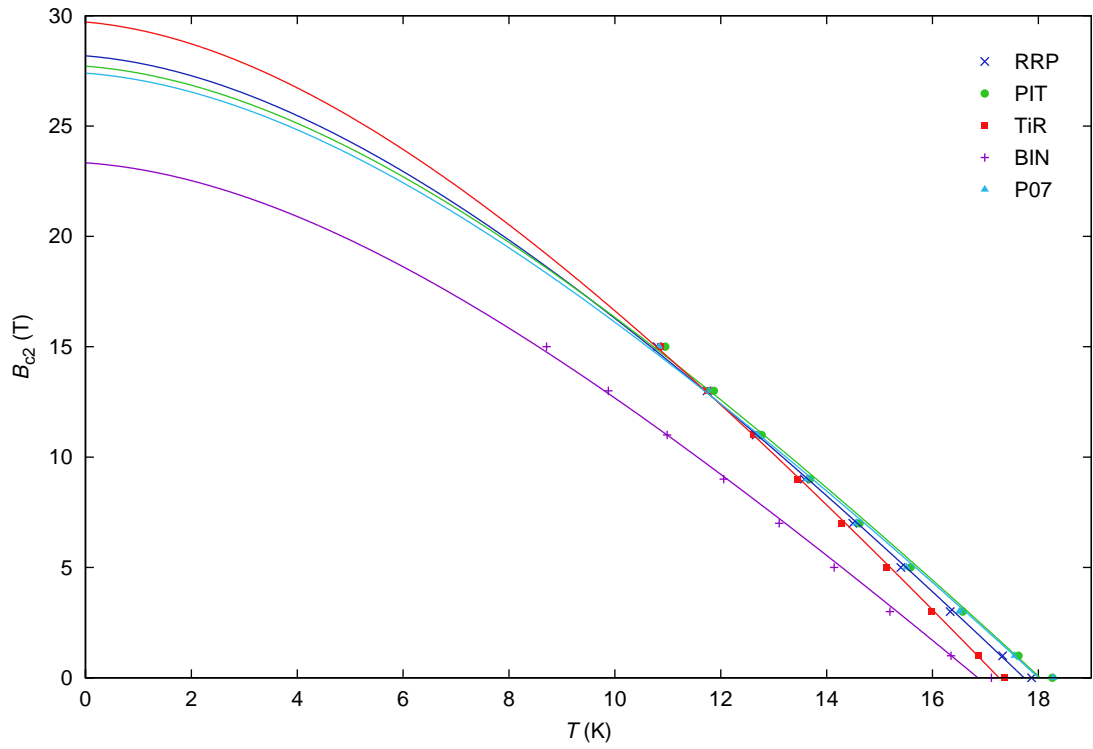


**Figure 4.9.:** Upper critical field values obtained from resistivity measurements on unirradiated wire samples and extrapolations to low temperatures.

#### 4.1.4. Scaling behavior

As discussed in Subsection 1.2.2, Nb<sub>3</sub>Sn is among the materials which exhibit pinning force scaling behavior, i.e. plotting the normalized volume pinning force  $F_p/F_p^{(\max)}$  versus the reduced field  $b = B/B_{c2}^*$  is supposed to yield the same curve, independent of the temperature at which the data were obtained. This curve is the so-called pinning force function  $f(b)$ , which is often expressed in the simple form

$$f(b) = C b^p (1 - b)^q, \quad (4.9)$$

with the material dependent low- and high-field exponents  $p$  and  $q$ . The prefactor  $C$  normalizes the maximum of the function to unity. If a material exhibits scalability, and  $f(b)$  as well as the temperature dependences of the pinning force maximum  $F_p^{(\max)}$  and the scaling field  $B_{c2}^*$  are known,  $F_p$  and hence  $J_c$  can be calculated for arbitrary values of temperature and magnetic field.

The scaling behavior of the five wire types examined in this work was analyzed using the critical current density data obtained from SQUID magnetometry (cf. Section 3.1 and Subsection 3.4.5). The scaling parameters of the unirradiated wires were obtained based on the averaged  $J_c$  data presented in Subsection 4.1.1, using a software program designed for that purpose, which accomplishes the following tasks:

- Obtain  $F_p(B) = J_c(B) B$  from the magnetometry results for all temperatures at which the measurements were performed.
- Find the peak in  $F_p(B)$ , using extrapolation if necessary.
- Normalize the volume pinning force to its peak value.
- Iterate  $p$  and  $q$  to find the optimum scaling exponents.
- Fit (4.9) to the data using  $B_{c2}^*$  as an adjustable parameter to obtain the scaling field at each available temperature. The values of  $p$  and  $q$  are fixed (previous step), thus determining the value of  $C$ .
- Assess the quality of the fits by computing the sum of the deviations between each data point at a given temperature and  $f(b)$ . The global error for all data sets is then calculated by summing up the values obtained at each available temperature.
- Continue to iterate  $p$  and  $q$  until the minimum in the global error is found.

The thus obtained pinning force functions  $f(b)$  of the unirradiated samples are depicted together with the normalized pinning force data obtained from magnetometry in Figure 4.10

(RRP wire), Figure 4.11 (PIT wire), Figure 4.12 (TiR wire), Figure 4.13 (BIN wire), and Figure 4.14 (P07 wire). A comparison of the computed scaling field  $B_{c2}^*$  and the upper critical field  $B_{c2}$  obtained from resistivity measurements (cf. Subsection 3.3.2, Subsection 3.4.8, and Subsection 4.1.3) is also shown in the respective figures.

A striking feature of these plots is that the scaling field exceeds the upper critical field at low temperatures in most sample types. The exception is the BIN wire, in which the crossover between the two functions occurs only in the extrapolated part of the curves, where no actual data points exist. The physically unsound outcome of a scaling field which is higher than the upper critical field is the result of minimizing the global error throughout the entire temperature range while lacking high-field data at low temperatures. However, such an unphysical temperature dependence of the scaling field is necessary to make the reduced pinning force data coalesce into one curve, as shown by Figure 4.15 which illustrates that scaling fails when the upper critical field is used as scaling field. These results lead to the conclusion that for the RRP, PIT, TiR, and P07 wire types scaling behavior of the data obtained from SQUID magnetometry can be “bought” at the price of a physically unsound scaling field at low temperatures. This implies that at low temperatures and fields well above 7 T (the upper limit of the *Quantum Design MPMS XL* SQUID magnetometer used in this work) the scaling parameters obtained from the above described algorithm are meaningless for the wires containing additives, and that  $J_c$  extrapolations to low temperatures and high fields based on these scaling parameters are bound to fail.

The problem with the unphysical scaling field could be remedied to some degree by including the results of transport measurements at applied fields of up to 15 T into the scaling calculations. However, these data are only available at one temperature (4.2 K), and the question remains of how to mix a few transport measurement data points with hundreds of magnetometry data points in a statistically justified way. Based on these considerations it was decided to perform the scaling computations presented in this work based on magnetometry data only. The scaling exponents  $p$  and  $q$ , the position of the maximum in  $f(b)$  given by

$$b_{\max} = \frac{p}{p+q}, \quad (4.10)$$

as well as the extrapolated zero-temperature value of the scaling field and its slope are summarized in Table 4.3 for all wire types in the unirradiated state. The pinning force data obtained from magnetometry generally exhibit good agreement with the simple scaling

law (4.9), provided that one is willing to accept unreasonably high scaling field values at low temperatures. Some deviations which appear to be systematic can be seen in the high-temperature parts of the curves, as can be expected owing to inhomogeneities [36]. The best agreement between data and fit was found in the binary wire, which also happens to exhibit the most ideal grain boundary pinning (scaling exponents closest to  $p = 1/2$ ,  $q = 2$ ) of all examined wire types. As pointed out by Flükiger, deviations from these values, which naturally lead to failure of the Kramer extrapolation method (cf. Subsection 1.2.2), may arise from the presence of grains whose Sn content or geometry differs significantly from the average [49].

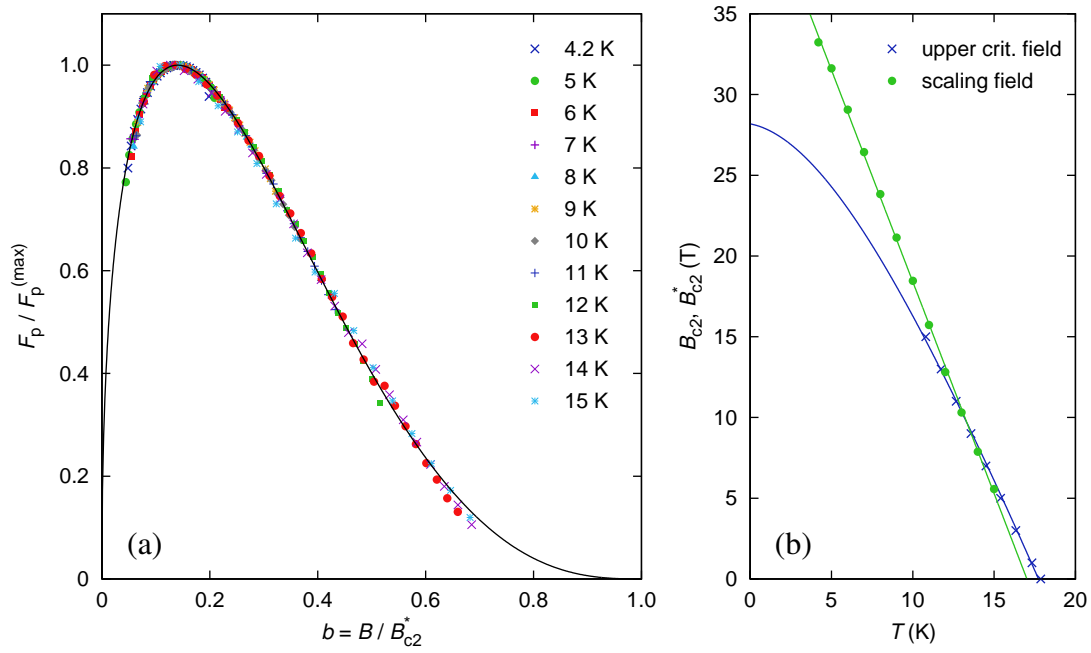


**Figure 4.10.:** Scaling behavior of unirradiated RRP samples. **(a)** Reduced pinning force at different temperatures and pinning force function. **(b)** Temperature dependences of the upper critical field and the scaling field.

The extrapolation of the available  $J_c(T, B)$  data into temperature and field ranges not accessible to measurements requires knowledge of both the pinning force function  $f(b)$  and the temperature scaling function  $h(t)$ , as discussed in Subsection 1.2.2. The latter describes the temperature dependence of the maximum value of the volume pinning force, and can be cast in the general form

$$h(t) = (1 - t^2)^\mu (1 - t^\nu)^{\eta - \mu} \quad \text{with} \quad t = \frac{T}{T_c^*}, \quad (4.11)$$

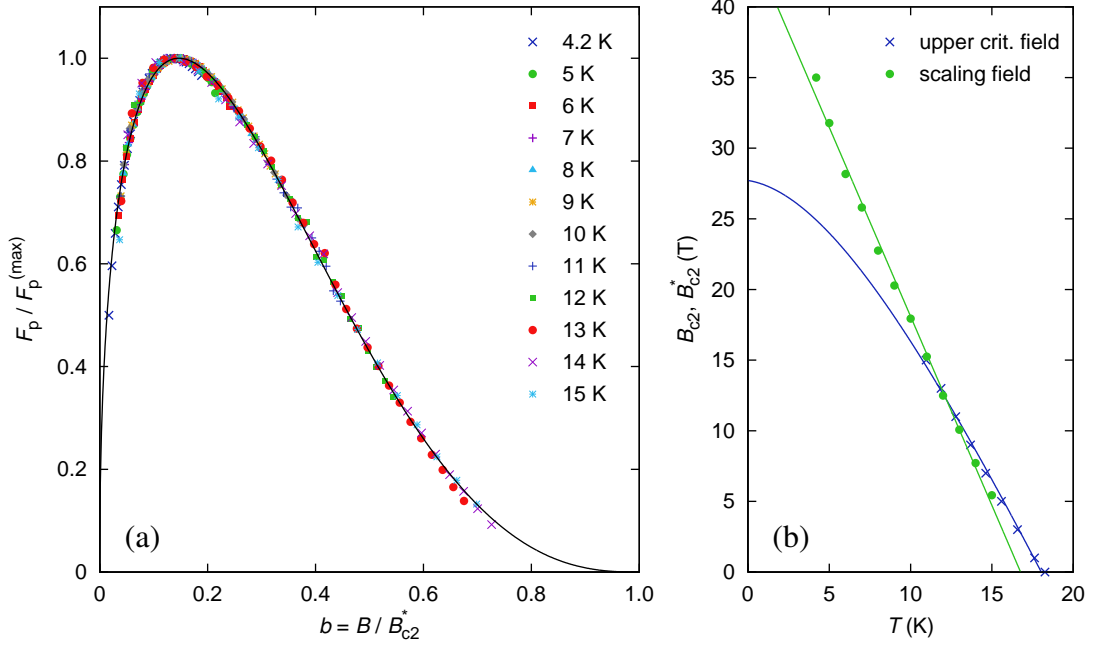


**Figure 4.11.:** Scaling behavior of unirradiated PIT samples. **(a)** Reduced pinning force at different temperatures and pinning force function. **(b)** Temperature dependences of the upper critical field and the scaling field.

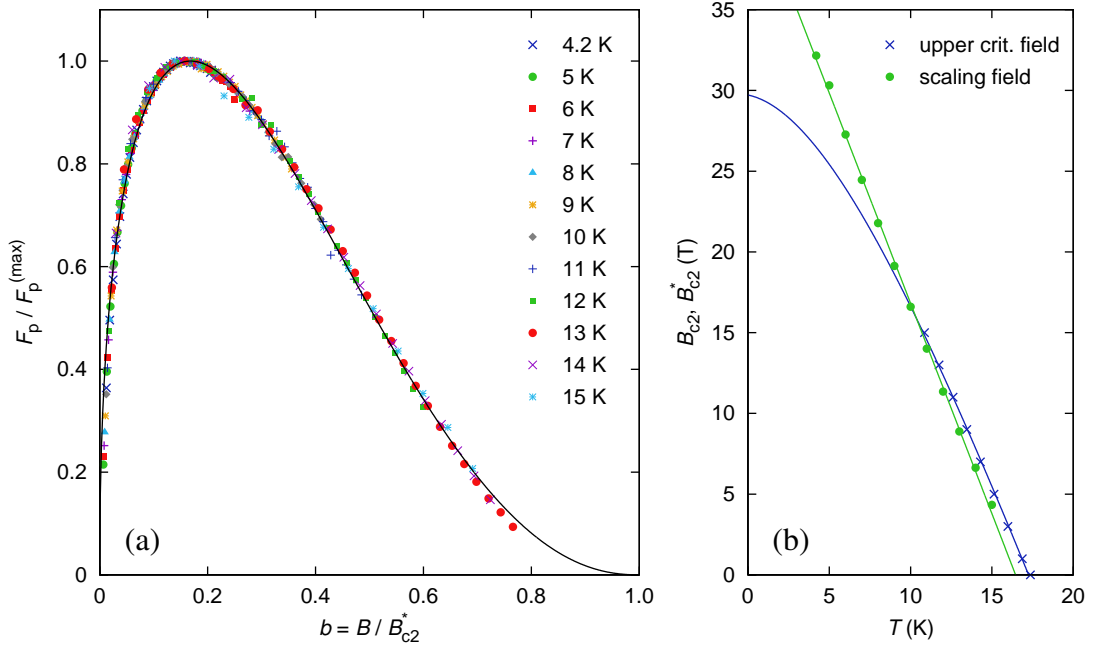


**Figure 4.12.:** Scaling behavior of unirradiated TiR samples. **(a)** Reduced pinning force at different temperatures and pinning force function. **(b)** Temperature dependences of the upper critical field and the scaling field.



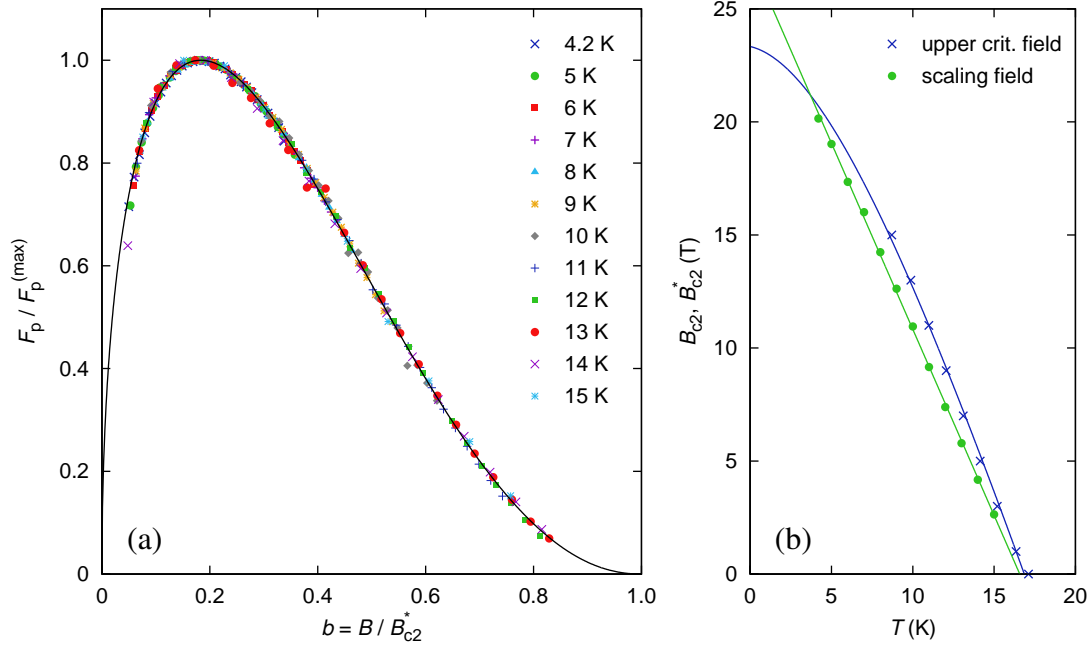


**Figure 4.13.:** Scaling behavior of unirradiated BIN samples. **(a)** Reduced pinning force at different temperatures and pinning force function. **(b)** Temperature dependences of the upper critical field and the scaling field.

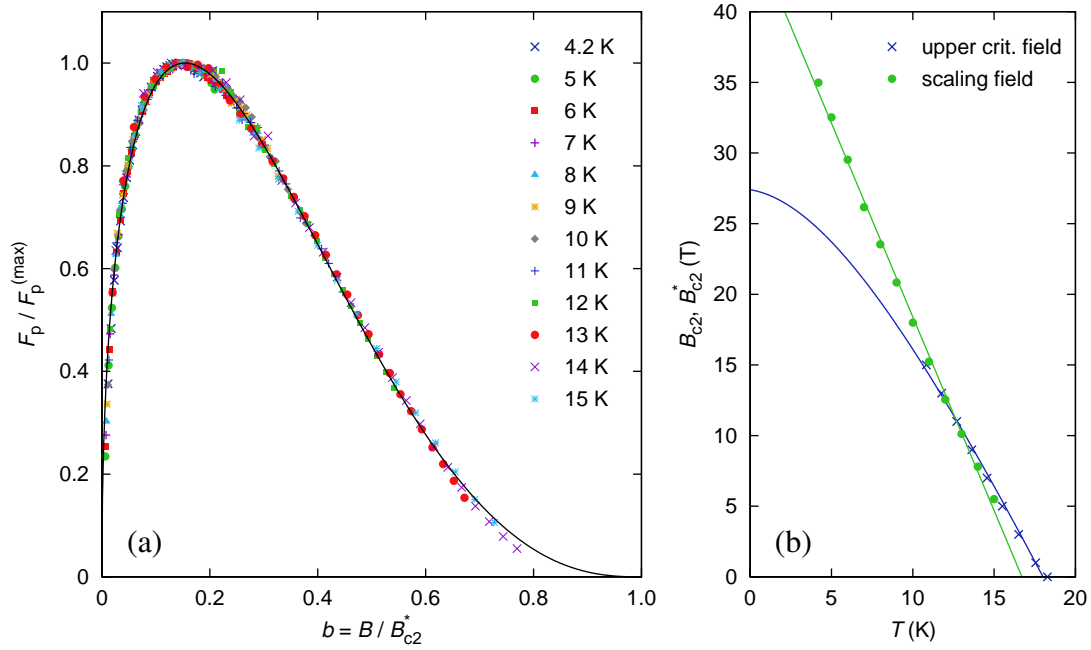


**Figure 4.14.:** Scaling behavior of unirradiated P07 samples. **(a)** Reduced pinning force at different temperatures and pinning force function. **(b)** Temperature dependences of the upper critical field and the scaling field.

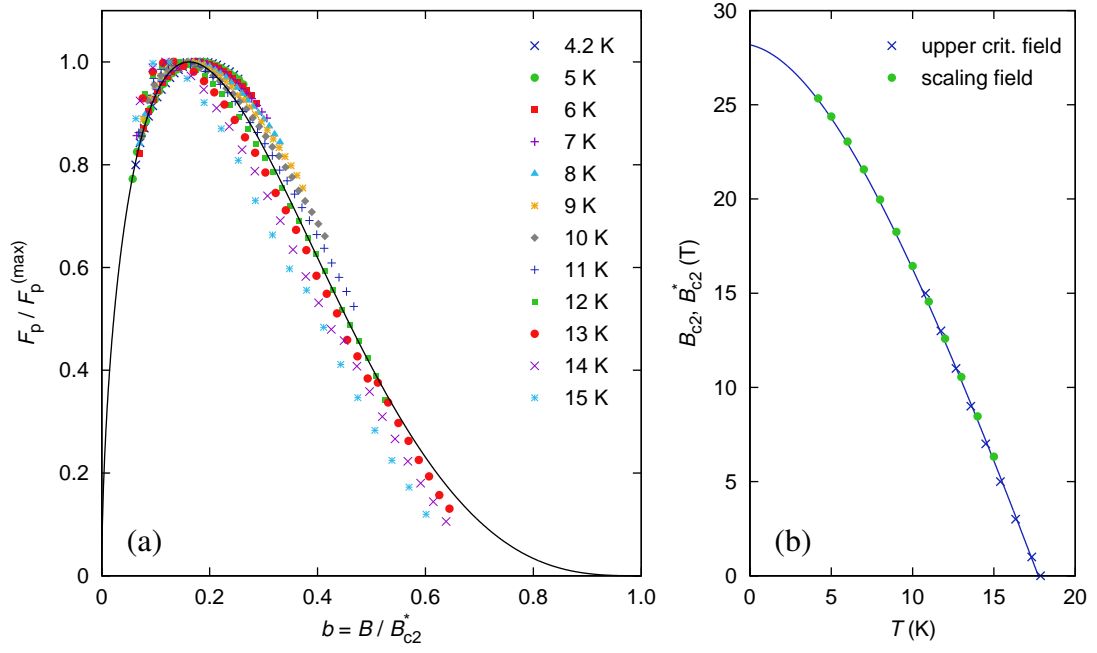


**Figure 4.15.:** Failure of scaling when the upper critical field is used as scaling field, illustrated with data obtained from unirradiated RRP samples. **(a)** Reduced pinning force at different temperatures and pinning force function. **(b)** Temperature dependence of  $B_{c2}^*(T) = B_{c2}(T)$ .

Wire type	$p$	$q$	$b_{\max}$	$B_{c2}^*(0)$ (T)	$dB_{c2}^*/dT$ (T/K)
RRP	0.448	2.738	0.141	44.64	-2.62
PIT	0.451	2.619	0.147	44.85	-2.68
TiR	0.458	2.262	0.168	42.87	-2.61
BIN	0.485	2.160	0.183	27.29	-1.65
P07	0.465	2.558	0.154	45.82	-2.74

**Table 4.3.:** Pinning force scaling parameters of the unirradiated wires.

where  $T_c^*$  is an effective scaling temperature. The optimum values of the exponents  $\mu$ ,  $\nu$ , and  $\eta$  have to be determined using a fit procedure with the restriction that  $\mu$  can only take the values 0, 1, or 2. Since  $h(0) = 1$  is independent of the scaling parameters, no additional normalization constant is required, and the maximum volume pinning force at a given temperature is

$$F_p^{(\max)}(T) = F_p^{(0)} h\left(\frac{T}{T_c^*}\right), \quad (4.12)$$

where  $F_p^{(0)}$  is the zero-temperature maximum volume pinning force. The temperature scaling parameters were evaluated using a software code which performs the following operations:

- Use the peak values  $F_p^{(\max)}$  computed in the pinning force scaling analysis based on SQUID magnetometry data measured in the temperature range from 4.2 to 15 K to obtain  $F_p^{(\max)}(T)$ .
- Fit expression (4.12) to the  $F_p^{(\max)}(T)$  data.  $F_p^{(0)}$  is always used as an adjustable parameter, whereas  $\mu$ ,  $\nu$ ,  $\eta$ , and  $T_c^*$  can be fixed.
- Calculate the sum of the deviations between each data point and the fit function to assess the quality of the fit.

An important outcome of these temperature scaling calculations is the fact that the critical temperature obtained from AC susceptibility measurements (cf. Subsection 3.1.4, Subsection 3.4.7, and Subsection 4.1.2) can be used as scaling temperature ( $T_c^* = T_c$ ) with very good agreement between the experimental data and the fit. Furthermore, it was found that the best choice for the exponent  $\mu$  is 0, although choosing  $\mu = 1$  or  $\mu = 2$  increases the fit deviation only slightly. Consequently, expression (4.11) can be simplified to

$$h(t) = (1 - t^\nu)^\eta \quad \text{with} \quad t = \frac{T}{T_c}. \quad (4.13)$$

A typical result of the above described fit procedure, using data obtained from sample PIT-2 in its unirradiated state, is shown in Figure 4.16. The scaling parameters determined by fixing  $T_c^* = T_c$  and  $\mu = 0$ , i.e. only using  $F_p^{(0)}$ ,  $\nu$ , and  $\eta$  as adjustable parameters, are given in Table 4.4. Note that the  $T_c$  values are slightly different from those specified in Subsection 4.1.2, which were calculated by averaging over the results of AC susceptibility measurements on unirradiated samples. The reason for this is that for the sake of consistency with the scaling analysis of irradiated samples (cf. Subsection 4.2.4) the  $T_c$  values in

Table 4.4 were calculated using an expression which describes the fluence dependence of the critical temperature (cf. Subsection 4.2.2).

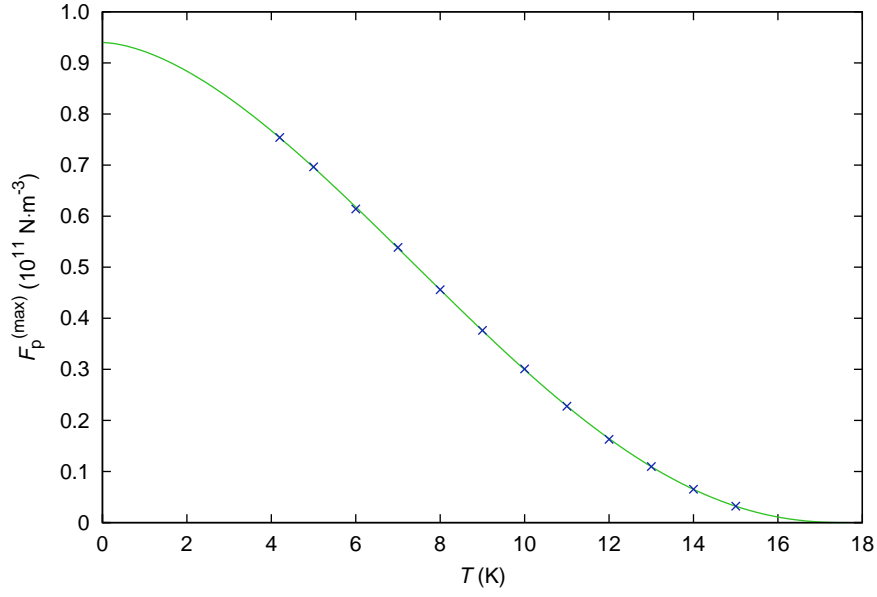


**Figure 4.16.:**  $F_p^{(max)}$  values and temperature scaling function of unirradiated sample PIT-2, computed with fixed  $T_c^* = T_c$  (from AC susceptibility measurements) and  $\mu = 0$ .

Wire type	$F_p^{(0)}$ (N/m <sup>3</sup> )	$T_c$ (K)	$\nu$	$\eta$
RRP	$1.20 \cdot 10^{11}$	17.85	1.782	2.430
PIT	$9.18 \cdot 10^{10}$	17.62	1.679	2.334
TiR	$1.00 \cdot 10^{11}$	17.43	1.716	2.389
BIN	$9.10 \cdot 10^{10}$	17.17	1.837	2.840
P07	$9.54 \cdot 10^{10}$	17.67	1.657	2.301

**Table 4.4.:** Temperature scaling parameters of the unirradiated wires.

It is noteworthy that the parameter  $\nu$  differs significantly from the value 1.52, which is often found in literature [36]. Using the expression  $(1 - t^\nu)$  to fit the temperature dependence of the upper critical field obtained from resistivity measurements yielded  $\nu \approx 1.6$  for all sample types (cf. Subsection 4.1.3), in rough agreement with  $\nu = 1.52$ . However, when the parameters  $\mu = 1$ ,  $\nu = 1.52$ , and  $\eta = 2$ , as suggested by Bottura and Bordini [17] were tested (with  $T_c^*$  being the only free parameter), the fit deviations were almost one order

of magnitude larger than they are with the parameters listed in Table 4.4. These results substantiate the fact that the wires examined in this work exhibit a large difference between the upper critical field (best fit with  $\nu \approx 1.6$ ) and the scaling field (best fit with  $\nu \approx 1.7$  to 1.8). Since the parameterization in [17] appears to be in good agreement with data obtained from Nb<sub>3</sub>Sn wires produced for *ITER*, it is possible that this behavior is limited to certain wire types.

### 4.2. Radiation induced changes

For reasons outlined in Section 1.1 the main focus of this work is the assessment of the effects of fast neutron irradiation on the properties of the five examined wire types. Sequential irradiation in the *TRIGA Mark-II* reactor at the *Atominstitut* (cf. Section 2.3) and SQUID magnetometry (cf. Section 3.1) after each irradiation step made this assessment possible. Changes in the critical current density, which was evaluated as described in Subsection 3.4.5, are discussed in Subsection 4.2.1. The effects of fast neutron irradiation on the critical temperature (cf. Subsection 3.4.7) and the upper critical field (cf. Subsection 3.4.8) are analyzed in Subsection 4.2.2 and Subsection 4.2.3. Changes in the pinning force scaling behavior – the most relevant result of this work in the opinion of the author – are discussed in Subsection 4.2.4.

#### 4.2.1. Critical current density

The critical current density  $J_c$  of short wire samples was obtained by means of SQUID magnetometry before irradiation and after each irradiation step as described in Subsection 3.4.5. The relative change  $J_c(\Phi_f t)/J_c(0)$  as a function of fast neutron fluence  $\Phi_f t$  at constant magnetic field  $B$  and temperature  $T$  was evaluated using an algorithm which carries out the following operations:

- Obtain  $J_c(B)$  from the critical current density evaluation files corresponding to the selected sample type and temperature, using only data from samples which were included in the irradiation program.
- Compute fits to the  $J_c(B)$  data within a range of  $\pm 1.5$  T around the selected evaluation field. This ensures that each of the  $J_c$  evaluation files can be used even if no data

point is available at the selected field, and it increases the reliability of the result by including several data points instead of relying on the quality of only one.

- Use the fit functions to obtain the value of the critical current density of all included samples after each irradiation step as well as in the unirradiated state.
- Calculate  $J_c(\Phi_f t)/J_c(0)$  for each sample and irradiation step.

As an example of the results obtained from this procedure the relative  $J_c$  increase in the RRP wire evaluated at temperatures of 4.2 K and 7 K as well as different field values is shown in Figure 4.17. Linear fits of the form  $f(\Phi_f t) = 1 + k\Phi_f t$  are also shown to guide the eye and to emphasize the temperature dependence of the  $J_c$  change. The slopes  $k$  are somewhat smaller at 7 K than they are at 4.2 K, which is to be expected owing to the fact that  $T_c$  decreases with increasing fluence, thus forcing  $J_c(\Phi_f t)/J_c(0)$  to take on values smaller than unity at high enough temperatures. The pronounced field dependence of the  $J_c$  change is consistent with the observations discussed in Subsection 1.2.3.

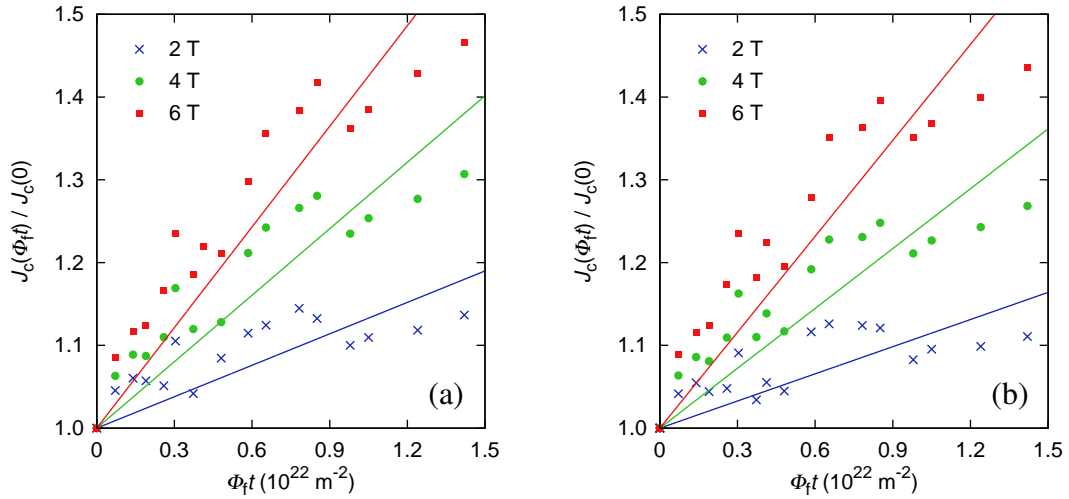


**Figure 4.17.:** Relative  $J_c$  increase as a function of fast neutron fluence evaluated at different field values. (a) RRP samples at 4.2 K. (b) RRP samples at 7 K.

Figure 4.17 was produced in such a way that the plots contain only one data point per fluence value. However, in some cases several samples of the same type were irradiated to the same fluence (cf. Section 2.3, in particular Table 2.6) in order to check the reproducibility of this irradiation study. The  $J_c(\Phi_f t)/J_c(0)$  evaluation results obtained from these samples at  $T = 4.2$  K and  $B = 6$  T are shown in Figure 4.18. The data exhibit considerable scatter, especially the three points obtained from TiR samples at a fast neutron fluence of  $1.7 \cdot 10^{21} \text{ m}^{-2}$ , which are scattered across a  $J_c$  increase range of eight percent points.

A difference in fluence between the samples cannot be the explanation for the deviation between the data points, since the samples were irradiated in the same step.<sup>3</sup> Insufficient reproducibility of the magnetization measurements is also implausible, as this would have resulted in larger standard deviations of the average  $J_c$  values obtained from several samples in the unirradiated state (cf. Subsection 4.1.1). As of this writing, the source of the large scatter in the  $J_c(\Phi_f t)/J_c(0)$  data is unknown.

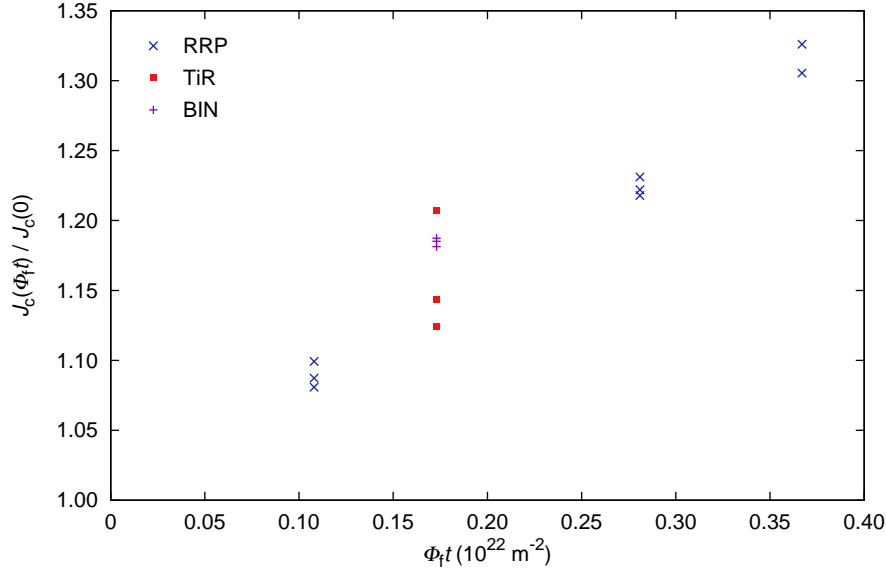


**Figure 4.18.:** Scatter of the  $J_c$  change at 4.2 T and 6 T, obtained by irradiating several samples of the same type to the same fluence.

In Figure 4.19 the increase of the critical current density at 4.2 K as a function of fast neutron fluence is shown for all wire types. An evaluation field of 6 T was selected because this value is close to the upper limit of the field range accessible with the SQUID magnetometer used for the measurements. Despite the large scatter, it is evident that there is no clear sign of a peak in the  $J_c(\Phi_f t)$  data of either one of the five wire types. At  $T = 4.2$  K and  $B = 6$  T a pronounced peak was expected to be found at a fast neutron fluence below  $10^{22} \text{ m}^{-2}$  in all wires containing additives (cf. Subsection 1.2.3). The fact that no peaks were found within the fluence range discussed in the present work proves that the state-of-the-art wires described in Section 2.1 exhibit a different irradiation behavior than the wires examined in previous studies. This important result and some of the data shown in Figure 4.19 are discussed by Flükiger et al. in [47].

<sup>3</sup>A small fluence difference can arise from the different positions of the individual samples within the irradiation capsule, but this effect is much too small to be responsible for the observed scatter.

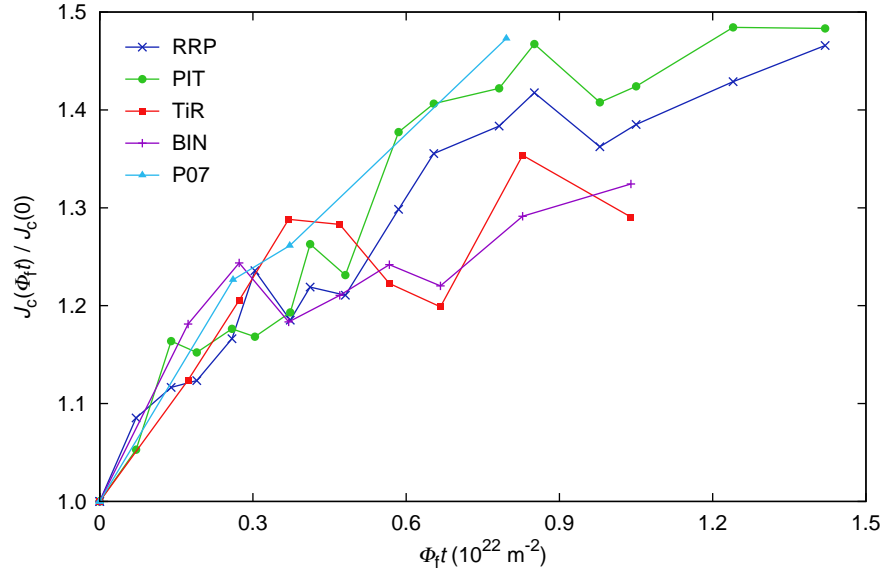


**Figure 4.19.:** Relative increase of the critical current density of all examined wire types as a function of fast neutron fluence evaluated at  $T = 4.2$  K and  $B = 6$  T. The points are connected to guide the eye.

As mentioned in Subsection 3.3.1, the irradiated transport samples TiR-T1 and P07-T2 sustained damage of unknown origin, and only sample TiR-T2 could be measured after irradiation to  $\Phi_f t = 3.7 \cdot 10^{21} \text{ m}^{-2}$ . The previously unirradiated sample TiR-8 was also included in this irradiation step in order to have a sample for magnetization measurements irradiated to exactly the same fluence. A comparison of transport and magnetization data is shown in Figure 4.20. The blue line labeled “ $I_c^{(\text{mag})}$ ” was computed based on the magnetometry data shown in the plot using the two-component pinning force function presented in Subsection 4.2.4. Critical current values were calculated analogously to the procedure described in Subsection 3.4.6 based on the  $J_c$  values obtained from magnetometry and the A-15 cross section of the wire. The second mechanism contribution  $\beta$  (cf. Subsection 4.2.4) and the scaling field  $B_{c2}^*$  (as well as the normalization constant of the pinning force function) were fit to the magnetometry data measured at 4.2 K instead of using the values obtained by minimizing the error for the entire magnetometry temperature range. This was necessary because of the large error otherwise introduced by the unphysically high scaling field values at low temperatures which arise from the global fitting procedure, as discussed in Subsection 4.1.4 and Subsection 4.2.4. The resulting fit parameters are  $p_1 = 0.458$ ,  $q_1 = 2.262$  (obtained from unirradiated samples; cf. Subsection 4.1.4),  $p_2 = 1$ ,  $q_2 = 2$  (fixed second mechanism),  $B_{c2}^* = 27.70$  T (a reasonable value at this temperature),



and  $\beta = 0.498$  (higher than the value obtained from the global fit).

The red curve in Figure 4.20 is the  $I_c(B)$  curve obtained from magnetometry, multiplied by the correction factor  $K = 1.059$  determined in Subsection 3.4.6 for unirradiated TiR samples. The deviations between the corrected magnetometry curve and the values obtained from transport measurements amount to +4% at 13.4 T, and +12% at 15.3 T, which corresponds to a slightly worse agreement than observed in the unirradiated state (cf. Figure 3.29 and Table 3.3). The fact that the agreement between transport data and magnetometry results is worsened by multiplying the magnetometry curve with the correction factor  $K$  indicates that the extrapolation to high fields is less reliable in irradiated samples.

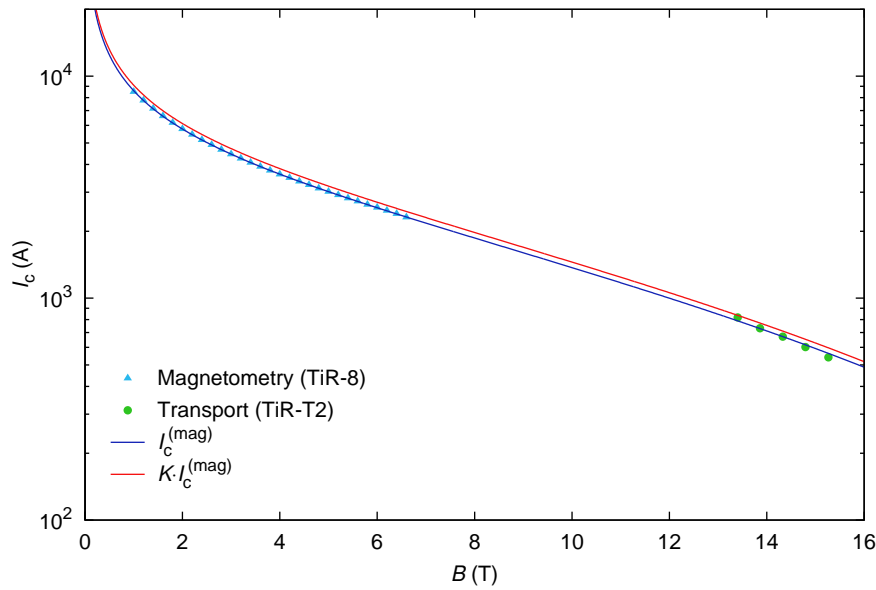


**Figure 4.20.:** Comparison of magnetometry results and transport measurements for the TiR wire at a fast neutron fluence of  $3.7 \cdot 10^{21} \text{ m}^{-2}$ . The red curve represents the critical current obtained from magnetometry multiplied by the correction factor determined in Subsection 3.4.6.

### 4.2.2. Critical temperature

The critical temperature of short wire samples was determined in the unirradiated state and after each irradiation step by means of AC susceptibility measurements (cf. Subsection 3.1.4), using the evaluation method described in Subsection 3.4.7. Within the fast

neutron fluence range investigated in this work, all examined wire types exhibit a small  $T_c$  depression which amounts to roughly 2% at  $\Phi_f t = 10^{22} \text{ m}^{-2}$ . A linear dependence

$$T_c(\Phi_f t) = T_c(0) - k_T \Phi_f t, \quad (4.14)$$

where  $T_c(0)$  is the critical temperature in the unirradiated state, and  $k_T = dT_c/d(\Phi_f t)$  is the slope of the degradation, is in good agreement with the data. The results of the  $T_c$  evaluation of measurements on irradiated samples as well as linear fits according to (4.14) are shown in Figure 4.21. The fit parameters  $T_c(0)$  and  $k_T$  are given in Table 4.5 for each sample type. Note that the  $k_T$  values of the RRP, PIT, TiR, and P07 sample types are in agreement with each other within 10%, whereas the BIN samples exhibit a significantly smaller  $T_c$  degradation with increasing fluence. Flükiger et al. reported some of these results in [47].

Wiesmann et al. reported that the critical temperature of A-15 superconductors irradiated with alpha-particles exhibited a steeper decrease with increasing fluence in samples with a high initial normal state resistivity  $\rho_n$  [141]. They argued that low-resistivity samples require more damage to smear out the electronic density of states sufficiently to produce a certain  $T_c$  reduction (cf. Subsection 1.2.1) than high-resistivity samples, which are in a highly disordered state even before irradiation. The normal state resistivities of the A-15 regions inside the examined wires are not known, but since the BIN wire type is the only one without Ta or Ti additions, it stands to reason that it might have the smallest  $\rho_n$  of the five wire types. In this case its slower  $T_c$  degradation could be explained with the same argument.

Using the relationship between the critical temperature and the long range order parameter  $S$  proposed by Sweedler et al. in [127] (cf. Subsection 1.2.3), the change in long range order can be cast in the form

$$\frac{S(\Phi_f t)}{S(0)} = 1 + \frac{1}{C} \ln \left( \frac{T_c(\Phi_f t)}{T_c(0)} \right). \quad (4.15)$$

Inserting the above-mentioned  $T_c$  reduction of 2% and the value  $C = 5$  suggested by Sweedler et al. into (4.15) gives a decrease in  $S$  of 0.4% at a fast neutron fluence of  $10^{22} \text{ m}^{-2}$ . According to the definition of  $S$  (cf. Subsection 1.2.1, in particular (1.2)) this change in long range order corresponds to a displacement of approximately 0.1% of the Nb atoms to lattice sites normally occupied by Sn, or to interstitial positions.

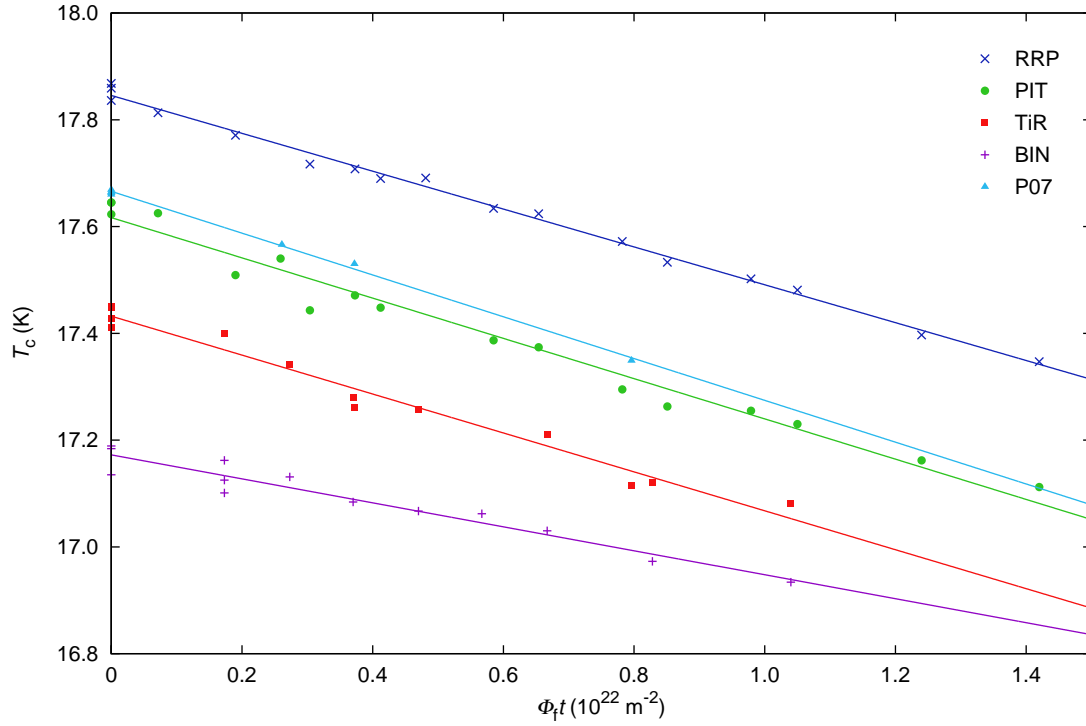


**Figure 4.21.:** Depression of the critical temperature in the five examined wire samples as a function of fast neutron fluence. Linear fits according to (4.14) were used to determine the slope of the degradation.

Wire type	$T_c(0)$ (K)	$k_T$ ( $10^{-22}$ K·m <sup>2</sup> )
RRP	17.85	0.355
PIT	17.62	0.377
TiR	17.43	0.365
BIN	17.17	0.225
P07	17.67	0.392

**Table 4.5.:** Parameters describing the linear decrease of  $T_c$  with increasing fast neutron fluence according to (4.14).

### 4.2.3. Upper critical field

As described in Subsection 3.3.2, resistivity measurements were used to determine the upper critical field of irradiated short wire samples using the evaluation method discussed in Subsection 3.4.8. Only three samples were measured, owing to the high demand for measurement time in the 17 T system and to the fact that the data obtained from these three samples were sufficient to deduce a general behavior. Slopes and zero-temperature upper critical field values were obtained from the data in the same way as described in Subsection 4.1.3. The  $B_{c2}(0)$  values were computed by fitting (4.7) to all data points (as opposed to using the dirty limit WHH expression (4.3)).

The  $B_{c2}(T)$  extrapolations from which the zero-temperature  $B_{c2}$  values were obtained are shown in Figure 4.22 (sample TiR-2), Figure 4.23 (sample BIN-2), and Figure 4.24 (sample P07-1), together with the respective data and extrapolations obtained from unirradiated samples (cf. Subsection 4.1.3). The slopes and the  $B_{c2}(0)$  values as well as their changes relative to the values measured in the unirradiated state of the wires are listed in Table 4.6. Remarkably, at a fast neutron fluence of  $10^{22} \text{ m}^{-2}$  the extrapolated zero-temperature upper critical field values exhibit only a minor increase between 1.8% and 5.6% (extrapolated from the result obtained from sample P07-1 at  $\Phi_f t = 8 \cdot 10^{21} \text{ m}^{-2}$ ). Since the increase is small in a Ta alloyed wire as well as in a Ti alloyed wire, and even in a wire which contains no additives, it stands to reason that the fluence dependence of  $B_{c2}$  in the other two Ta alloyed wire types (RRP and PIT) is similarly weak.

Due to the relationship  $B_{c2} = \kappa \sqrt{2} B_c$ , a small increase in the upper critical field corresponds to a small increase in the Ginzburg-Landau parameter  $\kappa$ . According to the Gor'kov-Goodman relation  $\kappa = \kappa_0 + C \sqrt{\gamma} \rho_n$ , the normal state resistivity  $\rho_n$  will reflect this small increase, unless the electronic specific heat coefficient  $\gamma$  decreases at a much higher rate than  $\rho_n$  increases, which is not expected (cf. Subsection 1.2.1 as well as [142] and [2]). As discussed by Weiss and Flükiger in [139], the relative change in  $\rho_n$  in wires containing additives can be expected to be minor, owing to their high initial resistivity. In the case of the BIN wire, however, the small  $B_{c2}$  increase was somewhat unexpected. The reason for this behavior might be that for binary  $\text{Nb}_3\text{Sn}$  the BIN wire exhibits a relatively high degree of disorder in the unirradiated state due to a significant deviation from stoichiometry. This assumption is supported by its relatively low critical temperature (cf. Subsection 4.1.2).

In Subsection 4.2.1 the increase of the critical current density as a function of fast neutron fluence was evaluated at  $T = 4.2 \text{ K}$  and  $B = 6 \text{ T}$ . At these field and temperature values the

observed  $B_{c2}$  increase amounts to a change in reduced field  $b$  of roughly 1%. Clearly this small change cannot account for the observed increase in  $J_c$  of approximately 40% at a fast neutron fluence of  $10^{22} \text{ m}^{-2}$ . Therefore, the origin of the large  $J_c$  increase must either be an improvement of the grain boundary pinning caused by irradiation, or an additional pinning force contribution stemming from radiation induced defects. Strong arguments for the latter are presented in Subsection 4.2.4.

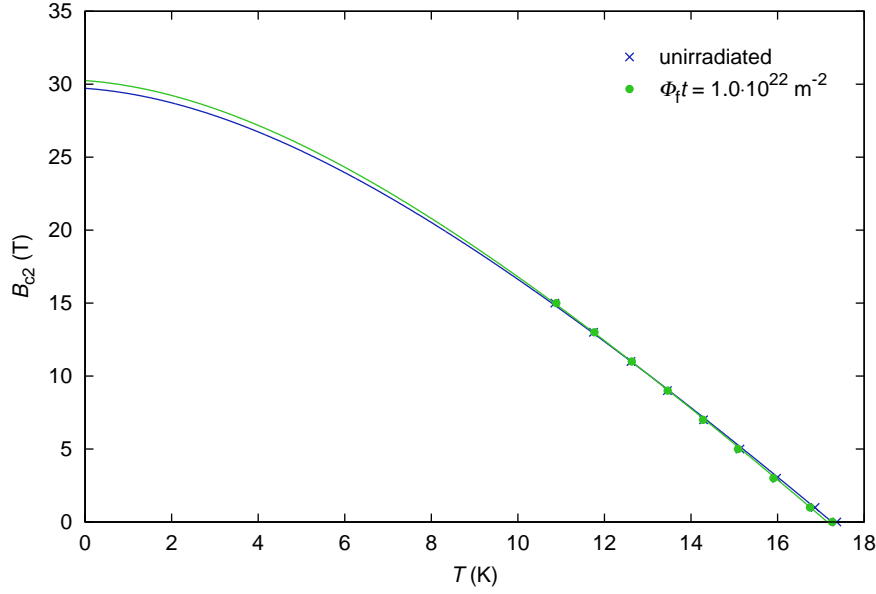


**Figure 4.22.:** Data points and extrapolation of the upper critical field of irradiated sample TiR-2 and data of the unirradiated TiR wire for comparison.

Sample	$\Phi_f t$ ( $10^{22} \text{ m}^{-2}$ )		$(dB_{c2}/dT)_{T=T_c}$ (T/K)		$B_{c2}(0)$ (T)	
TiR-2	1.0	(step 13)	-2.40	(+2.5%)	30.25	(+1.8%)
BIN-2	1.0	(step 13)	-1.91	(+2.9%)	23.93	(+2.6%)
P07-1	0.8	(step 12)	-2.19	(+4.2%)	28.63	(+4.5%)

**Table 4.6.:** Upper critical field slopes and zero-temperature  $B_{c2}$  values (obtained by fitting (4.7) to the  $B_{c2}(T)$  data) of three irradiated short wire samples.

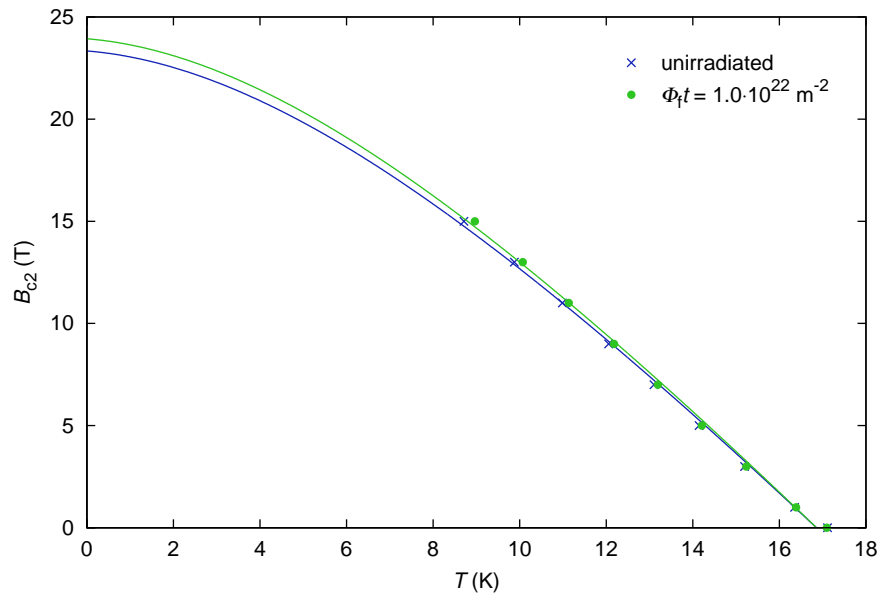


**Figure 4.23.:** Data points and extrapolation of the upper critical field of irradiated sample BIN-2 and data of the unirradiator BIN wire for comparison.

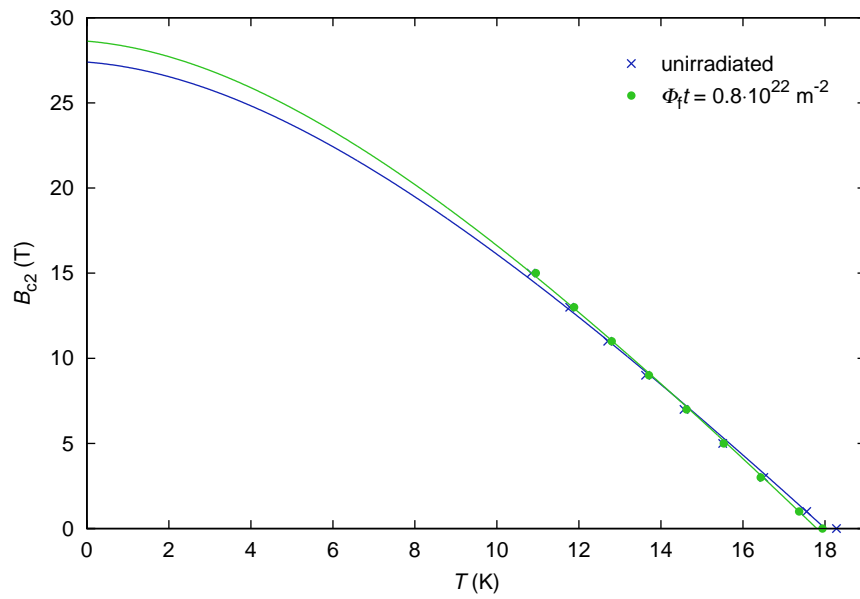


**Figure 4.24.:** Data points and extrapolation of the upper critical field of irradiated sample P07-1 and data of the unirradiator P07 wire for comparison.

#### 4.2.4. Scaling behavior

When the pinning force scaling behavior of data obtained from magnetization measurements (cf. Subsection 3.4.5) on irradiated samples was analyzed using the algorithm described in Subsection 4.1.4, it was found that the position of the peak in the pinning force function shifted towards higher values of the reduced field  $b$  with increasing fluence. For instance, in unirradiated BIN samples the peak is located at  $b_{\max} = 0.183$ , whereas it occurs at  $b_{\max} = 0.234$  after irradiation to a fast neutron fluence of  $10^{22} \text{ m}^{-2}$ , which corresponds to a shift by 28%. This shift manifests itself in an increase of the low-field scaling exponent  $p$  and a decrease of the high-field exponent  $q$  (cf. Subsection 1.2.2), which takes the values of these parameters far away from those expected in case of ideal grain boundary pinning ( $p = 1/2$ ,  $q = 2$ ). This peak shift is consistent with the findings of Guinan et al. [56], Seibt [109], and Okada et al. [90], which are discussed in Subsection 1.2.3.

It was conjectured by the present author that the observed shift in  $b_{\max}$  might arise from a second pinning mechanism whose contribution increases with fast neutron fluence. The simplest way of incorporating a second mechanism into the scaling analysis is to modify the pinning force function as follows.

$$f(b) = \alpha b^{p_1} (1 - b)^{q_1} + \beta b^{p_2} (1 - b)^{q_2}, \quad \alpha + \beta = 1 \quad (4.16)$$

In the above expression  $\alpha$  and  $\beta$  denote the relative contributions of the two mechanisms,  $p_1$  and  $q_1$  are the scaling exponents corresponding to the unirradiated state, and  $p_2$  and  $q_2$  are the exponents of the second mechanism. As discussed in Subsection 1.2.3, the idea of using a two-component ansatz was already published by Küpfer et al. [73] as well as Maier and Seibt [78], although not explicitly in the form used in (4.16). In order to test this model, the scaling behavior of irradiated samples was analyzed using an algorithm which performs the following operations:

- Obtain  $F_p(B) = J_c(B) B$  from the magnetometry results for all temperatures at which the measurements were performed.
- Find the peak in  $F_p(B)$ , using extrapolation if necessary.
- Normalize the volume pinning force to its peak value.
- Iterate  $\beta$  (and hence  $\alpha = 1 - \beta$ ) to find the optimum contribution of the second mechanism (whose exponents  $p_2$  and  $q_2$  are selected by the user).
- Normalize (4.16) using a prefactor  $C$  which is calculated from  $\beta$ ,  $p_1$ ,  $q_1$ ,  $p_2$ , and  $q_2$ .

- Fit expression (4.16) normalized with the prefactor  $C$  to the data using  $B_{c2}^*$  as an adjustable parameter to obtain the scaling field at each available temperature.
- Assess the quality of the fits by computing the sum of the deviations between each data point at a given temperature and  $f(b)$ . The global error for all data sets is then calculated by summing up the values obtained at each available temperature.
- Continue to iterate  $\beta$  until the minimum in the global error is found.

Several choices for the second mechanism were tested by using different values of the scaling exponents  $p_2$  and  $q_2$ . The values were taken from Dew-Hughes, who derived the pinning force functions for eight different mechanisms [30]. The best match between the fit functions and the data was obtained when choosing  $p_2 = 1$  and  $q_2 = 2$ , which corresponds to pinning by core interaction between the vortices and normal conducting point-like (small compared to the flux line spacing) structures.

The normalized pinning force data and the fit functions obtained from each sample type after irradiation to the highest fluence are shown in Figure 4.25 (sample RRP-2, step 13,  $\Phi_f t = 1.4 \cdot 10^{22} \text{ m}^{-2}$ ), Figure 4.26 (sample PIT-2, step 13,  $\Phi_f t = 1.4 \cdot 10^{22} \text{ m}^{-2}$ ), Figure 4.27 (sample TiR-2, step 13,  $\Phi_f t = 1.0 \cdot 10^{22} \text{ m}^{-2}$ ), Figure 4.28 (sample BIN-2, step 13,  $\Phi_f t = 1.0 \cdot 10^{22} \text{ m}^{-2}$ ), and Figure 4.29 (sample P07-1, step 12,  $\Phi_f t = 0.8 \cdot 10^{22} \text{ m}^{-2}$ ). These plots suffer from more scatter than those obtained from unirradiated samples (cf. Subsection 4.1.4), which is at least in part due to the fact that the latter are based on data computed by averaging over the  $J_c(T, B)$  data of several samples. The functional dependence of the data, however, is clearly in good agreement with the computed two-mechanism fit functions.

Also shown in the figures is the temperature dependence of the scaling field after irradiation as well as in the unirradiated state for comparison. As can be expected, the scaling analysis of irradiated samples suffers from the same unphysically high scaling fields at low temperatures found in unirradiated samples (cf. Subsection 4.1.4). Although some of the plots suggest a slight increase of the slope  $dB_{c2}^*/dT$  with increasing fluence, Figure 4.30 shows that neither the zero-temperature values nor the slopes of  $B_{c2}^*$  exhibit a discernible trend.<sup>4</sup> Therefore, the temperature dependence of the scaling field observed in unirradiated samples (cf. Subsection 4.1.4) can also be used to describe  $B_{c2}^*(T)$  of irradiated samples. This finding is consistent with the insignificant increase in the upper critical field discussed in Subsection 4.2.3.

<sup>4</sup>In some cases the results of the scaling calculations were not satisfactory, leading to unusually high values of  $dB_{c2}^*/dT$ . The corresponding outliers in Figure 4.30 have been removed for clarity.



These results have three important implications: Firstly, within the field range accessible by the magnetization measurements the present work is based on (up to 7 T), reasonably good pinning force scaling can still be obtained after fast neutron irradiation involving fluences of roughly  $10^{22} \text{ m}^{-2}$ . This, however, requires the introduction of a scaling field with a physically unsound temperature dependence, which leads to failure of scaling at high fields and low temperatures. Secondly, this scaling behavior can be described using a simple two-mechanism model which adds the contribution of radiation induced point-like pinning structures to the pinning force function found in the unirradiated state. And thirdly, the observed increase in the critical current density (cf. Subsection 4.2.1) cannot be accounted for by an increase of the scaling field.

Analyzing the pinning force scaling behavior of all irradiated samples using the magnetometry data obtained after each irradiation step made it possible to assess how the pinning force function changes as a function of fast neutron fluence. Using the two-component model defined by (4.16), this change can be described by the fluence dependence of one single parameter: the point-pinning contribution  $\beta$ . Figure 4.31 shows that the dependence of  $\beta$  on fast neutron fluence appears to be a universal behavior, independent of the sample type.<sup>5</sup> The function

$$\beta(\Phi_f t) = 1 - e^{-(\Phi_f t / \Phi_f t^*)^n} \quad (4.17)$$

was found to be in general agreement with the observed behavior of  $\beta$ , and is shown as a solid line in Figure 4.31. In (4.17)  $\Phi_f t^*$  is a characteristic fast neutron fluence, and the exponent  $n$  is required to adjust the curvature of the function. Both parameters were computed using a fit procedure, which produced the values  $\Phi_f t^* = 1.523 \cdot 10^{22} \text{ m}^{-2}$  and  $n = 0.697$ . According to Figure 4.31  $\beta$  takes on significant values even at relatively low fluences, contrary to the conclusion drawn by Maier and Seibt, who claimed that in high- $J_c$  wires the pinning due to radiation induced defects can be neglected [78].

The temperature scaling behavior of irradiated samples was examined using the algorithm described in Subsection 4.1.4. As already found for unirradiated samples, using the critical temperature obtained from AC susceptibility measurements as scaling temperature  $T_c^*$  produces very good agreement between data and fits. Actually, the analytical expression (4.14) with the sample type dependent parameters given in Table 4.5 was used to obtain the values of  $T_c^*$  at the given fluence. The smallest deviations between data and fits were

---

<sup>5</sup>Note that in order to reduce the scatter some points were filtered out based on the quality of the fit results.

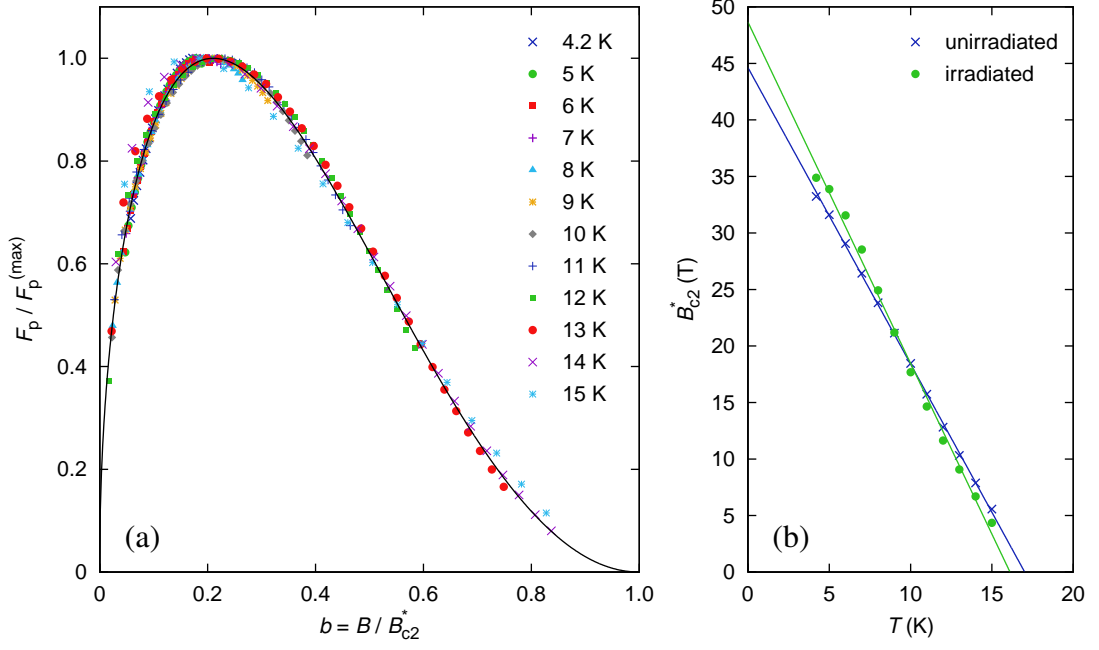


**Figure 4.25.:** Scaling behavior of irradiated sample RRP-2 ( $\Phi_f t = 1.4 \cdot 10^{22} \text{ m}^{-2}$ ). **(a)** Reduced pinning force at different temperatures and two-mechanism pinning force function. **(b)** Temperature dependence of the scaling field before and after irradiation.

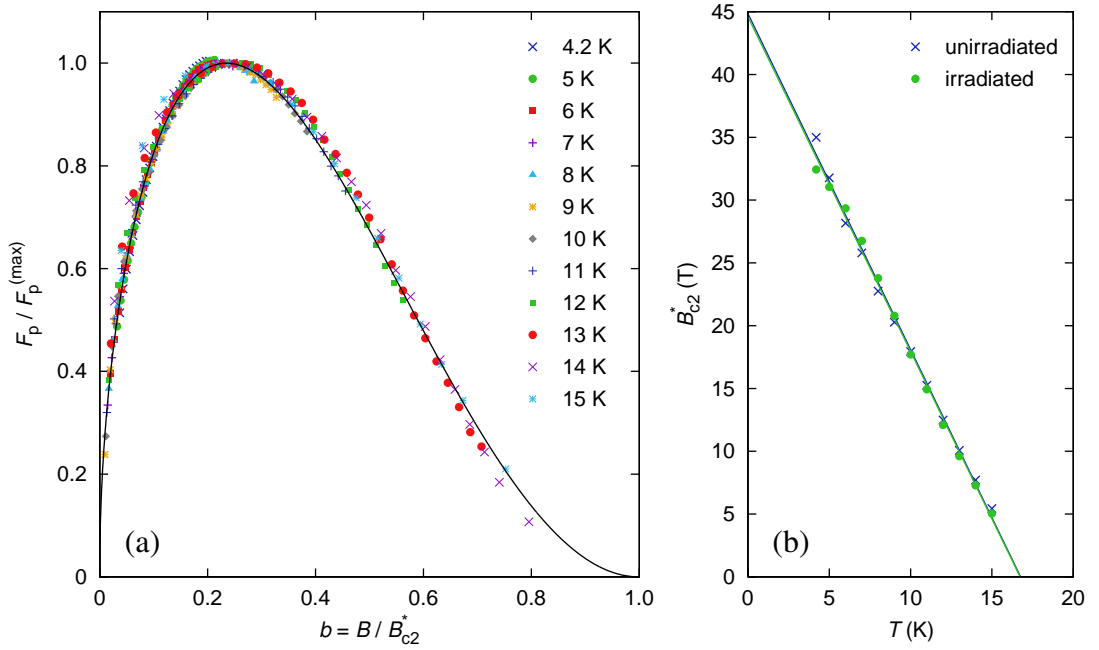


**Figure 4.26.:** Scaling behavior of irradiated sample PIT-2 ( $\Phi_f t = 1.4 \cdot 10^{22} \text{ m}^{-2}$ ). **(a)** Reduced pinning force at different temperatures and two-mechanism pinning force function. **(b)** Temperature dependence of the scaling field before and after irradiation.

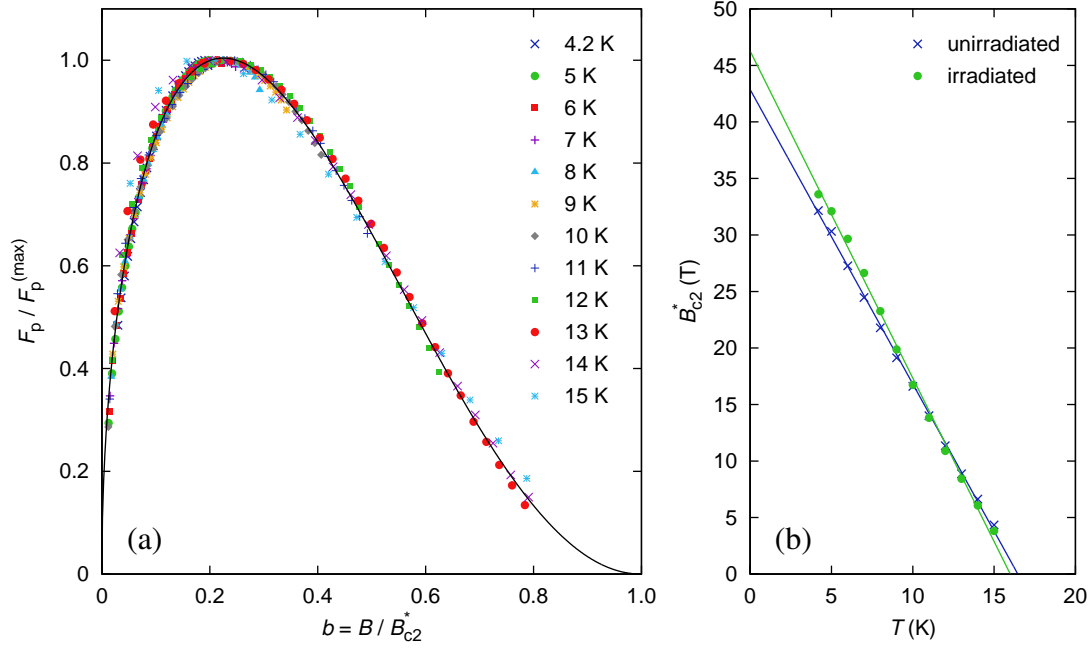


**Figure 4.27.:** Scaling behavior of irradiated sample TiR-2 ( $\Phi_f t = 1.0 \cdot 10^{22} \text{ m}^{-2}$ ). **(a)** Reduced pinning force at different temperatures and two-mechanism pinning force function. **(b)** Temperature dependence of the scaling field before and after irradiation.

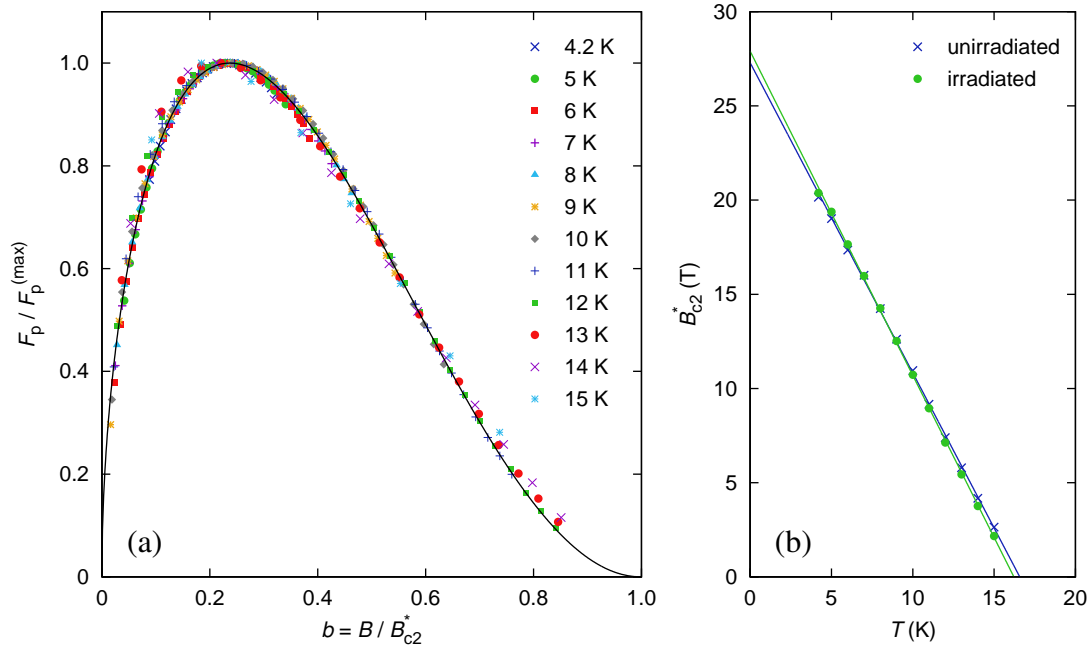


**Figure 4.28.:** Scaling behavior of irradiated sample BIN-2 ( $\Phi_f t = 1.0 \cdot 10^{22} \text{ m}^{-2}$ ). **(a)** Reduced pinning force at different temperatures and two-mechanism pinning force function. **(b)** Temperature dependence of the scaling field before and after irradiation.

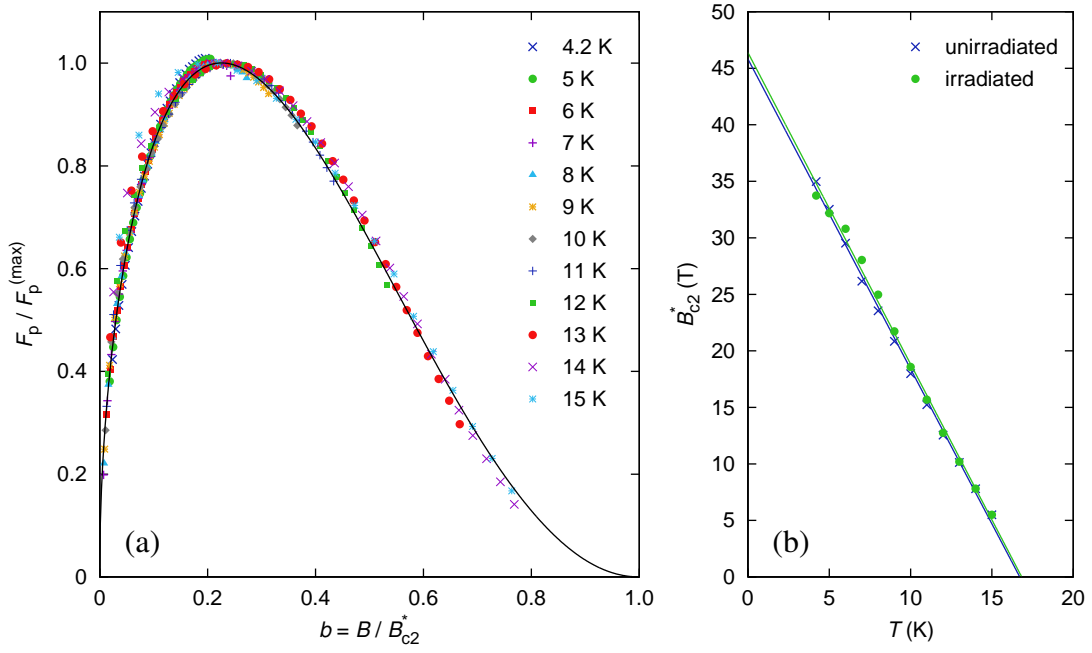


**Figure 4.29.:** Scaling behavior of irradiated sample P07-1 ( $\Phi_f t = 0.8 \cdot 10^{22} \text{ m}^{-2}$ ). **(a)** Reduced pinning force at different temperatures and two-mechanism pinning force function. **(b)** Temperature dependence of the scaling field before and after irradiation.

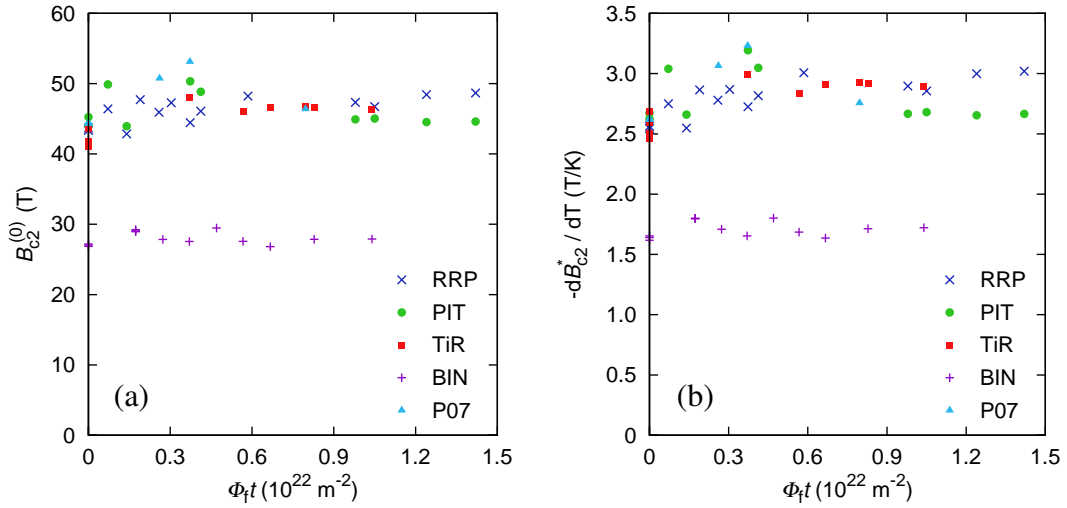


**Figure 4.30.:** Dependence of the scaling field on fast neutron fluence. **(a)** Zero-temperature values of  $B_{c2}^*$ . **(b)** Slopes of the linear temperature dependence. Since there is no discernible trend, the fluence dependence of the scaling field can be neglected.

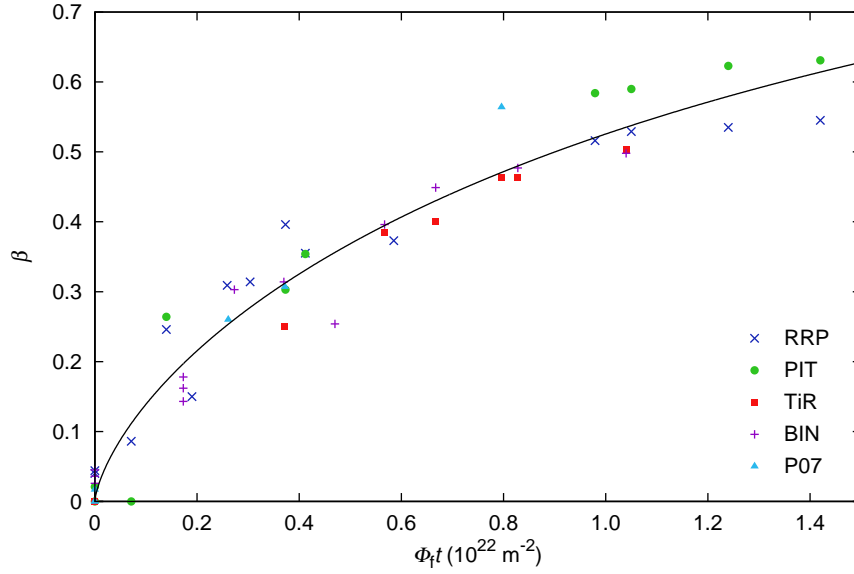


**Figure 4.31.:** Dependence of the point-pinning contribution on fast neutron fluence.

obtained when the exponent  $\mu$  in (4.11) was set to zero, leaving the zero-temperature maximum volume pinning force  $F_p^{(0)}$  as well as the exponents  $\nu$  and  $\eta$  as adjustable parameters. The values obtained for  $\nu$  plotted as a function of fast neutron fluence exhibited only minor scatter (about  $\pm 5\%$  of the average value) and showed no discernible trend. It was therefore decided to fix  $\nu$  to its average value for each sample type, thereby reducing the number of fit parameters.

The thus obtained dependence of  $F_p^{(0)}$  on fast neutron fluence was found to be linear with deviations of less than  $\pm 10\%$  between the data and the linear fits, as shown in Figure 4.32. The fluence dependence of  $\eta$ , which is shown in Figure 4.33, can also be described using linear fits with similar deviations. Hence, the change in temperature scaling behavior as a function of fast neutron fluence can be expressed by two simple functions:

$$F_p^{(0)}(\Phi_f t) = F_p^{(0)}(0) + k_F \Phi_f t \quad (4.18)$$

$$\eta(\Phi_f t) = \eta(0) + k_\eta \Phi_f t \quad (4.19)$$

The zero-fluence values  $F_p^{(0)}(0)$  and  $\eta(0)$  as well as the slopes  $k_F$  and  $k_\eta$  obtained from the fits depicted in Figure 4.32 and Figure 4.33 are summarized in Table 4.7 for each wire type. As can be expected, the values of  $F_p^{(0)}(0)$ ,  $\nu$ , and  $\eta(0)$  do not differ significantly from those obtained from unirradiated samples (cf. Subsection 4.1.4).

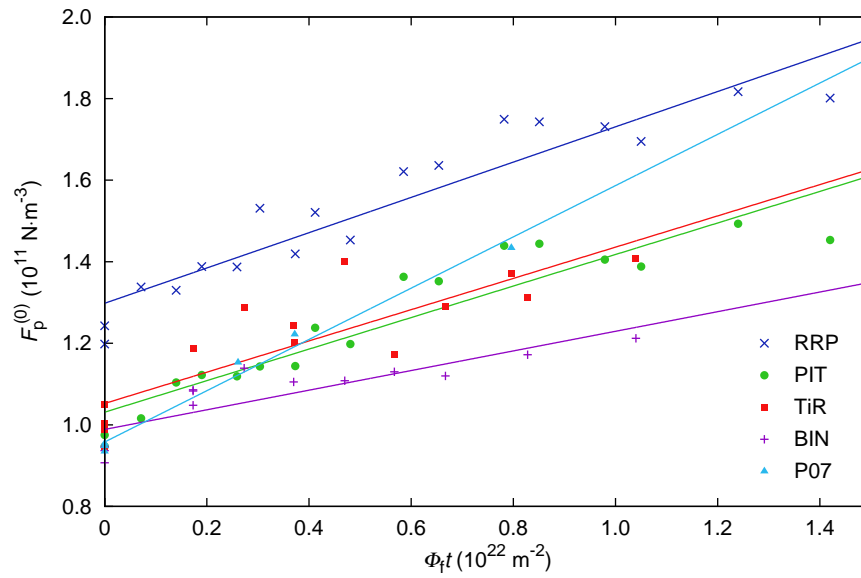


**Figure 4.32.:** Fluence dependence of the zero-temperature value of the maximum volume pinning force of each wire type.

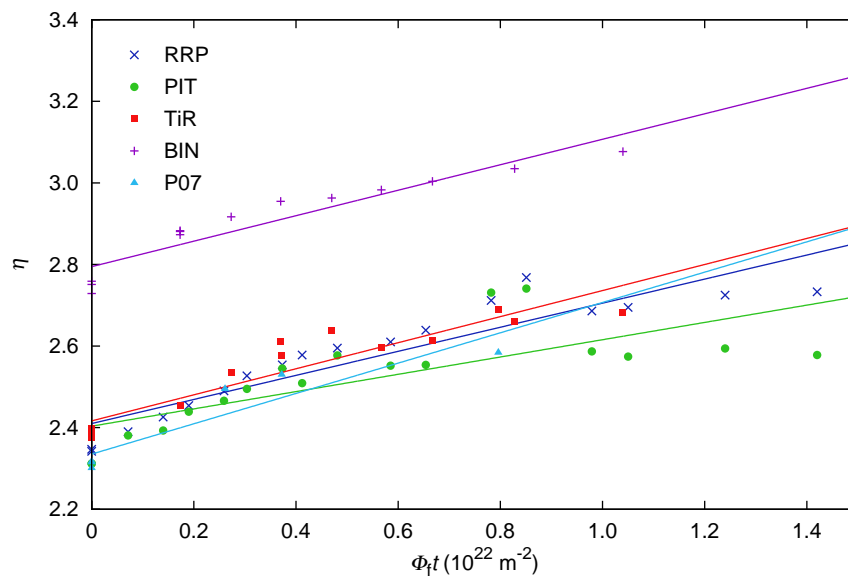


**Figure 4.33.:** Dependence of the temperature scaling exponent  $\eta$  of each wire type on fast neutron fluence.

Wire type	$F_p^{(0)}(0)$ (N/m <sup>3</sup> )	$k_F$ (kg/s <sup>2</sup> )	$\nu$	$\eta(0)$	$k_\eta$ (m <sup>2</sup> )
RRP	$1.30 \cdot 10^{11}$	$4.33 \cdot 10^{-12}$	1.691	2.410	$2.95 \cdot 10^{-23}$
PIT	$1.03 \cdot 10^{11}$	$3.87 \cdot 10^{-12}$	1.651	2.404	$2.12 \cdot 10^{-23}$
TiR	$1.05 \cdot 10^{11}$	$3.83 \cdot 10^{-12}$	1.711	2.417	$3.20 \cdot 10^{-23}$
BIN	$9.89 \cdot 10^{10}$	$2.41 \cdot 10^{-12}$	1.747	2.795	$3.12 \cdot 10^{-23}$
P07	$9.58 \cdot 10^{10}$	$6.29 \cdot 10^{-12}$	1.672	2.335	$3.72 \cdot 10^{-23}$

---

**Table 4.7.:** Parameters used to describe the changes in temperature scaling as a function of fast neutron fluence.

### 4.3. Conclusions

It is the purpose of this very last section to summarize the results presented above and to provide an outlook on possible future studies with the aim of refining the models described in this work. The former is done in Subsection 4.3.1, the latter in Subsection 4.3.2.

#### 4.3.1. Summary of the results

A multitude of experimental results and conclusions drawn from them are presented in this chapter. The most important findings are summarized in the following.

- The  $J_c$  evaluation model presented in Subsection 3.4.1 produces results which are in satisfactory agreement with data obtained from transport measurements at 4.2 K.
- As shown in Subsection 3.4.2, no additional self-field correction of magnetometry results is required, since the first-order correction inherent to the method used in this work for obtaining  $J_c$  from magnetization measurements (cf. Subsection 3.4.5) is sufficient.
- The values of the low- and high-field scaling exponents  $p$  and  $q$  determined from magnetization data on unirradiated samples (cf. Subsection 4.1.4) differ significantly from the ideal grain boundary pinning exponents of  $p = 1/2$  and  $q = 2$ , with the exception of the BIN wire. The coalescence of the reduced pinning force values obtained at various temperatures necessitates the introduction of a scaling field function which takes on unreasonably high values ( $B_{c2}^* > B_{c2}$ ) at low temperatures.

- Using the critical temperature obtained from AC susceptibility measurements (cf. Subsection 3.4.7) as scaling temperature  $T_c^*$  yields good agreement between magnetometry results and the temperature scaling function for both unirradiated and irradiated samples, as discussed in Subsection 4.1.4 and Subsection 4.2.4.
- Within the examined fluence range the degradation of  $T_c$  as a function of fast neutron fluence is in good approximation linear, as shown in Subsection 4.2.2. In the BIN wire this degradation occurs at a significantly slower rate than it does in the other wire types.
- The upper critical field of irradiated samples of the types TiR, BIN, and P07 exhibits only a minor increase relative to the value found in the unirradiated state (cf. Subsection 4.2.3).
- Irradiation induced changes in the field dependence of the pinning force function can be successfully described using the simple model presented in Subsection 4.2.4, which adds a point-pinning contribution of relative strength  $\beta$  to the pinning force function describing the unirradiated state. The fluence dependence of  $\beta$  was found to be a universal function for all examined wire types.

According to the separable form of the unified scaling law (cf. Subsection 1.2.2), the volume pinning force at arbitrary values of temperature and field is given by the product of the strain scaling function  $g(\epsilon)$ , the temperature scaling function  $h(t)$ , the pinning force function  $f(b)$ , and a constant  $C$  which contains a normalization factor as well as the zero-temperature maximum volume pinning force  $F_p^{(0)}$ . Since the strain dependence is not investigated in this work, the strain scaling function was neglected, which is equal to assuming  $g(\epsilon) = 1$ . The functional dependences of  $h(t)$  and  $f(b)$  as well as the effects of fast neutron irradiation on these functions and on  $F_p^{(0)}$  are discussed in Subsection 4.1.4 and Subsection 4.2.4. Based on these results the critical current density as a function of temperature, magnetic field, and fast neutron fluence can be cast in the following form:

$$J_c(T, B, \Phi_f t) = \frac{1}{B} F_p^{(0)} \left[ 1 - \left( \frac{T}{T_c} \right)^\nu \right]^\eta C(\beta, p, q) \left[ (1 - \beta) \left( \frac{B}{B_{c2}^*(T)} \right)^p + \left( 1 - \frac{B}{B_{c2}^*(T)} \right)^q + \beta \frac{B}{B_{c2}^*(T)} \left( 1 - \frac{B}{B_{c2}^*(T)} \right)^2 \right] \quad (4.20)$$

In the above expression the scaling exponents  $p$  and  $q$  are the ones found in the unirradiated state of the wires, and are listed in Table 4.3. The exponents  $p_2 = 1$  and  $q_2 = 2$ , which describe the scaling behavior of the irradiation induced pinning centers, appear in the last term of (4.20). The parameters  $F_p^{(0)}$ ,  $T_c$ ,  $\eta$ , and  $\beta$  are functions of fast neutron fluence, and



can be described as follows.

$$F_p^{(0)}(\Phi_f t) = F_p^{(0)}(0) + k_F \Phi_f t \quad (4.21)$$

$$T_c(\Phi_f t) = T_c(0) - k_T \Phi_f t \quad (4.22)$$

$$\eta(\Phi_f t) = \eta(0) + k_\eta \Phi_f t \quad (4.23)$$

$$\beta(\Phi_f t) = 1 - e^{-(\Phi_f t / \Phi_f t^*)^n} \quad (4.24)$$

The characteristic fluence  $\Phi_f t^*$  is  $1.523 \cdot 10^{22} \text{ m}^{-2}$ , the exponent  $n$  is 0.697, and the wire type dependent parameters  $F_p^{(0)}(0)$ ,  $T_c(0)$ ,  $\eta(0)$ ,  $k_F$ ,  $k_T$ , and  $k_\eta$  are listed in Section 4.2, in particular in Table 4.7 and Table 4.5. As pointed out in Subsection 4.2.4, the dependence of the scaling field on fast neutron fluence can be neglected. Together with the linear temperature dependence of  $B_{c2}^*$  found in Subsection 4.1.4 this leads to the simple expression

$$B_{c2}^*(T) = B_{c2}^*(0) + \frac{dB_{c2}^*}{dT} T, \quad (4.25)$$

with the zero-temperature scaling field  $B_{c2}^*(0)$  and the slope  $dB_{c2}^*/dT$  listed in Table 4.3 for all examined wire types. The function  $C(\beta, p, q)$  normalizes the maximum of the two-mechanism pinning force function to unity, and is given by

$$C(\beta, p, q) = \frac{1}{f(b_{\max})} = \left[ (1 - \beta) b_{\max}^p (1 - b_{\max})^q + \beta b_{\max} (1 - b_{\max})^2 \right]^{-1}. \quad (4.26)$$

The reduced field  $b_{\max}$ , at which the peak in the pinning force function occurs, can be computed by solving

$$(1 - \beta) \left[ p b^{p-1} (1 - b)^q - b^p q (1 - b)^{q-1} \right] + \beta \left[ (1 - b)^2 - 2b(1 - b) \right] = 0 \quad (4.27)$$

for  $b$  and discarding the solution  $b = 1$ .

The capability of expression (4.20) to predict  $J_c(T, B, \Phi_f t)$  within the 7 T field range of the *Quantum Design MPMS XL* SQUID magnetometer used in this work was tested by implementing it in a software code which compares the calculated values to those determined from magnetization measurements (cf. Subsection 3.4.5). This software calculates the average deviation per  $J_c(T, B, \Phi_f t)$  data point for each wire type, including results obtained from all magnetometry samples of this wire type. The calculated average deviations are 5% for the RRP and for the P07 wire, 6% for the PIT and for the TiR wire, and 7% for the

BIN wire. Considering the large scatter in the fluence dependence of  $J_c$  discussed in Subsection 4.2.1, the agreement between (4.20) and the measurement results is satisfactory.

However, large deviations between predicted values and measurement results occur when (4.20) is used to calculate the critical current density at low temperatures and high fields. Transport measurements performed at  $T = 4.2$  K on the unirradiated TiR wire (cf. Subsection 3.4.6) gave a critical current of 948 A at  $B = 10.5$  T (minimum field), and 372 A at  $B = 15.2$  T (maximum field). The corresponding values calculated with expression (4.20) using the A-15 cross section of the wire as well as the correction factor from Table 3.3 are 1158 A (+22%) and 540 A (+45%). Transport measurements on sample TiR-T2 after irradiation to  $\Phi_f t = 3.7 \cdot 10^{21} \text{ m}^{-2}$  yielded  $I_c = 819$  A at  $B = 13.4$  T, and  $I_c = 541$  A at  $B = 15.3$  T, whereas the predicted values are 906 A (+11%) and 681 A (+26%), respectively. Significantly lower deviations can be obtained by extrapolating  $J_c$  to high fields based on magnetometry data obtained at 4.2 K (cf. Subsection 3.4.6 and Subsection 4.2.1) instead of using (4.20).

As discussed in Subsection 4.1.4 and Subsection 4.2.4, this behavior is to be expected due to the fact that the scaling field according to (4.25) exceeds the upper critical field at low temperatures. This shortcoming is the result of minimizing the sum of the fit deviations over the entire temperature range of the magnetization measurements (4.2 – 15 K) while lacking data at low temperatures and high fields. The problem might be remedied to some degree by obtaining such high-field data and including it in the fit procedures. However, since unphysically high scaling fields at low temperatures are necessary for the coalescence of the pinning force data obtained within the accessible field range (up to 7 T), the resulting changes in the fit parameters and in the functional dependence of  $B_{c2}^*(T)$  are bound to have an adverse effect on the deviations between the experimental data and the computed pinning force functions. While improving the accuracy of the values predicted by (4.20) at high fields and low temperatures, it would increase the average deviation over the entire temperature and field range.

This limited pinning force scalability was not expected – at least not in unirradiated samples. The existence of this effect is an important result of this work and calls for further research on flux pinning in state-of-the-art Nb<sub>3</sub>Sn wires. Its absence in the BIN wire (cf. Figure 4.13; the scaling field does not exceed the upper critical field within the temperature range in which data points are available) indicates that additives might be the key to understanding this behavior. As long as no better scaling model for the wire types containing additives is available, it is advisable to perform extrapolations of the critical current

density to high field values based on data obtained at the temperature of interest, as it was done in Subsection 3.4.6 and Subsection 4.2.1.

### 4.3.2. Outlook

While a satisfactory amount of data and results of practical importance were compiled within the scope of the present work, some things are still left to be desired. In hopes of completing and expanding the findings presented in this work, the author would like to propose the following future activities:

- Continue the sequential irradiation of magnetization samples up to fast neutron fluences beyond the peak in the critical current density (cf. Subsection 4.2.1). This would allow to determine the fluence range in which expression (4.20) is valid, and it would help define a common scale for the effects of different kinds of radiation on the investigated wires, provided the peak position is also assessed for these types of radiation.
- Irradiate and measure additional transport samples for comparison with magnetometry results, and in order to gather more high-field data.
- Perform transport measurements at temperatures above 4.2 K to obtain a more comprehensive set of transport data. Due to the lack of thermal stability of the 1000 A sample rod operated in the gas cooled mode in the 17 T system (cf. Subsection 3.3.1), this was not possible within the scope of this work.
- Obtain magnetometry data at fields higher than the upper limit of the SQUID magnetometer used in this work (cf. Section 3.1). This could be achieved by using a magnetometer which can be operated inside the 17 T system described in Section 3.3, such as the rotating sample magnetometer designed by Eisterer et al. [33].
- Analyze the reasons for the limited pinning force scalability of the wire types which contain additives. Perhaps a model which assumes more than one type of pinning mechanism in the unirradiated state as well as different temperature dependences of the pinning force contributions of these mechanisms can improve the quality of the scaling computations.



# Bibliography

- [1] H. Adrian, G. Ischenko, M. Lehmann, P. Müller, H. Braun, and G. Linker, ‘Low temperature irradiation of Nb<sub>3</sub>Sn and V<sub>3</sub>Si with high energy sulphur ions’, *Journal of the Less-Common Metals*, **62**: pp. 99–110, 1978.
- [2] S. A. Alterovitz, D. E. Farrell, B. S. Chandrasekhar, E. J. Haugland, J. W. Blue, and D. C. Liu, ‘Superconductivity of proton-irradiated V<sub>3</sub>Si’, *Physical Review B*, **24** (1): pp. 90–95, 1981.
- [3] J. Appel, ‘Atomic ordering and  $T_c$  of narrow-band superconducting alloys’, *Physical Review B*, **13** (7): pp. 3203–3208, 1976.
- [4] L. R. Aronin, ‘Radiation damage effects on order-disorder in nickel-manganese alloys’, *Journal of Applied Physics*, **25** (3): pp. 344–349, 1954.
- [5] T. Asano, Y. Iijima, K. Itoh, and K. Tachikawa, ‘Effects of titanium addition to the niobium core on the composite-processed Nb<sub>3</sub>Sn’, *Transactions of the Japan Institute of Metals*, **27** (3): pp. 204–214, 1986.
- [6] H. Bauer, E. J. Saur, and D. G. Schweitzer, ‘Effect of neutron irradiation on superconducting properties of A-15 compounds undoped and doped with <sup>10</sup>B and <sup>235</sup>U’, *Journal of Low Temperature Physics*, **19** (3–4): pp. 171–187, 1975.
- [7] F. Baumgärtner, *Tabelle zur Neutronenaktivierung*, Thiemig Verlag, 1967, ISBN 978-3446147744.
- [8] T. Baumgartner, M. Eisterer, H. W. Weber, R. Flükiger, B. Bordini, L. Bottura, and C. Scheuerlein, ‘Evaluation of the critical current density of multifilamentary Nb<sub>3</sub>Sn wires from magnetization measurements’, *IEEE Transactions on Applied Superconductivity*, **22** (3): p. 6000604 (4 pp.), 2012.
- [9] C. P. Bean, ‘Magnetization of high-field superconductors’, *Reviews of Modern Physics*, **36** (1P1): pp. 31–39, 1964.
- [10] C. P. Bean, R. L. Fleischer, P. S. Swartz, and H. R. Hart Jr., ‘Effect of thermal-neutron irradiation on the superconducting properties of Nb<sub>3</sub>Al and V<sub>3</sub>Si doped with fissionable impurities’, *Journal of Applied Physics*, **37** (6): pp. 2218–2224, 1966.

- [11] K. H. Bennemann and J. B. Ketterson (editors), *Superconductivity – Conventional and Unconventional Superconductors*, Springer, 2008, ISBN 978-3540732525.
- [12] B. Besslein and G. Ischenko, ‘Influence of irradiation induced atomic disorder on  $H_{c2}$  of  $Nb_3Sn$ ’, *Solid State Communications*, **19** (9): pp. 867–869, 1976.
- [13] R. Bett, ‘The effects of neutron irradiation damage on the superconducting properties of  $Nb_3Sn$ ’, *Cryogenics*, **14** (7): pp. 361–366, 1974.
- [14] R. Blaschke, J. Ashkenazi, O. Pictet, D. D. Koelling, A. T. van Kessel, and F. M. Müller, ‘The influence of band structure on the electromagnetic properties of superconducting Nb and  $Nb_3Sn$ ’, *Journal of Physics F: Metal Physics*, **14** (1): pp. 175–189, 1984.
- [15] B. Bordini, ‘Self-field correction in critical current measurements of superconducting wires tested on ITER VAMAS barrels’, CERN-ITER Collaboration Report, Internal Note 2010-38.
- [16] B. Bordini, D. Bessette, L. Bottura, A. Devred, M. Jewell, D. Richter, and C. Senatore, ‘Magnetization and inter-filament contact in HEP and ITER bronze-route  $Nb_3Sn$  wires’, *IEEE Transactions on Applied Superconductivity*, **21** (3): pp. 3373–3376, 2011.
- [17] L. Bottura and B. Bordini, ‘ $J_c(B, T, \epsilon)$  parameterization for the ITER  $Nb_3Sn$  production’, *IEEE Transactions on Applied Superconductivity*, **19** (3): pp. 1521–1524, 2009.
- [18] E. H. Brandt and G. P. Mikitik, ‘Shaking of the critical state by a small transverse ac field can cause rapid relaxation in superconductors’, *Superconductor Science and Technology*, **17** (2): pp. S1–S5, 2004.
- [19] C. H. M. Broeders and A. Yu. Konobeyev, ‘Defect production efficiency in metals under neutron irradiation’, *Journal of Nuclear Materials*, **328** (2–3): pp. 197–214, 2004.
- [20] B. S. Brown, ‘Radiation effects in superconducting fusion-magnet materials’, *Journal of Nuclear Materials*, **97** (1–2): pp. 1–14, 1981.
- [21] B. S. Brown and T. H. Blewitt, ‘Critical current density changes in irradiated  $Nb_3Sn$ ’, *Journal of Nuclear Materials*, **80** (1): pp. 18–23, 1979.
- [22] B. S. Brown, T. H. Blewitt, T. L. Scott, and D. G. Wozniak, ‘Critical-current changes in neutron-irradiated  $Nb_3Sn$  as a function of irradiation temperature and initial metallurgy’, *Journal of Applied Physics*, **49** (7): pp. 4144–4148, 1978.
- [23] B. S. Brown, T. H. Blewitt, D. G. Wozniak, and M. Suenaga, ‘Critical current changes in  $Nb_3Sn$  irradiated with fast neutrons at 6 K’, *Journal of Applied Physics*, **46** (12): pp. 5163–5168, 1975.

- [24] F. Cerutti, A. Lechner, A. Mereghetti, and M. Brugger, ‘Particle fluence on LHC magnets’, WAMSDO Workshop, CERN, November 2012.
- [25] B. S. Chandrasekhar, ‘A note on the maximum critical field of high-field superconductors’, *Applied Physics Letters*, **1** (1): pp. 7–8, 1962.
- [26] H.-M. Chang, J. J. Byun, and H.-B. Jin, ‘Effect of convection heat transfer on the design of vapor-cooled current leads’, *Cryogenics*, **46** (5): pp. 324–332, 2006.
- [27] A. M. Clogston, ‘Upper limit for the critical field in hard superconductors’, *Physical Review Letters*, **9** (6): pp. 266–267, 1962.
- [28] S. L. Colucci, H. Weinstock, and M. Suenaga, ‘Critical current enhancement in Nb<sub>3</sub>Sn by low-temperature fast-neutron irradiation’, *Journal of Applied Physics*, **48** (2): pp. 837–838, 1977.
- [29] B. Cort, G. R. Stewart, C. L. Snead Jr., A. R. Sweedler, and S. Moehlecke, ‘Specific-heat studies of neutron-irradiated A15 Nb<sub>3</sub>Al’, *Physical Review B*, **24** (7): pp. 3794–3799, 1981.
- [30] D. Dew-Hughes, ‘Flux pinning mechanisms in type II superconductors’, *Philosophical Magazine*, **30** (2): pp. 293–305, 1974.
- [31] D. Dew-Hughes, ‘Reordering kinetics of disordered A15 compounds’, *Journal of Physics and Chemistry of Solids*, **41** (8): pp. 851–861, 1980.
- [32] E. Drost, W. Specking, and R. Flükiger, ‘Comparison of superconducting properties and residual resistivities of bronze processed Nb<sub>3</sub>Sn wires with Ta, Ti and Ni+Zn additives’, *IEEE Transactions on Magnetics*, **21** (2): pp. 281–284, 1985.
- [33] M. Eisterer, F. Hengstberger, C. S. Voutsinas, N. Hörhager, S. Sorta, J. Hecher, and H. W. Weber, ‘Rotating sample magnetometer for cryogenic temperatures and high magnetic fields’, *Review of Scientific Instruments*, **82**: p. 063902 (4 pp.), 2011.
- [34] J. W. Ekin, ‘Current transfer in multifilamentary superconductors. I. Theory’, *Journal of Applied Physics*, **49** (6): pp. 3406–3409, 1978.
- [35] J. W. Ekin, *Experimental Techniques for Low-Temperature Measurements*, Oxford University Press, 2006, ISBN 978-0198570547.
- [36] J. W. Ekin, ‘Unified scaling law for flux pinning in practical superconductors: I. Separability postulate, raw scaling data and parameterization at moderate strains’, *Superconductor Science and Technology*, **23** (8): pp. 1–30, 2010.
- [37] J. W. Ekin and A. F. Clark, ‘Current transfer in multifilamentary superconductors. II. Experimental results’, *Journal of Applied Physics*, **49** (6): pp. 3410–3412, 1978.
- [38] G. Erdtmann, *Neutron Activation Tables*, Wiley-VCH, 1976, ISBN 978-3527256938.

- [39] M. Föhnle, ‘The elementary interaction force between the flux-line lattice and precipitates’, *Physica Status Solidi (B)*, **83** (2): pp. 433–438, 1977.
- [40] M. Föhnle, ‘The influence of fast neutron irradiation on the critical current densities in Nb<sub>3</sub>Sn. I. Low neutron doses ( $\phi < 2 \times 10^{18}$  neutrons/cm<sup>2</sup>)’, *Physica Status Solidi (B)*, **84** (1): pp. 245–251, 1977.
- [41] M. Föhnle, ‘The influence of fast neutron irradiation on the critical current densities in Nb<sub>3</sub>Sn. II. High neutron doses ( $\phi > 2 \times 10^{18}$  neutrons/cm<sup>2</sup>)’, *Physica Status Solidi (B)*, **84** (2): pp. 541–549, 1977.
- [42] M. Föhnle, ‘Radiation effects on superconductivity in A15 materials’, *IEEE Transactions on Magnetics*, **17** (5): pp. 1707–1710, 1981.
- [43] M. Föhnle and H. Kronmüller, ‘The influence of radiation induced atomic disorder on the superconducting properties of Nb<sub>3</sub>Sn’, *Journal of Nuclear Materials*, **72** (1–2): pp. 249–255, 1978.
- [44] D. E. Farrell and B. S. Chandrasekhar, ‘Defect state in A-15 superconductors’, *Physical Review Letters*, **38** (14): pp. 788–791, 1977.
- [45] W. A. Fietz and W. W. Webb, ‘Hysteresis in superconducting alloys—temperature and field dependence of dislocation pinning in niobium alloys’, *Physical Review*, **178** (2): pp. 657–667, 1969.
- [46] R. Flükiger, ‘Effects of atomic order on the upper critical field and resistivity of A15 superconductors’, in H. Suhl and M. B. Maple (editors), ‘Superconductivity in d- and f-Band Metals’, pp. 265–271, Academic Press, 1980. ISBN: 978-0124143340.
- [47] R. Flükiger, T. Baumgartner, M. Eisterer, H. W. Weber, T. Spina, C. Scheuerlein, C. Senatore, A. Ballarino, and L. Bottura, ‘Variation of  $(J_c/J_{c0})_{\max}$  of binary and ternary alloyed RRP and PIT Nb<sub>3</sub>Sn wires exposed to fast neutron irradiation at ambient reactor temperature’, *IEEE Transactions on Applied Superconductivity*, **23** (3): p. 8001404 (4 pp.), 2013. To be published.
- [48] R. Flükiger, H. Küpfer, J. L. Jorda, and J. Muller, ‘Effect of atomic ordering and composition changes on the electrical resistivity of Nb<sub>3</sub>Al, Nb<sub>3</sub>Sn, Nb<sub>3</sub>Ge, Nb<sub>3</sub>Ir, V<sub>3</sub>Si and V<sub>3</sub>Ga’, *IEEE Transactions on Magnetics*, **23** (2): pp. 980–983, 1987.
- [49] R. Flükiger, C. Senatore, M. Cesaretti, F. Buta, D. Uglietti, and B. Seeber, ‘Optimization of Nb<sub>3</sub>Sn and MgB<sub>2</sub> wires’, *Superconductor Science and Technology*, **21** (5): p. 054015 (8 pp.), 2008.
- [50] R. Flükiger, D. Uglietti, C. Senatore, and F. Buta, ‘Microstructure, composition and critical current density of superconducting Nb<sub>3</sub>Sn wires’, *Cryogenics*, **48** (7–8): pp. 293–307, 2008.



- [51] S. Foner and E. J. McNiff Jr., ‘Upper critical fields of cubic and tetragonal single crystal and polycrystalline Nb<sub>3</sub>Sn in DC fields to 30 Tesla’, *Solid State Communications*, **39** (9): pp. 959–964, 1981.
- [52] A. K. Ghosh, L. D. Cooley, J. A. Parrell, M. B. Field, Y. Zhang, and S. Hong, ‘Effects of reaction temperature and alloying on performance of restack-rod-process Nb<sub>3</sub>Sn’, *IEEE Transactions on Applied Superconductivity*, **17** (2): pp. 2623–2626, 2007.
- [53] A. L. Giorgi, G. R. Stewart, E. G. Szklarz, and C. L. Snead Jr., ‘High-energy-neutron irradiation of A15 Mo<sub>0.4</sub>Tc<sub>0.6</sub>’, *Solid State Communications*, **40** (3): pp. 233–235, 1981.
- [54] A. Godeke, A. den Ouden, A. Nijhuis, and H. H. J. ten Kate, ‘State of the art powder-in-tube niobium-tin superconductors’, *Cryogenics*, **48** (7–8): pp. 308–316, 2008.
- [55] L. P. Gor’kov, ‘Theory of superconducting alloys in a strong magnetic field near the critical temperature’, *Soviet Physics JETP*, **37** (10): pp. 998–1004, 1960.
- [56] M. W. Guinan, R. A. van Konynenburg, and J. B. Mitchell, ‘Effects of low-temperature fusion neutron irradiation on critical properties of a monofilament niobium-tin superconductor’, Informal Report, Lawrence Livermore National Laboratory, 1984.
- [57] M. Gurvitch, A. K. Ghosh, B. L. Gyorffy, H. Lutz, O. F. Kammerer, J. S. Rosner, and M. Strongin, ‘Effects of disorder on the transition temperature and transport properties of a low- $T_c$  A15 superconductor: Mo<sub>3</sub>Ge’, *Physical Review Letters*, **41** (23): pp. 1616–1619, 1978.
- [58] P. A. Hahn, M. W. Guinan, L. T. Summers, T. Okada, and D. B. Smathers, ‘Fusion neutron irradiation effects in commercial Nb<sub>3</sub>Sn superconductors’, *Journal of Nuclear Materials*, **179–181**: pp. 1127–1130, 1991.
- [59] S. Haindl, M. Eisterer, R. Müller, R. Prokopec, H. W. Weber, M. Müller, H. Kirchmayr, T. Takeuchi, and L. Bargioni, ‘Neutron irradiation effects on A15 multifilamentary wires’, *IEEE Transactions on Applied Superconductivity*, **15** (2): pp. 3414–3417, 2005.
- [60] R. R. Hake, ‘Upper-critical-field limits for bulk type-II superconductors’, *Applied Physics Letters*, **10** (6): pp. 189–192, 1967.
- [61] E. Helfand and N. R. Werthamer, ‘Temperature and purity dependence of the superconducting critical field,  $H_{c2}$ ’, *Physical Review Letters*, **13** (23): pp. 686–688, 1964.
- [62] E. Helfand and N. R. Werthamer, ‘Temperature and purity dependence of the superconducting critical field,  $H_{c2}$ . II’, *Physical Review*, **147** (1): pp. 288–294, 1966.

- [63] R. H. Herber and R. Kalish, ‘Mössbauer effect studies on 2-MeV proton irradiated Nb<sub>3</sub>Sn’, *Physical Review B*, **16** (5): pp. 1789–1795, 1977.
- [64] P. Holdway and R. D. Rawlings, ‘Microstructure and radiation damage of commercially produced Nb<sub>3</sub>Sn tapes’, *Cryogenics*, **24** (3): pp. 137–142, 1984.
- [65] P. E. Johnson-Walls, D. R. Dieterich, W. V. Hassenzahl, and J. W. Morris Jr., ‘The microstructural state of Nb<sub>3</sub>Sn in a multifilamentary titanium doped bronze-process wire’, *IEEE Transactions on Magnetics*, **21** (2): pp. 1137–1139, 1985.
- [66] A. E. Karkin, V. E. Arkhipov, B. N. Goshchitskii, E. P. Romanov, and S. K. Sidorov, ‘Radiation effects in the superconductor Nb<sub>3</sub>Sn’, *Physica Status Solidi (A)*, **38** (2): pp. 433–438, 1976.
- [67] N. Karnezos and H. Weinstock, ‘Experimental test of a scaling law in low-temperature, fast-neutron-irradiated Nb<sub>3</sub>Sn and V<sub>3</sub>Ga superconductors’, in A. F. Clark and R. P. Reed (editors), ‘Proceedings of the Third International Cryogenic Materials Conference’, pp. 393–401, 1980.
- [68] K. Katagiri, K. Saito, T. Okada, H. Kodaka, and H. Yoshida, ‘Effect of neutron irradiation on Nb<sub>3</sub>Sn superconducting composites’, *Japanese Journal of Applied Physics Part I*, **26** (Supplement 26-3): pp. 1521–1522, 1987.
- [69] G. H. Kinchin and R. S. Pease, ‘The displacement of atoms in solids by radiation’, *Reports on Progress in Physics*, **18**, 1955.
- [70] W. Klein and H. Kronmüller, ‘Pinning forces in neutron-irradiated Nb<sub>3</sub>Sn diffusion layers’, *Physica Status Solidi (A)*, **67** (1): pp. 109–118, 1981.
- [71] E. J. Kramer, ‘Scaling laws for flux pinning in hard superconductors’, *Journal of Applied Physics*, **44** (3): pp. 1360–1370, 1973.
- [72] H. Küpfer and A. A. Manuel, ‘Summation and saturation behavior of the volume pinning force in neutron-irradiated V<sub>3</sub>Si’, *Physica Status Solidi (A)*, **54** (1): pp. 153–165, 1979.
- [73] H. Küpfer, R. Meier-Hirmer, and T. Reichert, ‘Field dependent change of the critical current density in neutron irradiated A15 superconductors with grain boundary pinning’, *Journal of Applied Physics*, **51** (2): pp. 1121–1126, 1980.
- [74] J. Labbé and J. Friedel, ‘Instabilité électronique et changement de phase cristalline des composés du type V<sub>3</sub>Si à basse température’, *Journal de Physique*, **27** (3–4): pp. 153–165, 1966.
- [75] J. Labbé and E. C. van Reuth, ‘Model to explain large changes in the electronic density of states with atomic ordering in V<sub>3</sub>Au’, *Physical Review Letters*, **24** (22): pp. 1232–1235, 1970.

- [76] M. Lehmann, G. Saemann-Ischenko, H. Adrian, and C. Nölscher, ‘Disordered A15 compounds from the Matthias-valley:  $\text{Mo}_3\text{Ge}$  and  $\text{Mo}_3\text{Si}$ ’, *Physica B+C*, **107** (1–3): pp. 473–474, 1981.
- [77] J. H. Lindenhovius, E. M. Hornsveld, A. den Ouden, W. A. J. Wessel, and H. H. J. ten Kate, ‘Progress in the development of  $\text{Nb}_3\text{Sn}$  conductors based on the “powder in tube” method with finer filaments’, *IEEE Transactions on Applied Superconductivity*, **9** (2): pp. 1451–1454, 1999.
- [78] P. Maier and E. Seibt, ‘Volume pinning force and upper critical field of irradiated  $\text{Nb}_3\text{Sn}$ ’, *Applied Physics Letters*, **39** (2): pp. 175–177, 1981.
- [79] K. Maki, ‘The magnetic properties of superconducting alloys I’, *Physics*, **1** (1): pp. 21–30, 1964.
- [80] K. Maki, ‘The magnetic properties of superconducting alloys II’, *Physics*, **1** (2): pp. 127–143, 1964.
- [81] B. T. Matthias, T. H. Geballe, S. Geller, and E. Corenzwit, ‘Superconductivity of  $\text{Nb}_3\text{Sn}$ ’, *Physical Review*, **95** (6): p. 1435, 1954.
- [82] W. L. McMillan, ‘Transition temperature of strong-coupled superconductors’, *Physical Review*, **167** (2): pp. 331–344, 1968.
- [83] R. Meier-Hirmer and H. Küpfer, ‘Experimental study on the collective theory of flux pinning in a high-field superconductor’, *Physical Review B*, **31** (1): pp. 183–192, 1985.
- [84] R. Meier-Hirmer, T. Reichert, and H. Küpfer, ‘Critical current density and superconducting parameters  $T_c$ ,  $H_{c2}$ , and  $\kappa$  in neutron-irradiated and annealed  $\text{V}_3\text{Si}$ ’, *IEEE Transactions on Magnetics*, **17** (1): pp. 997–999, 1981.
- [85] L. V. Meisel and P. J. Cote, ‘Influence of electron mean free path on superconducting transition temperature’, *Physical Review B*, **19** (9): pp. 4514–4517, 1979.
- [86] M. N. Mukherjee and J. Baixeras, ‘On the relation between the transition temperature and the density of states in A-15 superconductors’, *Physics Letters A*, **68** (3–4): pp. 375–377, 1978.
- [87] P. Müller, G. Ischenko, H. Adrian, J. Bieger, M. Lehmann, and E. L. Haase, ‘Transport properties, electronic density of states and  $T_c$  in disordered A15 compounds’, in H. Suhl and M. B. Maple (editors), ‘Superconductivity in d- and f-Band Metals’, pp. 369–379, Academic Press, 1980. ISBN: 978-0124143340.
- [88] National Nuclear Data Center, <http://www.nndc.bnl.gov/>, 2012.

- [89] C. Nölscher and G. Saemann-Ischenko, ‘Superconductivity and crystal and electronic structures in hydrogenated and disordered Nb<sub>3</sub>Ge and Nb<sub>3</sub>Sn layers with A15 structure’, *Physical Review B*, **32** (3): pp. 1519–1531, 1985.
- [90] T. Okada, M. Fukumoto, K. Katagiri, K. Saito, H. Kodaka, and H. Yoshida, ‘Effects of neutron irradiation on the critical current of bronze processed multifilamentary Nb<sub>3</sub>Sn superconducting composites’, *Journal of Applied Physics*, **63** (9): pp. 4580–4585, 1988.
- [91] T. P. Orlando, J. A. Alexander, S. J. Bending, J. Kwo, S. J. Poon, R. H. Hammond, and M. R. Beasley, ‘The role of disorder in maximizing the upper critical field in the Nb-Sn system’, *IEEE Transactions on Magnetics*, **17** (1): pp. 368–369, 1981.
- [92] T. P. Orlando, E. J. McNiff Jr., S. Foner, and M. R. Beasley, ‘Critical fields, Pauli paramagnetic limiting, and material parameters of Nb<sub>3</sub>Sn and V<sub>3</sub>Si’, *Physical Review B*, **19** (9): pp. 4545–4561, 1979.
- [93] P. M. Ossi, *Disordered Materials*, Springer, second edition, 2006, ISBN 978-3540296096.
- [94] C. S. Pande, ‘Effect of nuclear irradiation on the superconducting transition temperatures of A-15 materials’, *Solid State Communications*, **24** (3): pp. 241–245, 1977.
- [95] C. S. Pande, ‘Direct observation of defects in A-15 compounds produced by fast neutron irradiation’, in H. Suhl and M. B. Maple (editors), ‘Superconductivity in d- and f-Band Metals’, pp. 349–353, Academic Press, 1980. ISBN: 978-0124143340.
- [96] D. M. Parkin and D. G. Schweitzer, ‘Effects of neutron irradiation on the superconducting properties of NbTi and Nb<sub>3</sub>Sn multifilamentary composites’, *Nuclear Technology*, **22** (1): pp. 108–114, 1974.
- [97] D. M. Parkin and A. R. Sweedler, ‘Neutron irradiation of Nb<sub>3</sub>Sn and NbTi multifilamentary composites’, *IEEE Transactions on Magnetics*, **11** (2): pp. 166–169, 1975.
- [98] J. M. Poate, R. C. Dynes, L. R. Testardi, and R. H. Hammond, ‘Comments on defect production and stoichiometry in A-15 superconductors’, *Physical Review Letters*, **37** (19): pp. 1308–1311, 1976.
- [99] C. P. Poole Jr., H. A. Farach, R. J. Creswick, and R. Prozorov (editors), *Superconductivity*, Academic Press, second edition, 2007, ISBN 978-0120887613.
- [100] R. Roberge, H. LeHuy, and S. Foner, ‘Effects of added elements and strain on the martensitic phase transformation of Nb<sub>3</sub>Sn’, *Physics Letters A*, **82** (5): pp. 259–262, 1981.

- [101] F. Rullier-Albenque and Y. Quéré, ‘An experimental argument – in Nb<sub>3</sub>Ge – for the Labbé-Barisic-Friedel theory of A-15 superconductors’, *Physics Letters A*, **81** (4): pp. 232–234, 1981.
- [102] R. M. Scanlan, W. A. Fietz, and E. F. Koch, ‘Flux pinning centers in superconducting Nb<sub>3</sub>Sn’, *Journal of Applied Physics*, **46** (5): pp. 2244–2249, 1975.
- [103] E. Schachinger and M. Prohammer, ‘Anisotropy effects in the A-15 superconductor Nb<sub>3</sub>Sn’, *Physica C*, **156** (5): pp. 701–706, 1988.
- [104] C. Scheuerlein, M. Di Michiel, G. Arnau, R. Flükiger, F. Buta, I. Pong, L. Oberli, and L. Bottura, ‘Coarse Nb<sub>3</sub>Sn grain formation and phase evolution during the reaction of a high Sn content internal tin strand’, *IEEE Transactions on Applied Superconductivity*, **21** (3): pp. 2554–2558, 2011.
- [105] H. Scheurer, R. Meier-Hirmer, and H. Küpfer, ‘Radiation induced changes in critical superconducting properties of V<sub>3</sub>Si’, *Journal of Nuclear Materials*, **133–134** (AUG): pp. 823–825, 1985.
- [106] R. Schmucker, ‘The influence of plastic deformation of the flux-line lattice on flux transport in hard superconductors’, *Physica Status Solidi (B)*, **80** (1): pp. 89–97, 1977.
- [107] R. E. Schwall and G. M. Ozeryansky, ‘Critical current and upper critical field of multifilament Nb<sub>3–x</sub>Ta<sub>x</sub>Sn superconductor’, *Journal of Applied Physics*, **56** (3): pp. 814–818, 1984.
- [108] B. Seeber (editor), *Handbook of Applied Superconductivity*, Institute of Physics Publishing, 1998, ISBN 978-0750303774.
- [109] E. Seibt, ‘Irradiation and annealing effects of deuteron irradiated NbTi and V<sub>3</sub>Ga multifilamentary composite wires at low temperature’, *IEEE Transactions on Magnetics*, **11** (2): pp. 174–177, 1975.
- [110] H. Sekine, K. Itoh, and K. Tachikawa, ‘A study of the  $H_{c2}$  enhancement due to the addition of Ti to the matrix of bronze-processed Nb<sub>3</sub>Sn superconductors’, *Journal of Applied Physics*, **63** (6): pp. 2167–2170, 1988.
- [111] C. Senatore and R. Flükiger, ‘Formation and upper critical fields of the two distinct A15 phases in the subelements of powder-in-tube Nb<sub>3</sub>Sn wires’, *Applied Physics Letters*, **102** (1): p. 012601 (4 pp.), 2013.
- [112] S. Shiota, S. Nishijima, and T. Okada, ‘Degradation of transition temperature and critical current density in neutron irradiated Nb<sub>3</sub>Sn and V<sub>3</sub>Ga’, *IEEE Transactions on Magnetics*, **17** (1): pp. 993–996, 1981.

- [113] C. L. Snead Jr., 'Changes in the upper critical fields and critical currents of Nb<sub>3</sub>Sn and V<sub>3</sub>Ga owing to neutron radiation damage', *Applied Physics Letters*, **30** (12): pp. 662–664, 1977.
- [114] C. L. Snead Jr., 'Low-temperature 30 GeV-proton effects on critical properties of type-II superconducting filamentary conductors', *Journal of Nuclear Materials*, **72** (1–2): pp. 190–197, 1978.
- [115] C. L. Snead Jr., H. Kumakura, and M. Suenaga, 'Effect of disorder on the martensitic phase transformation in Nb<sub>3</sub>Sn', *Applied Physics Letters*, **43** (3): pp. 311–313, 1983.
- [116] C. L. Snead Jr. and D. M. Parkin, 'Effect of neutron irradiation on the critical current of Nb<sub>3</sub>Sn at high magnetic fields', *Nuclear Technology*, **29** (3): pp. 264–267, 1976.
- [117] C. L. Snead Jr., D. M. Parkin, and M. W. Guinan, 'High-energy-neutron damage in Nb<sub>3</sub>Sn: Changes in critical properties, and damage-energy analysis', *Journal of Nuclear Materials*, **103** (1): pp. 749–754, 1981.
- [118] C. L. Snead Jr. and M. Suenaga, 'Neutron-irradiation effects in the pseudobinary compound Nb<sub>3</sub>(SnGa): Changes in  $T_c$ ,  $I_c$ , and flux pinning', *IEEE Transactions on Magnetics*, **15** (1): pp. 625–628, 1979.
- [119] M. Söll, H. Bauer, K. Böning, and R. Bett, 'Effect of low temperature neutron irradiation on superconducting properties of Nb<sub>3</sub>Sn', *Physics Letters A*, **51** (2): pp. 83–84, 1975.
- [120] M. Söll, K. Böning, and H. Bauer, 'Influence of disordering by low-temperature neutron irradiation on the superconducting transition temperature of Nb<sub>3</sub>Sn', *Journal of Low Temperature Physics*, **24** (5–6): pp. 631–644, 1976.
- [121] T. Solleder, H. Kronmüller, and U. Essmann, 'The influence of neutron irradiation on the paramagnetic susceptibility and the upper critical field of V<sub>3</sub>Ge single crystals', in U. Eckern, A. Schmid, W. Weber, and H. Wühl (editors), 'Proceedings of the 17<sup>th</sup> International Conference on Low Temperature Physics, LT-17', pp. 607–608, 1984.
- [122] C. M. Soukoulis and D. A. Papaconstantopoulos, 'Effects of disorder on properties of A15 materials', *Physical Review B*, **26** (7): pp. 3673–3681, 1982.
- [123] M. Suenaga, 'Optimization of Nb<sub>3</sub>Sn', *IEEE Transactions on Magnetics*, **21** (2): pp. 1122–1128, 1985.
- [124] M. D. Sumption, X. Peng, E. Lee, X. Wu, and E. W. Collings, 'Analysis of magnetization, AC loss, and  $d_{eff}$  for various internal-Sn based Nb<sub>3</sub>Sn multifilamentary strands with and without subelement splitting', *Cryogenics*, **44** (10): pp. 711–725, 2004.

- [125] A. R. Sweedler, D. Cox, D. G. Schweitzer, and G. W. Webb, ‘Neutron induced disorder in superconducting A-15 compounds’, *IEEE Transactions on Magnetics*, **11** (2): pp. 163–165, 1975.
- [126] A. R. Sweedler and D. E. Cox, ‘Superconductivity and atomic ordering in neutron-irradiated Nb<sub>3</sub>Al’, *Physical Review B*, **12** (1): pp. 147–156, 1975.
- [127] A. R. Sweedler, D. G. Schweitzer, and G. W. Webb, ‘Atomic ordering and superconductivity in high- $T_c$  A-15 compounds’, *Physical Review Letters*, **33** (3): pp. 168–172, 1974.
- [128] L. R. Testardi and L. F. Mattheiss, ‘Electron lifetime effects on properties of A15 and bcc materials’, *Physical Review Letters*, **41** (23): pp. 1612–1615, 1978.
- [129] L. Thilly, M. Di Michiel, C. Scheuerlein, and B. Bordini, ‘Nb<sub>3</sub>Sn nucleation and growth in multifilament superconducting strands monitored by high resolution synchrotron diffraction during in situ reaction’, *Applied Physics Letters*, **99** (12): p. 122508 (3 pp.), 2011.
- [130] M. Tschurlovits, A. Leitner, and G. Daverda, ‘Dose rate constants for new dose quantities’, *Radiation Protection Dosimetry*, **42** (2): pp. 77–82, 1992.
- [131] C. C. Tsuei, ‘Relationship between the density of states and the superconducting transition temperature in A-15 compounds’, *Physical Review B*, **18** (11): pp. 6385–6387, 1978.
- [132] D. Uglietti, C. Senatore, A. Reginelli, H. J. Mathieu, and R. Flükiger, ‘Correlation between the overall  $T_c$  distribution in bronze route Nb<sub>3</sub>Sn wires and the Sn gradient in the filaments’, *IEEE Transactions on Applied Superconductivity*, **18** (2): pp. 1010–1013, 2008.
- [133] R. Viswanathan and R. Caton, ‘Effect of neutron irradiation on single-crystal V<sub>3</sub>Si: Heat capacity and resistivity’, *Physical Review B*, **18** (1): pp. 15–21, 1978.
- [134] R. Viswanathan, R. Caton, and C. S. Pande, ‘Superconducting transition-temperature widths in neutron-irradiated single-crystal V<sub>3</sub>Si’, *Physical Review Letters*, **41** (13): pp. 906–910, 1978.
- [135] R. Viswanathan, R. Caton, and C. S. Pande, ‘Superconductivity in irradiated A-15 compounds at low fluences. I. Neutron-irradiated V<sub>3</sub>Si’, *Journal of Low Temperature Physics*, **30** (3–4): pp. 503–511, 1978.
- [136] H. W. Weber, ‘Radiation effects on superconducting fusion magnet components’, *International Journal of Modern Physics E*, **20** (6): pp. 1325–1378, 2011.
- [137] H. W. Weber, H. Böck, E. Unfried, and L. R. Greenwood, ‘Neutron dosimetry and damage calculations for the TRIGA MARK-II reactor in Vienna’, *Journal of Nuclear Materials*, **137** (3): pp. 236–240, 1986.

- [138] H. W. Weber and O. Hittmair, *Supraleitung*, Verlag Karl Thiemig, 1979, ISBN 978-3521061132.
- [139] F. Weiss, R. Flükiger, W. Maurer, P. A. Hahn, and M. W. Guinan, ‘Changes in superconducting properties by room-temperature neutron-irradiation for binary and alloyed Nb<sub>3</sub>Sn multifilamentary wires’, *IEEE Transactions on Magnetics*, **23** (2): pp. 976–979, 1987.
- [140] N. R. Werthamer, E. Helfand, and P. C. Hohenberg, ‘Temperature and purity dependence of the superconducting critical field,  $H_{c2}$ . III. Electron spin and spin-orbit effects’, *Physical Review*, **147** (1): pp. 295–302, 1966.
- [141] H. Wiesmann, M. Gurvitch, A. K. Ghosh, H. Lutz, K. W. Jones, A. N. Goland, and M. Strongin, ‘Superconductivity in irradiated A-15 compounds at low fluences. II. Alpha-particle-irradiated Nb<sub>3</sub>Sn and Nb<sub>3</sub>Ge’, *Journal of Low Temperature Physics*, **30** (3–4): pp. 513–519, 1978.
- [142] H. Wiesmann, M. Gurvitch, A. K. Ghosh, H. Lutz, O. F. Kammerer, and M. Strongin, ‘Estimate of density-of-states changes with disorder in A-15 superconductors’, *Physical Review B*, **17** (1): pp. 122–125, 1978.
- [143] E. Wildner, F. Broggi, F. Cerutti, A. Ferrari, A. Mereghetti, and E. Todesco, ‘Energy deposition patterns in the LHC inner triplet and their impact on the Phase II luminosity upgrade’, in ‘Proceedings of the 23<sup>rd</sup> Particle Accelerator Conference’, pp. 2543–2545, 2009.
- [144] A. V. Zlobin, G. Ambrosio, N. Andreev, E. Barzi, P. Bauer, D. Chichili, Y. Huang, L. Imbasciati, V. V. Kashikhin, M. Lamm, P. Limon, I. Novitski, T. Peterson, J. B. Strait, S. Yadav, and R. Yamada, ‘Conceptual design study of Nb<sub>3</sub>Sn low-beta quadrupoles for 2nd generation LHC IRs’, *IEEE Transactions on Applied Superconductivity*, **13** (2): pp. 1266–1269, 2003.



# Curriculum Vitae

**Name** Thomas Baumgartner  
**Date of birth** November 24, 1983  
**Place of birth** Vienna, Austria  
**Address** Düsseldorfstraße 5–13/2/22,  
1220 Vienna, Austria

## Education and experience

**2010 – 2013** PhD research at the Atominstitut, Vienna University of Technology  
Project assistant

**2004 – 2010** Studies of physics at the Vienna University of Technology  
Diploma thesis: ‘Transport current anisotropy in melt-textured high-temperature superconductors’

**1998 – 2003** TGM, Höhere Technische Lehranstalt (secondary technical college), 1200 Vienna, Austria

**1994 – 1998** Neulandschule, Gymnasium (lower secondary education), 1190 Vienna, Austria

**1990 – 1994** Neulandschule, Volksschule (primary education), 1190 Vienna, Austria

## Publications

‘Variation of  $(J_c/J_{c0})_{\max}$  of Binary and Ternary Alloyed RRP and PIT Nb<sub>3</sub>Sn Wires Exposed to Fast Neutron Irradiation at Ambient Reactor Temperature’, R. Flükiger, T. Baumgartner, M. Eisterer, H. W. Weber, T. Spina, C. Scheuerlein, C. Senatore, A. Ballarino, and L. Bottura, *IEEE Transactions on Applied Superconductivity*, **23** (3): p. 8001404 (4 pp.), 2013. To be published.

‘ $J_c(B, T)$  Characterization of Commercial NbTi Strands for the ITER Poloidal Field Coils by Transport and Magnetization Methods’, Yu. V. Karasev, V. I. Pantsyrny, M. V. Polikarpova, P. A. Lukianov, L. V. Potanina, T. Baumgartner, M. Eisterer, and H. W. Weber, *IEEE Transactions on Applied Superconductivity*. To be published.

‘Evaluation of the Critical Current Density of Multifilamentary Nb<sub>3</sub>Sn Wires From Magnetization Measurements’, T. Baumgartner, M. Eisterer, H. W. Weber, R. Flükiger, B. Bordini, L. Bottura, and C. Scheuerlein, *IEEE Transactions on Applied Superconductivity*, **22** (3): p. 6000604 (4 pp.), 2012.